University of Oxford

Department of Materials

Lead Oxides for Photovoltaics

Thesis

Laura Melanie Droessler

Supervisors:

Dr Andrew A.R. Watt and Dr Hazel E. Assender

Abstract

This thesis investigates lead oxides as photovoltaic materials. Vacuum deposition methods and *ex-situ* annealing are used to produce different stoichiometries of lead oxide. The relationship between structure and the optoelectronic properties is then investigated. Following this, a number of photovoltaic devices are prototyped and a Kelvin probe used to determine and understand the band structure of devices.

Thin films of PbO produced via air annealing of thermally evaporated lead consist of a mixture of two phases, orthorhombic and tetragonal, that determine the materials properties and effectiveness as absorber layer in a Schottky device. Films of higher tetragonal content are more photoactive, showing lower series resistance. Kelvin probe reveals that with an increasing work function of the PbO with increasing duration of the annealing, the Schottky barrier between PbO and Al increases, which results in a higher V_{OC}. This trend is inverted when the Fermi level of PbO drops below that of ITO, creating an opposing junction.

Reactively sputtered PbO_2 films are highly conductive degenerate semiconductors. Increasing oxygen flow rate during deposition leads to increased resistivity and decreased mobility, resulting from a decrease in grain size. Alongside this an increase in carrier concentration is observed as the material gets less ordered at higher oxygen flow rates, which results in an increase in Fermi level. Due to its high conductivity the material is not photoactive, and the high work function between -5.6 and -5.8 eV does not allow the formation of a Schottky junction or a p-n junction with the evaporated p- type PbO.

Post deposition annealing of the sputtered films leads to the formation of the more resistive Pb_3O_4 phase. This material shows lower carrier concentration and mobility, however, work functions are similarly high. The changes induced by the heat treatment are not substantial enough to be able to create a junction between the as-deposited and the annealed material, as is revealed by Kelvin probe and Hall Effect measurements.

Heterojunctions between P3HT and Pb_3O_4 were made to test predictions made by KP measurements. A heat treatment on P3HT improved its electronic properties and raised the Fermi level, resulting in the transformation of a diode in to a photovoltaic device and a decrease in dark current.

Acknowledgements

Firstly I would like to thank my supervisors Dr Andrew Watt and Dr Hazel Assender for the opportunity to work with them and their continuous support throughout the project. Andrew, thank you for going on this journey with me, I've learned so much about science and life. Thank you for being the core of such a loving group of people.

Hazel, thank you for your critical and constructive feedback all these years. Your steady and focused approach has often helped to bring me back on track when everything seemed to be going wrong.

For all your help with equipment issues, set-up and repair work on the vacuum systems I owe a huge thanks to Richard Turner, Andy Cook and John Topping.

I would like to thank Professor John Sykes for allowing me to use the Kelvin probe in his lab, and David Lee for making these otherwise lonely hours so much more enjoyable.

Thank you also to the department staff for all your help: Laurie Walton in the workshop, Richard Cripps with some of the electronics, Lyn Richmond for being such a friendly face at reception and Paul Warren and Chris Akinola for IT support.

Thank you for such a warm welcome to the group: Alex, Richard, Elva, Shawn, Peter, Simon, Chris and Shek, and the others who joined later, Jenna, Cheng, Lou, Simon B., Miri, Tom, Maria, Dan, Natasha, Assia, Inji, Darren and Camden, it has been such a pleasure to spend my days with you over the last years, in and outside the lab. I consider myself very lucky to have found

friends like you that were there for all the ups and downs: Chris, thank you for keeping me on my toes and making sure I keep it real, and for keeping the lab tidy. Simon, it was good to be in the same boat with you.

Thank you to my dear friends Elsbeth and Sophie, for all the fun times and for sticking around through the not so fun ones, and to Jeannine for bearing with me in these final days. Luis, thank you for your confidence, for believing in me and for your encouragement throughout this time. And Dansie, seeing the world through your eyes is just heaps good.

Thank you to my family, for your patience, for creating a home open for curiosity and exploring, and for showing me to be respectful with others and the world.

Declaration of Originality

This thesis is an account of work carried out by the author in the Materials Department, University of Oxford under the supervision of Dr Andrew Watt and Dr Hazel Assender. Where the work of others has been drawn upon this is duly acknowledged in the text, and a list of references is presented at the end of the thesis. No part of this thesis has been submitted towards the completion of another degree at the University of Oxford or elsewhere. Parts of this thesis have been published in the following scientific journal:

Laura M. Droessler, Hazel E. Assender, Andrew A.R. Watt, Thermally deposited lead oxides for thin film photovoltaics, Materials Letters 71 (2012) 51-53.

- *Für meinen Papa.*

Contents

1. Introduction

1.1. PV Market

A secured and sustainable supply of energy is indispensable for the perpetuation and development of prosperous and modern societies. For a continued use of fossil fuels however, the depletion of fossil fuel reserves, environmental concerns including global warming, political and military conflict and significant fuel price rise are the main predicted consequences [1].

Several studies have been made that indicate that the peak year of oil production has passed already [1]. What remains is solar energy and all forms of energy resulting from it, like photovoltaics, wind energy, hydro power and biomass. The sun is a fusion reactor that has been operating maintenance free for four and a half billion years, and will continue to do so for another three and a half billion years. Every day it provides more energy than mankind consumes in one year in the form of fossil fuels. The utilization of those renewable resources is a chance to meet the demand for energy that is constantly rising and will continue to rise due to increasing population and modernisation. Emerging economies including China and India account for almost two thirds of the increase in world energy use and are expected to double

their energy demand by 2025 on a 2002 baseline [1]. In China renewable energy shows an annual growth rate of 25% in wind power, solar, wave, tidal and biomass power. Likewise, India shows a big renewable energy potential of which, despite significant achievements in solar, biogas and wind energy, only a fraction of a few per cent has been utilized so far [1]. But renewable energy markets have seen rapid growth and costs have fallen dramatically [2]. Long term scenarios postulate that with appropriate policies and new technology developments renewables could reach up to 50 % of the total share of mid-21st century [1]. Comparing PV, wind and biomass energy, de Vries *et. al.* assess the technical potential of PV to be substantially higher than the other two main sources of renewable energy, wind and biomass [3].

Asif *et. al.* report a total annual world energy consumption of ca. $1.2*10^{17}$ Wh in 2004 [1], de Vries *et. al.* suggest a world electricity consumption of $1.3*10^{16}$ Wh in 2001 and estimate a technical potential for photovoltaics (PV) of $4*10^{18}$ Wh in 2050 [3]. Using learning curves from a wide range of technologies and sectors that demonstrate a fall in prices with increasing cumulative production, cost for 1 kWh is estimated to fall to 0.06-0.25 $ by 2050 [3]. Other groups give more conservative predictions, but also estimate the potential for long-term cost reduction for PV through market growth and innovation to be enormous [2]. Appropriate policies and progress in research are necessary to reach a high market share and decrease cost [4]. Good policies have been implemented in many countries, pioneered by Germany and Japan, where market development is advancing quickly [1, 2, 5].

This literature review will outline the current photovoltaic technologies and thin film systems in particular. The focus will be set upon the challenge of finding new materials systems that fulfil

the economic and sustainability requirements for large scale photovoltaics deployment, develop requirements from photovoltaic principles to materials science aspects and look at the potential of photovoltaic application of a particular class of metal oxides.

1.2 Existing Technologies

A range of technologies exists on the PV market, including wafer-based silicon, a variety of thin film technologies and more recently polymer solar cells, quantum dot technologies and tandem and multi junction cells.

1.2.1. First generation PV

First generation PV cells are single-junction solar cells based on single crystal or polycrystalline silicon wafers. They have profited considerably from the processing know-how gained in the integrated circuit industry, and are the dominating technology on the PV market. The efficiency of commercial single crystal cells lies in the range of 18-20 %, and for polycrystalline cells, which account for more than 60 % of the world market, at 13-14 % [6].

Half of their overall cost is the cost of the 200-250 μm thick wafer material, so that the reduction of wafer thickness is one potential route to cost reduction. A reduction of production cost will also be achieved through up-scaling, smarter processing and shorter manufacturing learning curves. However, the cost reduction trend will most likely reach its limits before cost competitiveness with conventional energy sources is achieved, although relative cost reduction will still be present due to spiralling energy cost [6, 7].

Understanding the nature of defects resulting from crystal growth and processing and treatments to minimize carrier losses are the focus of current research for further improvement of first generation solar cells [5].

1.2.2. Thin Film PV

Second generation thin film technologies are single junction devices using less material while maintaining the efficiencies of first generation cells. The leading technologies use CdTe, CIGS ($CuIn(Ga)Se_2$), amorphous-Si which have a market share of about 17 % [8]. Those materials can be used in thin film solar cells since they have much higher absorption coefficients than crystalline Si (c-Si), so that films with thicknesses in the range of μm are enough for efficient absorption and far less material is used for their production.

The main research interests for thin film PV materials and concepts are the better understanding of interfaces and new multijunction designs, as well as low-cost, high-

performance transparent conductor oxide (TCO) materials and the development of new module concepts [7].

Big advantages of thin film solar cells are the low materials utilization, simpler manufacturing technology for large-area modules, fewer processing steps and better energy economy for production and product recovery [5, 6, 9].

1.2.3. Advantages of thin film systems

A number of methods exist for thin film deposition, that range from simple thermal evaporation over multi source evaporation, physical and chemical vapour deposition to electrochemical, plasma based and hybrid techniques [5, 7, 10]. Depending on these production techniques and the chosen parameters and substrate materials, the microstructure of the films can be adjusted from amorphous or nanocrystalline to highly oriented or even epitaxial growth or large grains [7, 11]. Although a high number of interfaces and grain boundaries generally deteriorate the efficiency of a solar cell, the interfaces can be controlled and passivated or modified to provide for example diffusion barriers, and the design of thin film solar cells makes different types of junctions feasible. Lattice constants, composition, band gap and other optoelectronic material properties can be graded for multicomponent materials [12-14].

1.3. Material constraints

The photovoltaic (PV) sector has reached a billion dollar scale in some countries, undergoing staggering growth. It is no surprise that photovoltaic technology has therefore aroused the interest of the financial sector and it seems possible that economic arguments rather than environmental arguments will push PV energy into the mainstream [6]. To reach this goal, the cost/W ratio will have to be reduced drastically and cost reduction remains the prime goal of the PV sector [5, 6, 15].

Growing Si single crystals is expensive whereas thin film materials can be produced on large area and fast throughput, typically via physical or chemical deposition techniques, so that second generation thin film solar cells show the potential for much lower cost fabrication [5, 6, 15]. However, the leading second generation PV cells are made of copper indium gallium diselenide (CIGS) and cadmium telluride (CdTe), and the use of rare elements will soon limit their production due to material scarcity [16, 17]. The reserve of indium in zinc deposits for example is expected to satisfy the world demand for only another 20 years. Further demand will have to be met by extending the reserve base by additional indium reserves in copper, lead and tin ores and the use of recycled secondary indium, thereby raising the cost of the raw material [18].

For PV to become a viable alternative it will have to become a far larger industrial sector. A growing need exists for the development of new second generation solar cells using new

materials systems that use materials that are abundant and entail low energy cost [15]. Wadia *et al.* evaluated the component cost contribution of 23 potential inorganic PV materials and reported a range in cost of up to 5 orders of magnitude between conventionally used thin film PV material like GaAs, CdTe and CIGS, and oxides and chalcogenides based on Cu, Pb, Zn and Fe, which are much cheaper and show great potential for future PV developments [15]. Their comparison of cost per Watt for potential materials for large scale photovoltaics is illustrated in Fig. 1.

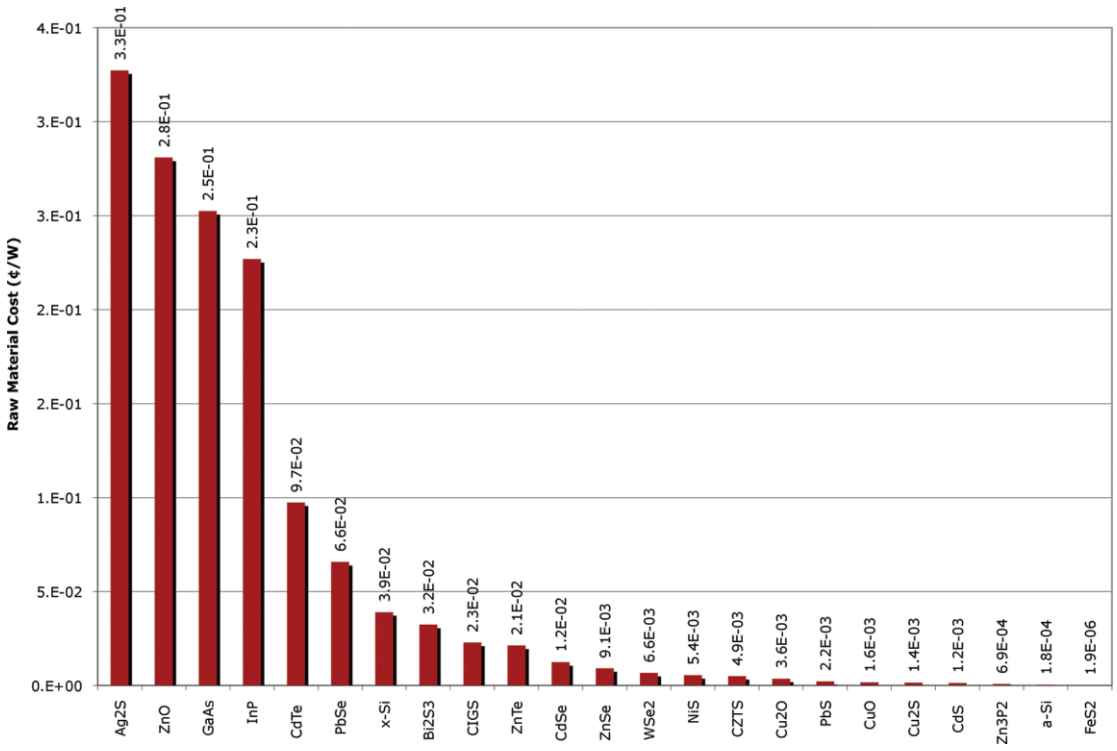

Fig. 1: Minimum cost of material extraction/Watt for potential inorganic photovoltaic materials. Several metal oxides and sulphides show costs three and more orders of magnitude lower than conventional materials used for the fabrication of solar cells [15].

1.4. Desired material properties for PV applications

For efficient solar energy conversion several requirements have to be fulfilled. Efficient light absorption, efficient charge separation, transport and collection are the essential requirements. What this means for materials properties will be elucidated in the following:

1.4.1 Band gap

First of all, the material needs to have an energy gap E_g, which separates the usually occupied electronic states from the usually unoccupied states [14]. In indirect band gap materials, the maximum of the valence band (VB) is found at different k-vectors than the minimum of the conduction band (CB). The smallest distance for band transition from valence to conduction band is hence shifted away from the location of the valence band maximum. In this case, a band transition must involve the absorption or emission of a phonon, which makes the process much less likely to occur, and the overall absorption of light is inefficient. Hence, the effective absorption of photons is only possible in direct band gap materials [7, 14].

Semiconductors have energy gaps between 0.5 and 3 eV, which corresponds to the energy range of visible photons, and can therefore absorb visible light and excite electrons across the band gap.

For a fixed incident spectrum, the spectrum of the sun, an optimum band gap can be determined. For small band gaps, the voltage created by lifting electrons across the gap will be small. For large band gaps the photocurrent will be small, since fewer of the incoming photons will have energies higher than that of the gap and will be able to excite electrons to the conduction band [14]. The optimum band gap for a single band gap photoconverter and the standard AM1.5 solar spectrum lies at 1.4 eV, which results in a maximum theoretical power conversion efficiency (PCE) of 33 %. For high theoretical power conversion efficiencies the band gap should lie in the range 1-1.6 eV, or in the range 0.7-2 eV for PCE of 20 % or higher [14].

1.4.2. Absorption

The material should be a good light absorber with solar optical absorption around 10^5/cm. The optical depth of a semiconductor is increased with increasing thickness of the film, and for most semiconductors almost perfect absorption can be obtained for material thicknesses in the μm range, which is of the order of the inverse of the optical absorption coefficient. For good absorption the optical depth should be high for energies above the band gap, and reflectivity should be small [7, 14].

However, high absorption alone does not result in an efficient photoconverter. The crucial factor is the external quantum efficiency (EQE). EQE does not only depend on the material's absorption of light, but also on the collection of charges. After a photon has been absorbed in the material and has created an electron-hole pair, the charges have to be separated and

collected at the junction. At the same time charge recombination has to be avoided to the highest possible extent to reach a high EQE [7, 14].

1.4.3. Charge separation

After an electron is excited to a higher energy level, leaving behind a hole in the valence band, the two charge carriers have to be separated and recombination must be inhibited. It is therefore necessary that the material can form a good electronic junction (homojunction, heterojunction or Schottky junction) with a suitable material to create a spatial asymmetry that drives the electrons to one side and the holes to the opposite side. This spatial asymmetry can be an electric field or a gradient in electron density, and is given at the interface between two electronically different materials or differently treated layers of the same material. This built-in bias should be large, and charge recombination should be as slow as possible [7, 14].

Fig. 2 outlines the charge creation and separation at a junction.

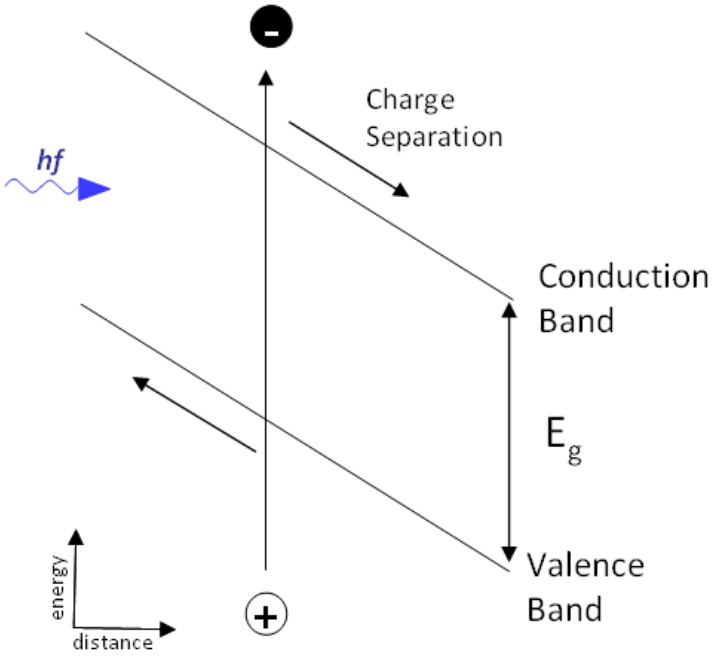

Fig. 2: Sketch of charge creation and separation.

1.4.4. Charge transport

The material should be a good conductor in order to deliver the charge carriers to the external circuit without considerable losses. Defects and impurities act as recombination sites and their number has to be kept as low as possible to achieve long diffusion lengths, which corresponds to long minority carrier lifetime, and low recombination velocity. Series resistance leads to resistive loss and should be as low as possible, parallel resistance prevents current leakage back across the junction and should be high.

The electrodes connecting the junction to the external circuit should be excellent conductors and provide a good ohmic contact to the external circuit [14].

1.5. State of the art thin film PV

Although from a processing point of view elemental materials should be favoured for the manufacture of solar cells, there is no elemental semiconductor available with a direct band gap close to 1.4 eV. A wider range of materials with suitable band gap and optical absorption can be found amongst two component alloys, which are therefore investigated and used for thin film photovoltaic applications. While thin film PV manufacturing costs have dropped by more than 80 % since the early 1990s, manufacturing capacity has been rising at fast pace [7, 10, 14].

For several decades the main focus of research for thin film photovoltaic devices has been on high efficiency systems like amorphous silicon (a-Si), $CuInSe_2$ (CIS) and $CuIn(Ga)Se_2$ (CIGS), and CdTe. Those devices are therefore the most understood and developed thin film systems that deliver the highest power conversion efficiencies of up to 20 % [14, 19]. CIGS, CIS and CdTe are polycrystalline thin film systems and will be discussed here in more detail.

CIGS, CIS and CdTe solar cells can be produced by several processing methods, such as physical vapour deposition (PVD) [7, 20], close-space sublimation (CSS) [21-23], screen printing [24], electrodeposition [25] and spray pyrolysis [26, 27]. The materials are direct semiconductors, with more or less ideal band gap values of 1 eV for CIS, 1.1-1.6 eV for CIGS and 1.5 eV for CdTe. In CIS, the substitution of In by Ga leads to a continuous increase of band gap over a wide range of composition, which explains the possible range of band gaps for CIGS. Substitution of Se by S shows the same effect, but is not commonly used due to the difficulties in controlling the sulphur during deposition [7, 10]. CIS has an absorption coefficient higher than 5×10^4 cm^{-1} at room temperature for photon energies above 1.4 eV and mobilities and carrier densities were reported at 15-150 $cm^2V^{-1}s^{-1}$ and 0.15-2 x 10^{17} cm^{-3} respectively for p-type material, and 90-900 $cm^2V^{-1}s^{-1}$ and 1.8×10^{15} to 5×10^{17} cm^{-3} for n-type material at 300 K. Electronic transport in $Cu(InGa)Se_2$ is dominated by intrinsic defects [28, 29]. Polycrystalline material provides a large number of interfaces in the form of grain boundaries that act as recombination sites. In $Cu(InGa)Se_2$, the grain boundaries parallel to the current flow can be electronically modified through heat treatments and oxygen doping. This process makes the grain boundaries more p-type than the bulk material and inhibits recombination for electron minority carriers [10].

CIGS cells are grown on a substrate containing a Mo contact. The p-n junction is formed by a p-type $Cu(InGa)Se_2$ absorber layer and an n-type CdS window layer and followed by a transparent conductive oxide (TCO) top contact [5, 7]. In $CuInSe_2$-based cells a p-n junction is obtained with a p-type $CuInSe_2$-layer together with an n-type CdS film. CdS has a band gap of 2.4 eV and is an n-type semiconductor. The CdS film is very thin, with thicknesses in the range of 0.05 µm, and lets light pass with small absorption. It does therefore also serve as a window layer for the

device [10, 14]. The carrier density in CdS is much larger than in $CuInSe_2$ and the depletion field, where electron-hole pairs are generated, is therefore entirely in the $CuInSe_2$ region, which minimises recombination at the interface [10]. Furthermore, the diffusion of Na from the soda lime glass substrate and incorporation into the absorber layer enhances the performance of CIGS cells. It is believed that Na reduces the resistivity of the film [5], although there is no definite explanation for the effect [10, 30]. Other models suggest that Na leads to an increased grain size and a reduction of intra-granular lattice defects and a strong orientation of the film. These phenomena are discussed in detail in [31]. Furthermore, the presence of Na widens the α-($CuInSe_2$) phase in the phase diagram and increases the tolerance for deviations in stoichiometry [11]. Efficiencies of 19.5 % [32] and 20 % [33] have recently been reported for CIGS cells.

CdTe cells have structures similar to CIGS cells. The junction also consists of an n-type CdS window layer and a p-type, in this case CdTe, absorber layer. However, CdTe cells operate in a superstrate configuration, where the light enters through the glass on which the cell is grown [5]. The absorption coefficient of CdTe is very high with a value of 5×10^4 cm^{-1} at room temperature for photon energies above 1.8 eV [10]. CdTe can be doped n- and p-type. In on Cd sites forms donor levels at 0.60 eV below the conduction band whereas Cu, Ag and Au introduce acceptor levels 0.33 eV above the valence band [10]. Mobilities of 1100 $cm^2V^{-1}s^{-1}$ and 80 $cm^2V^{-1}s^{-1}$ have been reported for electrons and holes respectively [10]. High efficiency CdTe photovoltaic cells have been reported with PCE of 15.8 % [34] and 16.7 % [19, 35].

Although thin film photovoltaics research has been focusing on these systems in the past decades, aspects remain that have not been fully understood. The main research questions for

the future are the influence of processing on the device performance, the exact role of the buffer layer and its influence on interfacial energies and the understanding of device interfaces to allow for the improvement of transport properties, the quality of the junction and to reduce losses due to surface and interface recombination. Further cost reduction could be achieved for systems that only require one deposition process for all layers [7, 10, 14, 36].

One non-commercial promising technology is thin film solar cells based on $Cu_2ZnSn(S,Se)_4$, known as CZTSSe, as light absorber, using only non-toxic and abundant materials [37, 38]. These cells generally have a substrate/Mo/CZTSSe/CdS/ZnO/TCO structure [38, 39]. Vacuum deposition allows for good control of the phase composition and devices with 6.7 % efficiency have been achieved [40]. The addition of selenium allows for tuning of the band gap and leads to a broader spectral response [38]. Device efficiencies of these cells have been pushed beyond 11 % [39]. Further improvements are expected to be obtained with a better understanding of processes happening at the interfaces, the nature of defects and a reduction of the material's high series resistance [37].

More recently, remarkable results have been achieved in the development of lead iodide based perovskite solar cells with efficiencies up to and exceeding 10 % [41-47]. In these structures a mesoporous alumina is used as an inert scaffold to structure the perovskite absorber and force the electrons to travel through the perovskite [46], leading to "exceptionally few fundamental energy losses" [46]. Perovskite devices that operate as conventional thin film cells, using a homogeneous $CH_3NH_3PbI_3$ film as absorber and TiO_2 as electron collecting contact and spiro-OMeTAD (2,2',7,7'-tetrakis-(N,N-di-p-methoxyphenylamine)9,9'-spirobifluorene) and gold as hole collecting contact were recently reported to reach power conversion efficiencies as high as

15 % [48]. In these devices charge separation and charge transport of both carrier species take place in the perovskite absorber, showing internal quantum efficiencies of nearly 100 % [41].

1.6. Metal Oxides for Photovoltaics

Currently metal oxides mainly find application in photovoltaics as transparent conductive oxide (TCO) electrodes in thin films devices or as electron transport layers, while not many have been used as the active light absorbing layer [47]. The advantage of using metal oxides (MOs) is the "nearly unlimited" number of possible compositions, many of which possess band gaps close to the ideal for single junction solar cells. They are chemically stable and can be processed at atmospheric conditions and are abundant and non-toxic or at least show lower toxicity than elements like Cd, which is currently widely used [47]. Challenges are presented by low mobility and carrier lifetime [47].

Nanostructured devices such as dye-sensitized solar cells or quantum-dot sensitized solar cells use nanostructured MOs for electron collection, coated with a light absorbing layer from which electrons are injected into the metal oxide [49, 50]. Materials used include TiO_2 [51], ZnO [52], SnO_2 [53], $SrTiO_3$ [54], Nb_2O_5 [55] and ZrO_2 [56]. Fe_2O_3 has shown some success in photoelectrolytic devices [57-59] but to date shows very low efficiencies in Fe_2O_3-ZnO solar devices [47].

All-oxide PV devices have been made based on $BiFeO_3$ [60-63], Co_3O_4 [47] and CuO/Cu_2O, whereas Cu_2O cells show the highest performance to this date and are hence discussed in some more detail here:

Cu_2O is a p-type semiconductor with a band gap of about 2 eV, which results in a maximum theoretical power conversion efficiency of roughly 23 % [47]. Schottky junctions are limited in V_{OC} due to the reduction of Cu_2O at the metal interface, resulting in a Cu_2O-Cu junction regardless of the back electrode material [64] with values lower than 0.6 V [65, 66]. A similar effect was found in ZnO-Cu_2O heterojunctions [67] although efficiencies up to 4 % have been reached in cells with an intrinsic n-type ZnO window layer [68, 69]. Nanostructured interfaces were successfully shown to improve charge collection [70] but device efficiencies remained low due to the incompatibility of ideal dimensions of nanostructure spacing for charge collection and thickness necessary for full barrier formation at such low carrier concentrations [71].

All in all, promising PCEs have been reached with Cu_2O cells while other systems still remain low. However, with the vast number of potential metal oxide PV materials this materials group is expected to have a significant impact on future PV research [47].

1.7. Effect of grain boundaries in multicrystalline PV systems

Polycrystalline semiconductors always contain unintentional lattice defects and grain boundaries that can have major detrimental effects on the performance of a solar cell, if they introduce additional energy levels in the band gap.

In a doped material defects at grain boundaries introduce space charge regions. These result from the trapping of charge carriers that create a fixed charge at the interface, leaving behind an oppositely charged, depleted region. This leads to reduced majority carrier mobility and enhanced minority carrier recombination. Fig. 3 shows a sketch of the band bending and depletion at a grain boundary of an n-type semiconductor with an interface neutrality level lower than the Fermi level of the semiconductor.

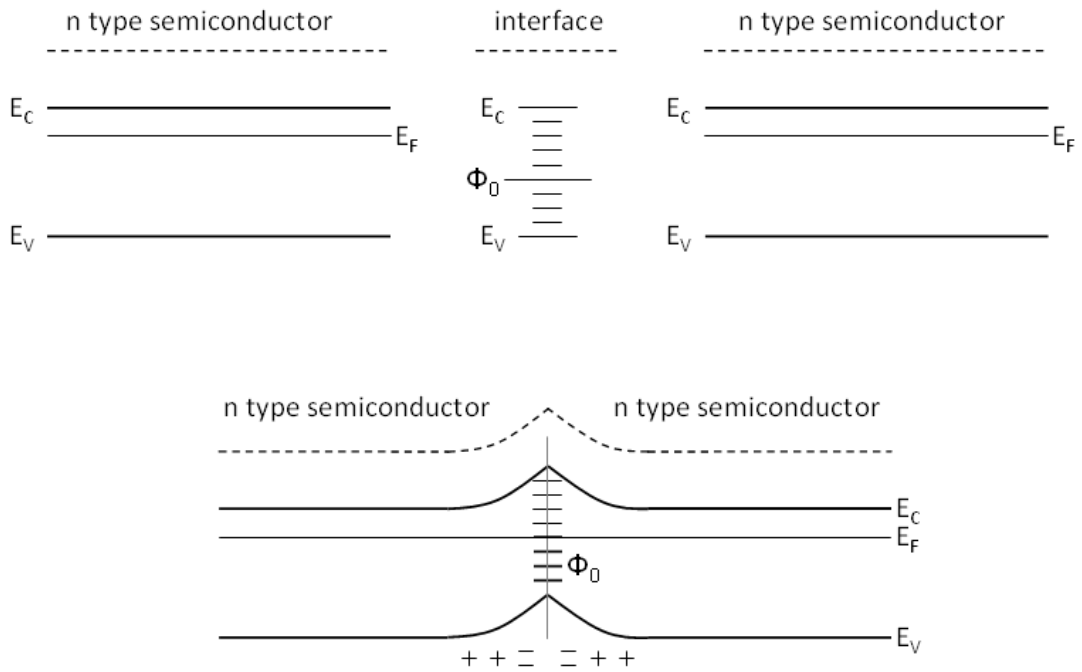

Fig. 3: Band bending at a grain boundary for an n-type semiconductor. Depletion results for interfaces with neutrality levels lower than the Fermi level of the surrounding semiconductor [14].

Broken bonds and intrinsic impurities deposited from the external environment or concentrated during growth introduce additional defects at hetero interfaces that act as recombination sites and reduce the open circuit voltage [14]. Recombination paths and pinholes exist along the grain boundaries which lead to a strong loss in performance for cells with large grains. Hydrogen treatments are widely used to improve the electronic properties of a variety of polycrystalline materials from Si to metal oxides [38, 44, 48, 72]. Upon annealing in hydrogen atmosphere [48, 72] or treatment with hydrogen plasma [38, 44], hydrogen is known to passivate dangling bonds or lead to the desorption of negatively charged oxygen species from surfaces and grain boundaries, which act as carrier traps and recombination centres. This

treatment has been shown to increase carrier concentration by half an order of magnitude in Al doped ZnO [72] and two orders of magnitude in nitrogen doped Cu_2O [44] while decreasing resistivity.

1.8. Lead oxides

1.8.1. Known phases of lead oxide

The first polycrystalline thin film lead oxide in a rectifying Schottky barrier junction photovoltaic device was recently demonstrated by Darbe *et al.* [73]. Lead oxides exist in a range of stoichiometries and it is well known that the lead to oxygen ratio determines the band gap [74].

There are two forms of Pb(II)O, litharge and massicot, that are both stable at ambient pressure. Litharge is the lower temperature type of the two crystalline forms of PbO. Litharge is red, with a tetragonal layered SnO structure. It is produced by heating Pb to about 600°C in air or O_2 [75, 76]. The range of homogeneous compositions for tetragonal PbO has not been determined concordantly, and propositions lie in the range of 49.9 – 52.4 at % O [77]. Massicot is the higher temperature phase of PbO. It is yellow, with an orthorhombic chain structure and is stable

above 488°C [75, 76] and up to the melting point at about 890°C [77]. The relative phase stability of litharge (PbO_{tet}) and massicot (PbO_{orth}) is very sensitive to impurities [78] and discrepancies exist in the literature concerning phase transition temperatures [77]. White *et al.* studying the effect of hydrostatic pressure on the transformation temperature from PbO_{tet} to PbO_{orth} [79, 80] determined that higher pressures stabilize PbO_{orth} and that at 0.1 MPa hydrostatic pressure the two phases are in equilibrium at 543°C. Different groups have investigated the range of stoichiometry for PbO_{orth} and it is believed to lie within 49.95-53.1 at % O [77]. Crystallographic unit cells of the the PbO phases are displayed in Fig. 4.

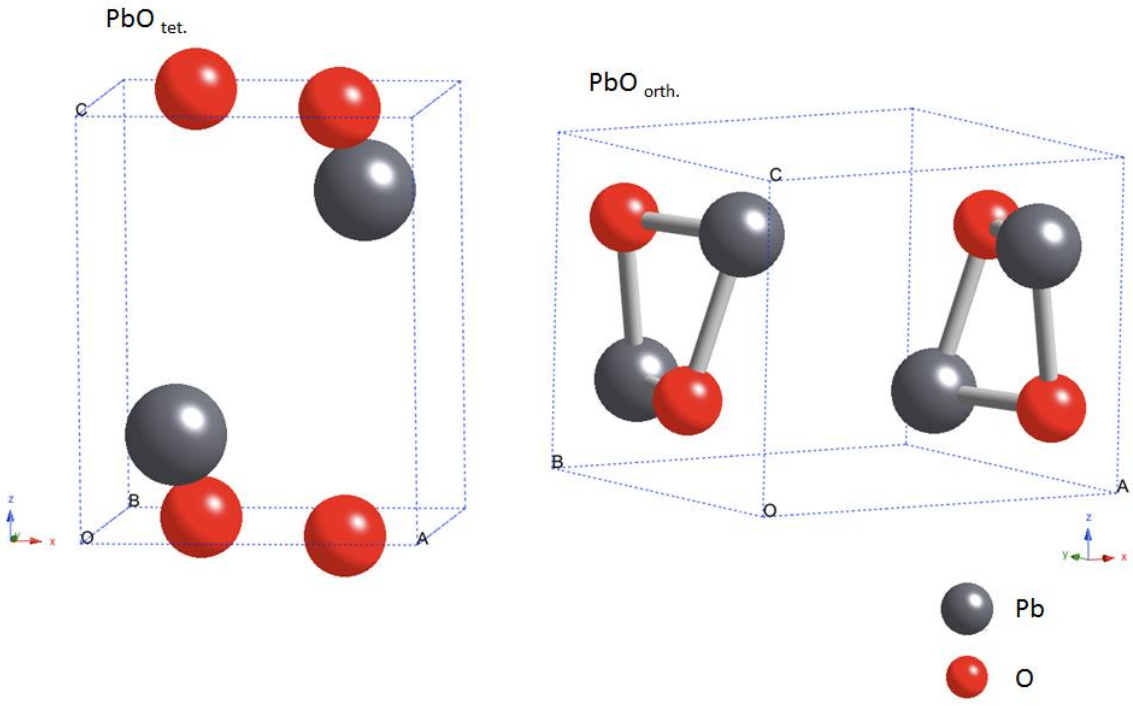

Fig. 4: Unit cells of tetragonal and orthorhombic PbO.

Pb_3O_4 is called minium or red lead. It is a mixed-valency oxide and behaves chemically as a mixture of Pb(II)O and $Pb(IV)O_2$ [75, 76, 81]. In Pb_3O_4, the $Pb(IV)O_6$ octahedra form chains sharing opposite edges, that are linked by the Pb(II) atoms, pyramidally coordinated by three oxygen atoms. It can be obtained by heating PbO in air at 450-500°C [76]. Wriedt [77] reports a black tetragonal Pb_3O_4 phase (Pb_3O_4-T), stable above -103°C, which dissociates into Pb_2O_3 and PbO in conditions of elevated pressure without O_2 exchange and furthermore an orthorhombic low temperature Pb_3O_4 phase (Pb_3O_4-R) that is stable between -268°C and -103°C. Its unit cell is shown in Fig. 5.

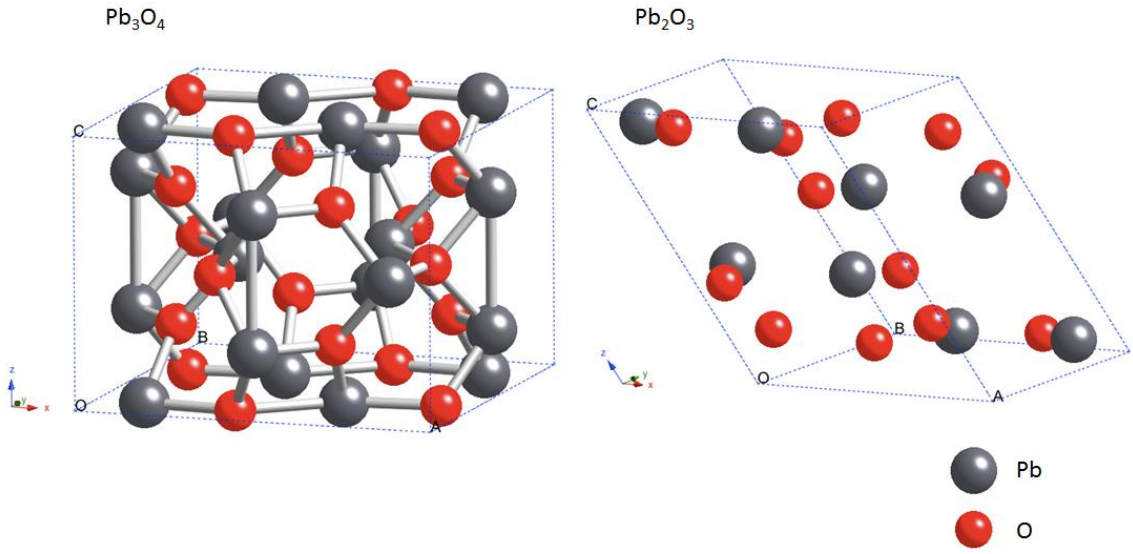

Fig. 5: Unit cells of Pb_3O_4 and Pb_2O_3.

A $Pb_{12}O_{17}$-phase is described in the literature that has not been characterised definitely. It has been reported as both orthorhombic and cubic, and also appears under the name β-PbO_x [77].

$Pb_{12}O_{19}$ has also been described under several different terms, namely Pb_5O_8, Pb_7O_{11}, Pb_9O_{14}, α-PbO_x, β-PbO_x, $PbO_{1.57}$ and $Pb_{12}O_{19}$. This variety of similar stoichiometries was attributed to $Pb_{12}O_{19}$ due to the breadth in homogeneity range of this phase [77]. $Pb_{12}O_{19}$ has a monoclinic crystal structure that forms dark-brown or black crystals [76].

The highest oxide of lead known is PbO_2. Three structures exist for Pb(IV)O_2, whereas only one of them is stable at ambient pressure [77]. PbO_2 cannot be oxidised from any starting material at atmospheric conditions and is usually prepared using aqueous oxidizing agents or leachants or is obtained though electrolysis [77, 80], but its formation as a thin film in air was reported by Bragg *et al.* [82], who dipped a thin Cu wire into melted Pb that was then slowly withdrawn. The maroon-coloured ß-PbO_2, or PbO_2-I, has a tetragonal, rutile structure [76, 83]. Small amounts of hydrogen suggest the existence of hydroxyl ions and could be an explanation for the inability to reverse the decomposition of PbO_2 into $Pb_{12}O_{19}$ due to the lack of hydrogen as an essential constituent [77, 80].

The high-pressure phase α-PbO_2, or PbO_2-II, is black with an orthorhombic, columbite structure and forms at pressures above about 3 MPa [76, 83]. A third polymorphic form of PbO_2 exists at even higher pressures [77]. Crystal unit cells of the three different PbO_2 phases are shown in Fig. 6.

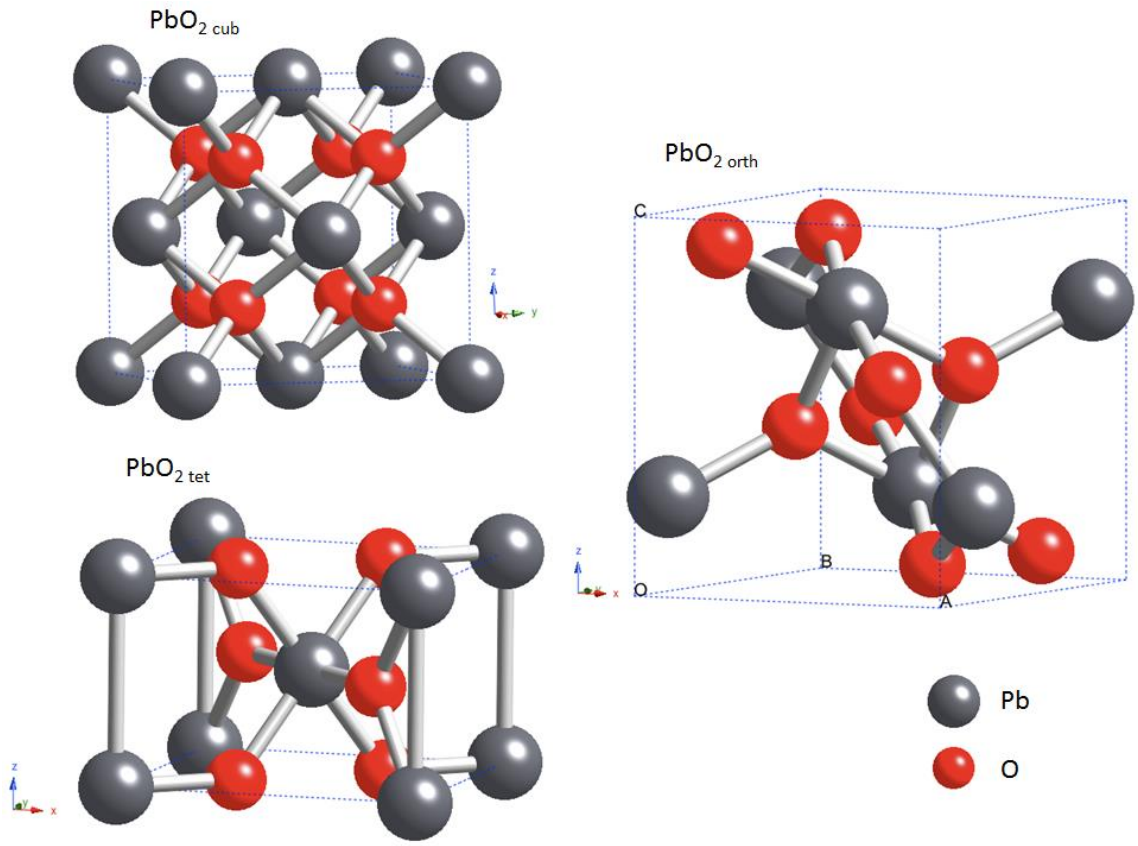

Fig. 6: Unit cells of cubic, orthorhombic and tetragonal PbO_2.

The sesquioxide Pb_2O_3 high pressure phase is a vitreous black monoclinic crystal. It can be produced by decomposing PbO_2 or PbO at about 600°C under an oxygen pressure of 1.4 kbar. In this structure, the Pb(II) atoms are situated between layers of distorted $Pb(IV)O_6$ octahedra [76]. The Pb_2O_3 unit cell is displayed in Fig. 5.

In addition to the described stable phases of lead oxide, a number of metastable phases exist that are described in the literature [77]. The stable phases are listed in Table 1.

Table 1: Known stable phases of lead oxide.

colour	name	stochiometry	crystal structure	band gap	oxide
yellow	massicot, β-PbO	PbO	orthorhombic	2.8 eV	Pb(II)
red	litharge, α-PbO	PbO	tetragonal	1.9 eV	Pb(II)
bright red	minium; red lead	Pb_3O_4	tetragonal	2.1 eV	Pb(II) & Pb(IV)
	$Pb_{12}O_{17}$	$Pb_{12}O_{17}$			
dark brown / black	$Pb_{12}O_{19}$	$Pb_{12}O_{19}$	monoclinic	1.28 eV	
vitreous black	Pb sesquioxide, Pb metaplumbate	Pb_2O_3	monoclinic	1.4 eV	
brown	β plattnerite, PbO_2 - I, plumbic oxide	PbO_2	tetragonal, rutile structure	1.5 eV	Pb(IV)
	α, scrutinyite, PbO_2 - II	PbO_2	orthorhombic, columbite	1.4 eV	Pb(IV)
	PbO_2 - III	PbO_2	cubic		

The binary phase diagram of oxygen and lead is shown in Fig. 7, displaying the equilibrium range of existence for the different stable phases.

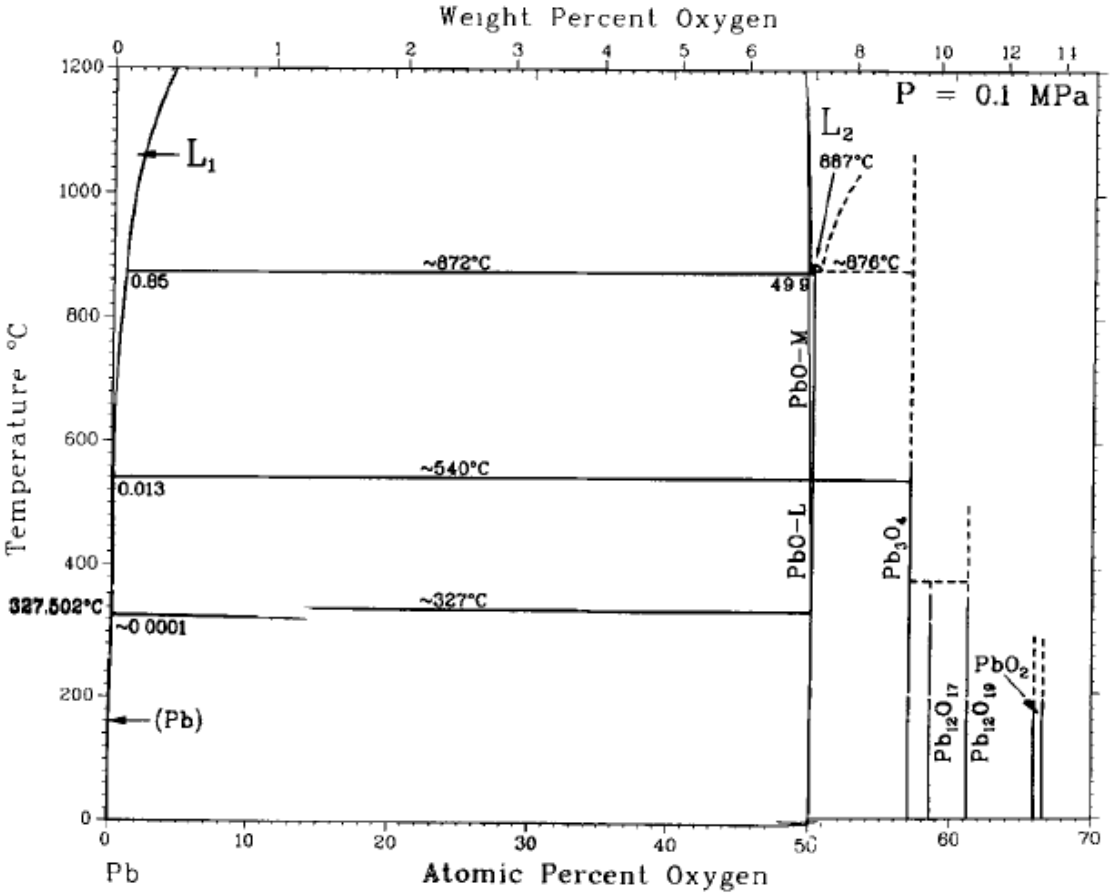

Fig. 7: Oxygen-lead phase diagram (with permission) [77].

Toxicity is always a concern when handling lead, and is a complicated parameter to quantify that needs more investigation [73]. However, lead is less toxic than Cd, that is currently used in the production of solar cells [84]. Recycling can be accomplished through the dissolution of PbO in ethyl acetate and the formation of solid lead acetate [73].

1.8.2. Known electronic properties of lead oxides

A number of lead oxides prepared via the electrochemical route have been found to be photoactive. Pavlov [85] describes PbO_2 as n-type semiconductor with a very high electron conductivity caused by oxygen vacancies O^{2+} and H^+ and Pb^{2+} ions in the PbO_2 structure. PbO_{tet} and PbO_{orth} are also photoactive, although PbO_{tet} is more photosensitive than PbO_{orth} [86]. Munkhopadhyay *et al.* [87] ascribe the photoactivity in PbO-films to nonstoichiometry, a mixture of PbO and PbO_2. The general n-type conductivity is, as in the work of Pavlov, ascribed to oxide ion vacancies. But metal excess phenomena are observed for changed parameters in the electrosynthesis of the film that enhance the charge carrier concentration. This technique enhances the content of PbO and hence the photoactivity of the film. Although the band gap energy remains unaltered, the photoactivity is influenced by surface modifications obtained by a modified electrochemical technique [87]. Charge carrier densities of 5.81×10^{15} cm^{-3} were found [87].

Radhakrishnan *et al.* describe the dependence of photoconductivity in tetragonal PbO_{tet} on heat treatments [88]. The photosensitivity at room temperature is significantly increased and peaks for a heat treatment at 225°C. This increase is due to the creation of new impurity or defect centres through the incorporation of oxygen. The crystallographic and electronic structures of PbO_{tet} and PbO_{orth} are discussed further in detail in [89].

Both crystalline modifications of PbO_2 show low resistivities with 10^{-3} Ωcm for α-PbO_2 and 10^{-4} Ωcm for β-PbO_2. The band gaps of both phases are about 1.4 eV. PbO_2 shows n-type conductivity with electrical conductivity comparable with that of some metals. Electron

densities lie between 10^{20} and 10^{21} cm^{-3} and mobilities are of the order of 100 cm^2/Vsec [83, 90, 91]. The free electrons in the material can arise from a deviation from stoichiometry, the incorporation of hydrogen that forms OH groups that substitute oxygen atoms in the lattice [92] or the presence of other impurities [83]. Since high concentrations of impurities would be necessary to cause significant changes in the carrier concentration, doping of PbO_2 with III- or V-valent ions will not be as effective as in, for example, SnO_2, and the latter is rather unlikely [83]. The mobility in α-PbO, as obtained by Mindt, is lower than in β-PbO, which can be ascribed to the smaller grain size observed in this modification as well as the higher carrier density, which means a higher density of lattice defects on which electrons are scattered [83].

Pb_3O_4 has high resistivity, 10^8 Ωcm for pressed powder [93] and 10^4 Ωcm for a Pb_3O_4 film [94]. Experimental values for the band gap lie between 2.1 and 2.2 eV [81].

1.9. Production of lead oxide thin films

1.9.1. Deposition technologies

Thin film deposition technologies can be divided into three main classes: thermal evaporation – or physical vapour deposition-, cathodic sputtering and chemical deposition. The first two, thermal evaporation and sputtering are relatively cheap and suitable for industrial scale deposition and will hence be discussed in the following. These techniques allow an automatic controlling and monitoring of the deposition rate and film thickness. A number of parameters exist that influence the properties of the films. These parameters vary from technique to technique and include the deposition rate, temperature of the vapour atoms, angle of incidence of vapour, substrate and source material, substrate temperature and the composition of the ambient atmosphere [95].

The crystallite size is an important parameter in thin film photovoltaics and can be influenced significantly by deposition parameters. Increasing surface mobility of adatoms and clusters during deposition leads to an increased crystallite size. Larger crystals are obtained by *e.g.* increased substrate temperature, rate of deposition and inertness and smoothness of the surface [95]. The influences of some parameters on the crystallite size are outlined in Fig. 8.

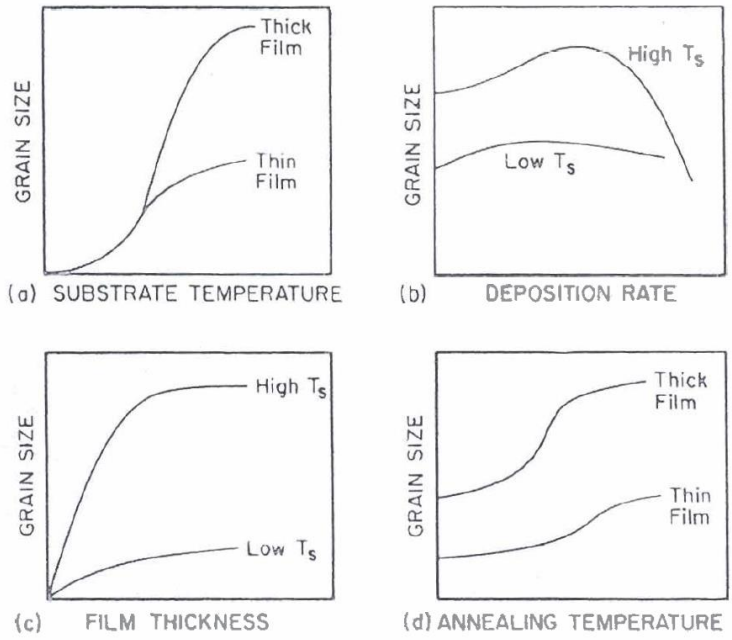

Fig. 8: Dependence of grain size of vapour deposited pure metal films on a.) substrate temperature, b.) deposition rate, c.) film thickness and d.) annealing temperature [95].

It must be kept in mind that the effective substrate temperature is always relative to the melting point of the deposited material. Thermal diffusion of surface atoms on a deposited condensate is a high-activation-energy process, hence the influence of post deposition heat treatments is significantly different from the effect obtained by the same temperature during deposition. The final crystallite size can be influenced considerably by contamination and residual gases. For very high deposition rates, the adatoms show strong interaction with each other and are chemisorbed with little surface migration, leading to a fine-grained film. The dependence of crystallite size on film thickness is more pronounced in the case of higher surface mobility [95].

1.9.2. Lead oxide made via thermal evaporation

Thermal evaporation is simple and convenient and therefore a very widely used deposition method. In thermal evaporation, thin films are obtained by the condensation of vapour onto a cooler substrate. Therefore, a source material is first heated to high temperatures to vaporise in a vacuum system with a chamber or bell jar. The ultimate vacuum and residual gases can, depending on the source material, have a high impact on the structure and properties of the deposited film. A fraction of the vapour atoms can be scattered and randomised in direction due to collisions with ambient gas atoms. Hence a fairly good vacuum has to be established to reach the necessary straight-line path for most of the vapour atoms. For systems with source-to-substrate distances between 10 and 50 cm pressures in the order of 10^{-5} Torr are needed [95]. Thus the rate of deposition depends on the equilibrium vapour pressure of the evaporant, the molecular weight of the vapour species, the condensation coefficient, the source geometry and its position relative to the substrate [95].

IV-VI compounds usually show no or low photoconductivity and low electrical resistivity when vacuum evaporated onto a substrate kept at room temperature. They generally have fine grained structures and an excess of the metal component. Grain size and resistivity increase during subsequent annealing or at deposition at elevated temperatures, and weak photoconductivity can then be measured. Recrystallisation occurs during post-evaporation heat treatments so that homogeneity and uniformity are increased. In order to make these thin

films efficient photoconductors they have to be sensitized or activated by the incorporation of certain impurities through simultaneous or sequential evaporation [95].

1.9.3. Lead oxide made via sputtering

Sputtering is the ejection of atoms from a surface by bombardment with energetic particles. The sputtered atoms are subsequently condensed on a substrate and form a thin film. For a bombardment with positive ions the process is referred to as cathodic sputtering [95].

The average number of atoms ejected from the target per incident ion, the sputtering yield, is proportional to the energy and mass of the ions. A sputtering threshold exists that depends on the sublimation energy [95, 96]. Above the threshold the yield shows a rapid increase and runs into saturation after a short linear region. At very high energies the ion penetration depth increases resulting in higher energy losses and a decrease in sputtering yield. Except for sputtering at very high temperatures, where thermal evaporation accompanies the process, the yield is insensitive to variations of the target temperature. The velocities and energies of the sputtered atoms are considerably higher than of evaporated atoms [95].

Primarily atoms and clusters of atoms are ejected from the target, though some ions can be present. Studies on the sputtering of Cu, Ag and GaAs indicate the ejection of diatomic molecules [95, 97, 98].

Thin film carbides, nitrides, oxides, hybrids and sulphides can be deposited either from a target of the compound, or via reactive sputtering from a metallic target. Reactive sputtering, although it can be more difficult to control, is increasingly favoured due to the higher deposition rates and conducting nature of the target, limiting detrimental arcing effects. The atomic form of stable diatomic species is highly chemically reactive and used in this sputtering process. A mixture of the inert sputtering gas and the reactant is introduced into the cathode region where ions for the chemical reaction are formed in a glow discharge [95]. A study of the reactive sputtering of various metals can be found in [99]. Depending on the pressure of the reactant and the chemical reactivity of the reacting species, the reaction can take place at the cathode, during transport of the ejected atoms or at the film surface, or a combination of these processes. For low partial pressures of reactant the reaction takes place predominantly on the film surface during film growth. The growth rate of an oxide film depends on temperature and increases rapidly with increasing substrate temperature [100].

1.9.4. Magnetron Sputtering

In magnetron sputtering a magnetic field traps the electrons of the plasma to create a confined and densified plasma, enhancing the ionisation efficiency of the cathode. This increases the deposition rate through an increased ion bombardment of the target [101, 102]. The magnets are generally arranged as one planar pole in the centre of the target with the opposite pole as a ring around the edge of the cathode, below the target material [101] resulting in a 'circuit' of

electrons in the plasma in front of the target. This arrangement results in preferential sputtering of material from the region around the sheath, also known as the racetrack, resulting in poor material utilisation of the target. Spatial variation of properties in the sputtered films relative to the position of the racetrack is a common observation [103-106].

The two main types of power supply used are direct current (DC) and alternating current, generally radio frequency (RF) supplies. While DC sputtering can only be used for conducting targets due to charge build up, RF sputtering can be used on insulators since highly mobile electrons can rapidly neutralise the charge build-up on the target surface in a short time [107]. In the case of reactive sputtering from a metal target the formation of an oxide film on the target surface, also known as target poisoning, can lead to such a charge built up and result in cathodic arcing, where macro particles are then ejected from the target [108] and can cause damage to the thin film, thus in some cases RF sputtering may be preferred.

The oxides sputtered in this work are highly conductive and no arc formation was observed in DC sputtering and hence this, more simple, approach was used as deposition method throughout the sputtering experiments.

Venkataraj *et al.* prepared some oxides of lead by reactive DC magnetron sputtering in an Ar-O_2 mixture at different oxygen partial pressures [74]. They observed that with increasing oxygen flow different stoichiometries of lead oxide were obtained. Tetragonal PbO formed predominantly at low oxygen flow rates, increased oxygen flow resulted in cubic $PbO_{1.44}$, a further increase resulted in orthorhombic Pb_2O_3, and finally orthorhombic PbO_2 formed for

high oxygen flow rates. Optical measurements revealed that the energy gap decreases with increasing oxygen flow, see Table 2 [109].

Table 2: Grain size, surface roughness and band gap of lead oxide films deposited via reactive sputtering [109].

Oxygen flow (sccm)	Composition	Grain size (nm)	Surface roughness (nm)	Optical band gap energy E_g (eV)
20	PbO	23.54	3.98	1.89
25	$PbO_{1.44}$	21.08	4.01	1.60
30	$PbO_{1.44}$	52.48	3.79	1.45
35	Pb_2O_3	18.09	4.01	1.39
40	Pb_2O_3	12.79	4.11	1.31
50	PbO_2	6.86	3.69	1.35

The dominant (101) peak suggested an orientation texture in the resulting thin film. Furthermore the possibility of a coexistence of a respective minority phase was not excluded. To study the effect of kinetic constraints on the formation of different oxides of lead, post-deposition annealing studies were carried out. Films of tetragonal PbO were heat treated in a furnace in Ar atmosphere for 1 h between 100°C and 600°C. Venkataraj *et al.* observed that tetragonal PbO persists up to 400°C, showing only grain growth and no structural change. Above 400°C Pb_3O_4 begins to form that coexists with the tetragonal PbO. At 500°C the lattice changes to orthorhombic PbO. The authors explain this using kinetic arguments. The tetragonal

PbO phase originally formed during room temperature deposition has a small heat of formation. The more stable orthorhombic phase has a higher heat of formation and can only form upon annealing when sufficient energy is provided [109].

A second extended study surveys the changes in various other phases of lead oxides upon heat treatment [74]. Thin films of tetragonal PbO, cubic $PbO_{1.44}$, orthorhombic Pb_2O_3 and orthorhombic PbO_2 were prepared by reactive DC magnetron sputtering and annealed in Ar atmosphere. For the PbO, $PbO_{1.44}$ and Pb_2O_3 starting materials grain growth could be observed at temperatures up to 400°C without any phase transformation, whereas PbO_2 only showed pure grain growth up to 300°C and started to decompose to tetragonal $PbO_{1.55}$ above 400°C. All four materials transformed to the most stable phase, orthorhombic PbO, upon annealing at 500°C. An observed decrease of film thickness with increasing annealing temperature indicates a densification of the films. The surface roughness was found to increase with temperature. Band gaps were determined by optical spectroscopy. The findings (Fig. 9) are in good agreement with the previously published data [109], showing lower band gaps for higher oxides of lead. Upon annealing at 500°C all samples show a band gap of 2.8 eV, corresponding with the value for orthorhombic PbO [74].

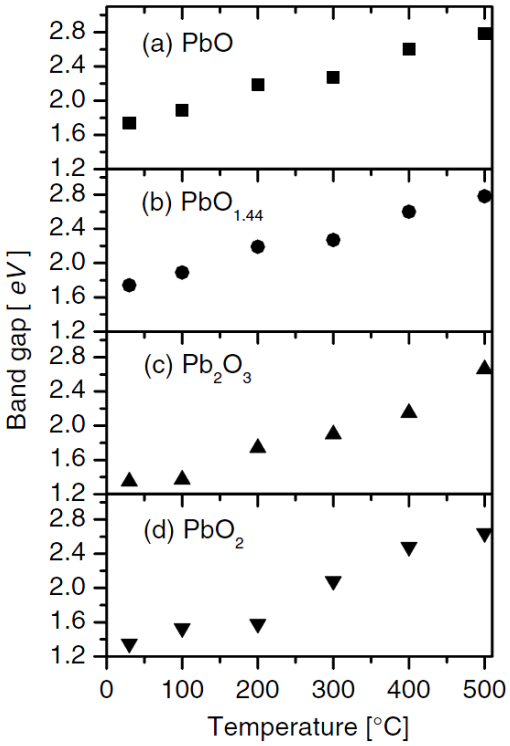

Fig. 9: Band gap E_G as a function of temperature for different starting stoichiometries of lead oxide [74].

1.9.5. Lead oxide thin films for solar cells

A number of theoretical and experimental studies of different forms of lead oxides have been carried out that show interesting optical and electronic properties pointing towards it being a very useful photovoltaic material with strong absorption cross sections and high carrier mobility and conductivity [73, 74, 81, 83, 86, 90, 110-112].

The band gaps of lead oxides vary in a range between 1.4 and 2.8 eV, with higher oxides showing lower band gap values [74, 81, 83]. For the production of Schottky junctions the most interesting stoichiometries of lead oxides will be PbO_2 and Pb_2O_3 that exhibit band gaps of 1.4 eV [74, 83]. This gives a maximal power conversion efficiency of around 20% [43].

In multijunction cells films are layered in order of their band gap, with solar radiation entering the largest band gap layer first. As light passes through the cell each layer absorbs a narrow energy range of above gap photons. Electrons excited to a state in the conduction band by photons with energies higher than the band gap value decay to the bottom of the conduction band within picoseconds resulting in energy being lost for charge extraction, known as hot carrier losses [5]. The multijunction system allows the highest energy photons to be absorbed by the wide band gap material, while the lower energy electrons will pass through this material to be absorbed by the lower band gap material behind. Thus, photons with energies above the smallest band gap energy have a high probability of being absorbed, minimizing below gap losses. The ideal efficiency of the multijunction cell is determined by the number of cells in series and the selection of band gaps [5, 113]. The exploitation of the different oxide phases in a multijunction cell by successive thin film depositions could lead to improved solar cell efficiency.

1.10. Summary and Conclusions

State of the art solar cells face impasses due to either high materials cost or confined materials availability that will prevent current systems from becoming competitive with fossil fuels on a large scale. Systems using alternative materials will have to be developed for a sustainable production of solar energy in the long term. Nevertheless, new solar cell designs can be built on the expertise gained from current thin film systems.

Challenges will be to understand the semiconductor properties and find suitable material combinations to design effective junctions with new “unconventional” materials. For these new systems charge generation, transport and extraction will have to be optimised.

Thin film solar cell research on current solar cell designs mainly focuses on the optimisation of processing for improved performance, all-around understanding of the role of buffer layers and the understanding of interfaces and defects and additional energy levels they introduce. The same challenges will exist for the development of new materials systems.

In a first step, material studies must be performed to find appropriate materials with adequate optical properties that have the potential to form good junctions and to enable the computer simulation of different junction designs. For the production and processing, many approaches known from existing thin film systems and studies performed on the relevant materials can be used for new systems. These include deposition parameters that influence crystal structure and hence band gap, uniformity and degree of crystallinity, as well as strategies for grain boundary

passivation and doping for manufactured properties. Therefore the past research has laid the corner stone for the development of new seminal solar cell concepts.

2. Experiment and Methods

2.1. PV Testing

2.1.1. Sample Preparation

All solar devices were made on a glass substrate coated with a transparent conductive indium tin oxide (ITO) layer serving as an anode. Depending on the device design, one or two thin semiconductor films were then deposited as the active material. Cathode top contacts were thermally evaporated and were usually aluminium, in some cases gold. This setup is outlined in Fig. 10.

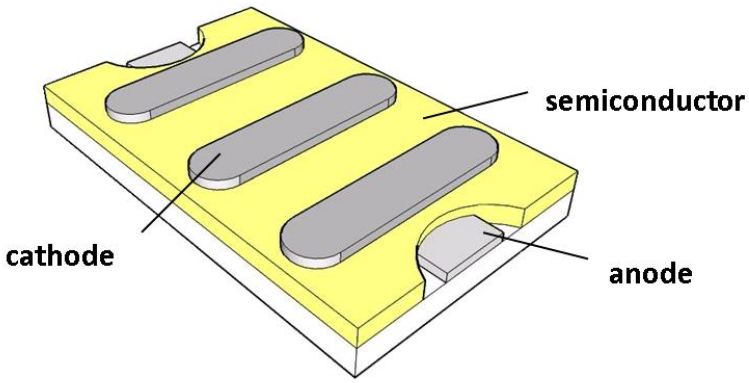

Fig. 10: Sketch of a photovoltaic device structure.

Substrate Preparation

ITO coated glass was purchased from Delta Technologies. The ITO films were 140 nm thick with a sheet resistance of 15 Ω/□. In order to make device substrates the sheets were cut into pieces of 12 x 14 mm on a precision dicing saw. Subsequently, the substrates were patterned to create a 2 mm wide ITO strip running down lengthwise in the middle of the sheet (Fig. 10). This was achieved by covering the desired area with an adhesive mask before etching off the surrounding ITO in aqua regia, a solution of water, hydrochloric acid and nitric acid in a ratio of 25:25:2 at 55-60°C for 6 min. The substrates were then cleaned in a sequence of ultrasonic baths, 0.5 % detergent solution, deionized water, HPLC grade acetone and finally HPLC grade 2-propanol for 5 min each. The slides were then plasma etched for 5 seconds in an oxygen plasma in a Tegal Plasmod.

Thin Film Evaporation

Metal films were deposited in a vacuum bell-jar in an Edwards 306 thermal evaporator at pressures below 10^{-4} Torr. Films were evaporated at rates of 0.1 nm/s for the first 5 nm and the rate was then increased to 3 nm/s. The deposition rate was measured using an Edwards FTM 5 quartz crystal growth monitor, calibration was carried out via thickness measurements using a DEKTAK profilometer. Both Pb for the production of some device active layers and aluminium, and in certain cases gold, for the top cathode were deposited in this manner. For the correct patterning of the cathode a shadow mask was used to deposit three ”fingers” perpendicular to the ITO strip that define the dimensions of 1.5 mm x 2 mm of three solar cells on each substrate, as outlined in Fig. 10. The Pb films were made 300 nm thick to avoid the shorts that often occurred for thinner films. The cathodes were 70 nm thick.

Oxidation of Pb to PbO

Oxidation of the Pb films to PbO for the absorber layer was performed on a hotplate in air. Oxidation times were varied to obtain different stages of oxidation and varied proportions of different oxides. The oxidation temperature was restricted as it was found that the minimum oxidation temperature for thin films of lead was 270°C and ITO resistance started to increase for heat treatments at 300°C and above.

Fig. 11 shows the evolution of resistance as a function of both temperature and time for ITO over-coated with lead. The ITO substrate was coated with a Pb film and the resistance was measured across the slide as the sample was continuously heated, increasing the temperature by 50°C every 30 min up to 350°C, where it was held for 15 hours. It is obvious that heat treatments at 300°C and above lead to the rapid degradation of the ITO bottom electrode: resistances increase from 30 Ω at room temperature (RT) to more than 2 kΩ across the substrate after 15 h at 350°C. This means all photovoltaic processing steps need to take place at lower temperatures if results are not to be dominated by large series resistances. The high conductivity of ITO stems from its large charge carrier densities that are a result of the substitution of indium atoms with tin atoms, each adding one extra electron, and oxygen vacancies that each act as two electron donors. The drastic increase in resistance upon heating in air has also been observed in dye-sensitized solar cells by Ngamsinlapasathian *et al.* [114] and is ascribed to the oxidation of ITO, leading to the removal of oxygen vacancies. This phenomenon leads to a deterioration in solar cell performance with a decrease in fill factor and current and is therefore undesirable. 270°C was hence chosen as the oxidation temperature for the Pb films on ITO.

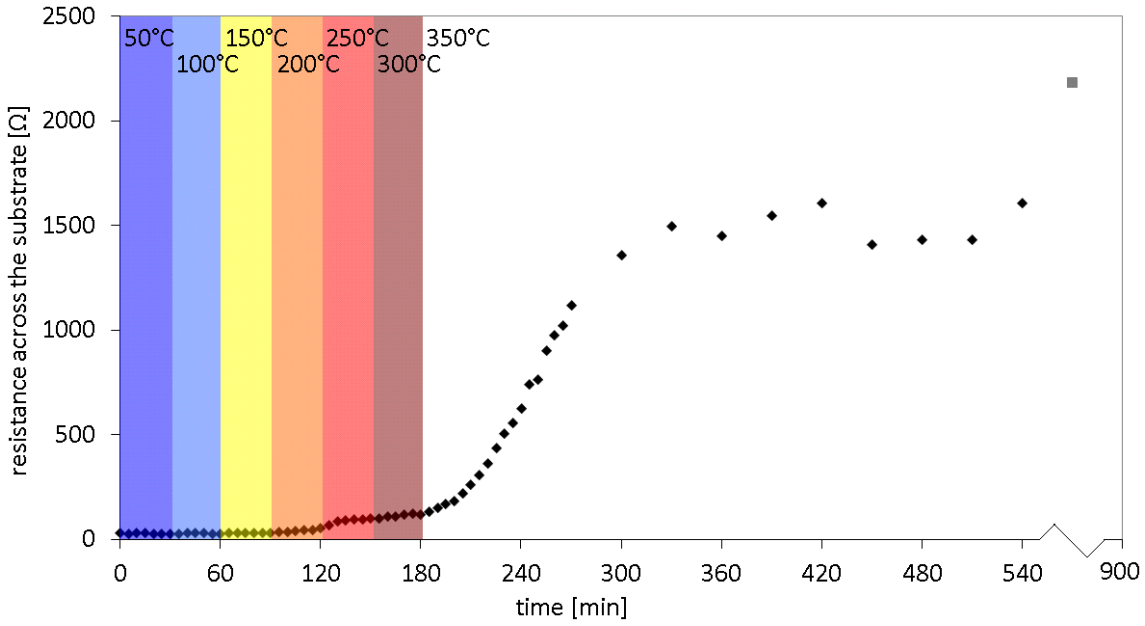

Fig. 11: Increasing resistance of ITO with increasing heat treatment temperature.

Reactive Sputtering of Lead Oxides

Reactive sputtering of lead oxide was performed in a different Edwards 306 deposition chamber set up for sputtering. The dimensions of the cylinder shaped bell jar were 390 mm x 300 mm diameter. The chamber was equipped with Advanced Energy Area mass flow controllers (MFC) with a range between 1 and 200 sccm and accuracy of 0.1 sccm at 50 % range, controlled via an Advanced Energy ROD4 system. Power was supplied by an Advanced Energy MDX unit which operates up to 12 kW. An Advanced Energy SparcLE unit was operated in self-run mode to suppress the formation of arcs.

Sputtering was performed from a Pb target in an oxygen-argon atmosphere. A circular magnetron with a 3” diameter water cooled target was mounted on the top lid of the chamber.

Before every deposition the chamber was pumped down to a base pressure of $5x10^{-5}$ mbar and a 5 min deposition of Pb in Ar was performed with a closed shutter to clean any residual oxide off the target in order to achieve reproducible conditions at the beginning of every sputtering run. All runs were performed at 0.85 A at power levels varying between about 0.12 and 0.14 kW, which was the minimum current necessary to spark a plasma. The voltage varied between 220 and 280 V, depending on the oxygen flow rate and the amount of target poisoning. The absolute flow rate of oxygen and argon was kept constant at 40 sccm for all runs and the pressure was regulated using a throttle valve and kept at $7x10^{-3}$ mbar.

Spin Coating of P3HT

20 mg/mL P3HT was dissolved in 1,2-dichlorobenzene and stirred overnight at ambient temperature in a dry box to ensure the polymer was completely dissolved. The P3HT polymer layer was then spin coated at 1000 rpm on top of the PbO [115].

It should be noted that devices were made in batches with control samples. Due to the inherent changes in processing conditions and quality of aluminium cathode through the project there was some variation in overall device performance, however within batches we take results to be internally consistent. The use of the sputtering and evaporation systems for the deposition of other materials introduces the risk of contamination of the films and had an impact on the reproducibility of results for solar cell performance. In order to reduce variations

between batches a layer of metal was deposited onto the chamber surface before runs to trap organic contaminants.

2.2. JV Measurements

Current-density voltage (*JV*) measurements were performed to determine the power conversion efficiency (*PCE*) and other defining parameters of the fabricated solar cells under white light. Short circuit current (J_{SC}) and open circuit voltage (V_{OC}) can be read directly from the JV curve under illumination, whereas other parameters such as series resistance (R_S) and reverse saturation current (J_0) can be extracted from the dark curve as described below.

The set-up used for this test consisted of a Newport solar simulator equipped with a 150 W ozone-free xenon lamp with an AM1.5G filter, as used in standard solar cell testing. The spectrum is shown in Fig. 12.

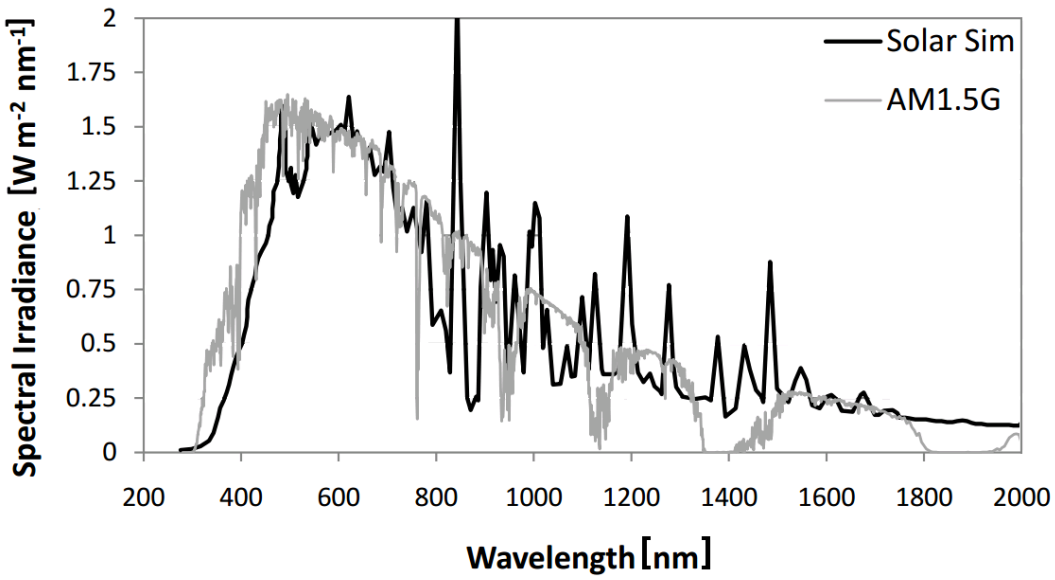

Fig. 12: Comparison of the Newport 150 W solar simulator spectrum with the ASTM G173-03 AM1.5 global spectrum at 100 mW/cm^2 [115].

For *JV* testing, the devices were mounted in a custom built holder at a distance such that the incident power density from the simulator was 100 mW/cm^2, calibrated with a Thorlabs D3MM thermal sensor. A variable bias was then sourced across the cells through a Keithley 2400 Source Measurement Unit (SMU) while current output was recorded.

A typical *JV* curve recorded in this way is sketched in Fig. 13 for measurements in the dark and under illumination, including the device parameters that can be directly determined from the graph as displayed. V_{OC} and J_{SC} are both determined from the curve recorded under illumination. V_{OC} is the voltage at which the built in bias is nullified by the applied bias so that no current flows, i.e. the voltage at zero current, J_{SC} is the current measured at zero external bias.

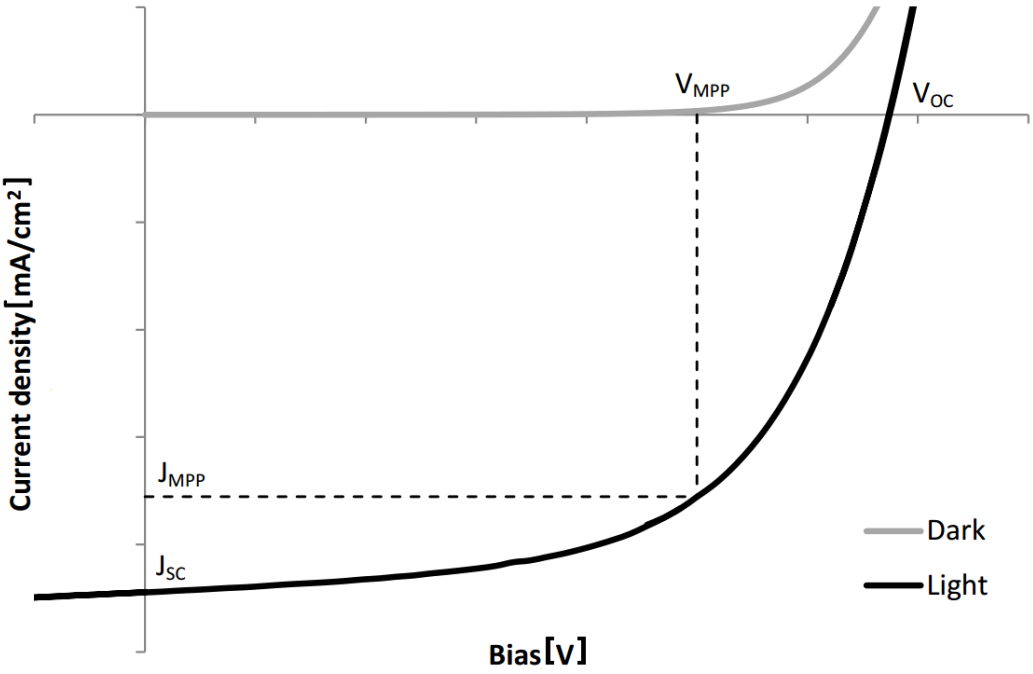

Fig. 13: JV curve of a typical solar cell [115].

The fill factor *FF* is determined using J_{MPP} and V_{MPP}, the current density and voltage at the maximum power point, and J_{SC} and V_{OC} in the following equation:

$$FF = \frac{J_{MPP}\ x\ V_{MPP}}{J_{SC}\ x\ V_{OC}}$$

PCE then results from:

$$PCE = \frac{J_{MPP}\ x\ A\ x\ V_{MPP}}{P_{IN}}$$

where *A* is the device area and P_{IN} is the incident light power density.

2.2.1. Determination of Parasitic Resistances

Series resistance R_S and shunt resistance R_{SH} have a significant impact on the fill factor and ultimately on the efficiency of a solar cell. R_S arises from the resistance of the materials used in the solar cell and from resistivity at the contacts, whereas R_{SH} stems from current leakage through the device e.g. at micro-shorts and around the edges of the device [14]. For a well-performing solar cell, R_S should be as small and R_{SH} as large as possible.

The diode equation including parasitic resistances is:

$$I = -I_{SC} + I_0 \left(e^{\frac{q\,(V+I\,R_S)}{kT}} - 1 \right) + \frac{V + I\,R_S}{R_{SH}}$$

with I and V being the measured current and voltage from the JV curve, I_0 the reverse saturation current, q the elementary charge and k the Boltzmann constant. For very large values of R_{SH} the second term can be neglected and the equation can be rearranged to:

$$\frac{dV}{dI} = -\frac{k_B\,T}{q} \left(\frac{1}{I_{SC} + I_O - I} \right) - R_S$$

At open circuit conditions, where $I=0$ and $V=V_{OC}$, this gives:

$$R_S = \frac{dV}{dI}\Big|_{V=V_{OC}} + \frac{k_B\,T}{q} \left(\frac{1}{I_{SC} + I_0} \right)$$

R_S can further be approximated, as the second term in this equation will be small compared to the series resistance:

$$R_S \approx \frac{dV}{dI}\Big|_{V=V_{OC}}$$

Analogous for R_{SH}, in the case of small R_S, so that terms containing R_S can be neglected we get:

$$\frac{dI}{dV} = -\frac{q}{k_B T} I_0 e^{\frac{q V}{k_B T}} + \frac{1}{R_{SH}}$$

And at short circuit conditions, where $V=0$ and $I=I_{SC}$:

$$\frac{1}{R_{SH}} = \frac{dI}{dV} - \frac{q I_0}{k_B T}$$

Since the second term is negligible compared to dI/dV we get:

$$R_{SH} \approx \frac{dV}{dI}\Big|_{V=0}$$

2.2.2. Determination of Dark Saturation Current

The dark diode equation is:

$$J = J_0 \left(e^{\frac{q V}{n k_B T}} - 1\right)$$

where n is the ideality factor. The dark saturation current J_0 can be determined by fitting the dark diode equation to the diode portion of the dark *JV* curve. Starting values for n and J_0 were 1 and $1*10^{-6}$, respectively. An example of such a fit is shown in Fig. 14.

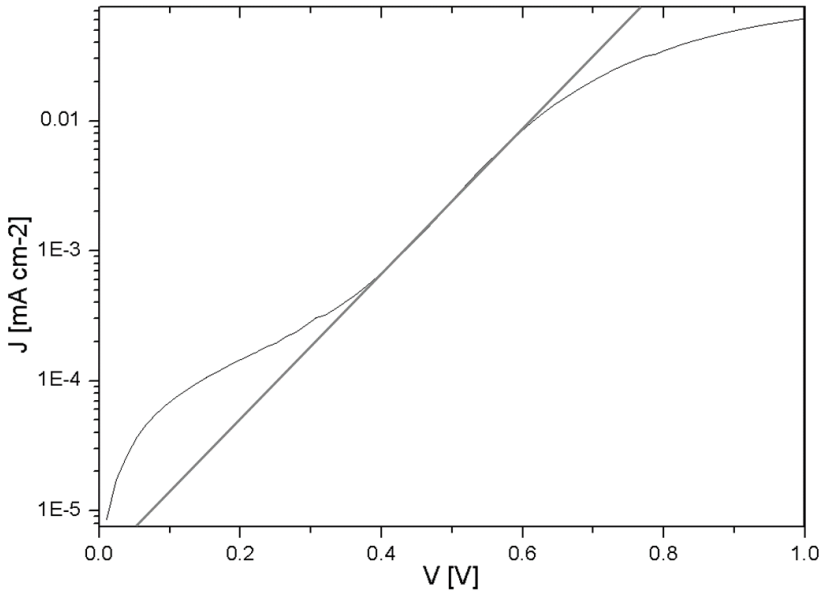

Fig. 14: Example dark IV curve in half log plot showing the diode equation fitted to it to determine J_0.

2.3. Hall Measurements

Hall Effect measurement is a standard technique used in the semiconductor industry to determine charge carrier type, conductivity, carrier density and mobility of semiconductors. An electron moving along an electric field perpendicular to an applied magnetic field experiences a magnetic force, the Lorentz force, perpendicular to both fields. A charge builds up on the surface of the sample and the measured Hall voltage allows a determination of carrier polarity and density, and with known resistivity, the carrier mobility. This is visualized for an n-type bar-

shaped sample in Fig. 15. Here, current flow *I* is from left to right, the magnetic field *B* points into the image plane and the Lorentz force *F* drives electrons towards the top of the sample, causing a surface charge and resulting transverse Hall voltage *V*.

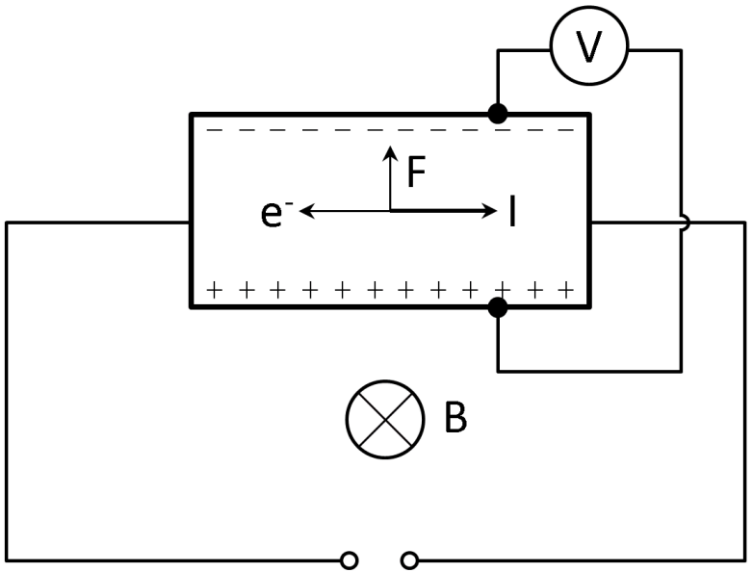

Fig. 15: Representative illustration of the forces causing the Hall Effect for a bar shaped n-type sample.

2.3.1. Experimental Setup

Samples used for Hall measurements were square thin films of minimum 500 nm thickness on glass slides with a lateral length of about 1 cm. The small sample size was chosen due to inhomogeneities in the stationarily sputtered samples over larger areas. Ohmic electric contacts were achieved through Cu wires attached to the four corners using silver paint. The contacts were numbered counter clockwise from one to four, starting in the top left corner.

The measurements were carried out in the field of Newport Instruments Electromagnet of 1 Tesla, currents in the range of 10^{-4} to 10^{-6} A were sourced through a Keithly 220 V Programmable current source and voltage was measured using an Agilent 34420 Nanovolt meter. All measurements were performed in the dark at room temperature.

Conventions for the measurement were:

I_{12}…….positive current between contacts 1 and 2, analogous for I_{23}, I_{34}, I_{41} etc.

V_{12}....voltage measured between contacts 1 and 2, i.e. V_1-V_2 at B=0, analogous for V_{23}, V_{34}, V_{41} etc.; for measurement in a magnetic field index P or N is added for positive and negative direction respectively

Requirements to minimize the source of errors:

- Diameter of the contacts (*D*) and sample thickness (*d*) must be smaller than the distance between the contacts (*L*). Errors are in the order of *D/L*.
- Contacts must be ohmic.
- Samples should be symmetrical.
- Power dissipation should not exceed 5 mW, set current such that $I < (200\ R)^{-0.5}$.

2.3.2. Calculations

Sheet resistance is determined using the van der Pauw method. Therefore current is sourced through different contacts to measure voltage and calculate resistance as follows, using the above mentioned conventions:

$R_{21,34} = \frac{V_{34}}{I_{21}}, \quad R_{12,43} = \frac{V_{43}}{I_{12}}$

$R_{32,41} = \frac{V_{41}}{I_{32}}, \quad R_{23,14} = \frac{V_{14}}{I_{23}}$

$R_{43,12} = \frac{V_{12}}{I_{43}}, \quad R_{34,21} = \frac{V_{21}}{I_{34}}$

$R_{14,23} = \frac{V_{23}}{I_{14}}, \quad R_{41,32} = \frac{V_{32}}{I_{41}}$

Internal consistency checks are performed through:

$R_{21,34} + R_{12,43} = R_{43,12} + R_{34,21}$ and

$R_{32,41} + R_{23,14} = R_{14,23} + R_{41,32}$

and only measurements where these statements are true within 5 % are considered valid results.

Sheet resistance R_S can then be calculated using the van der Pauw equation:

$e^{\frac{-\pi R_A}{R_S}} + e^{\frac{-\pi R_B}{R_S}} = 1$

where

$R_A = \frac{R_{21,34} + R_{12,43} + R_{43,12} + R_{34,21}}{4}$ and

$R_B = \frac{R_{32,41} + R_{23,14} + R_{14,23} + R_{41,32}}{4}$.

Hall measurements for the determination of carrier type, density and mobility are performed in a magnetic field such that currents are applied and voltages are measured in opposing corners of the sample, i.e. apply I_{13} and measure V_{24} for both positive and negative magnetic fields etc. The material is p-type if

$$V_H = (V_{24P} - V_{24N}) + (V_{42P} - V_{42N}) + (V_{13P} - V_{13N}) + (V_{31P} - V_{31N})$$

is positive and n-type if $\Sigma_{\Delta V}$ is negative.

Carrier density (for n- or p-type materials respectively) can then be determined through:

$$n = \frac{I\ B}{q\ |V_H| d}$$

with q being the elementary charge and d the sample thickness. Hall mobility follows with:

$$\mu = \frac{1}{q\ n\ d\ R_S}$$

2.4. Kelvin Probe Measurements

The Kelvin Probe Method is a non-destructive, non-contact method to measure work function of a solid [116]. The work function is defined as the minimum energy required to remove an electron from a solid, which means it describes the position of the Fermi Energy relative to the vacuum level.

2.4.1. Operating Principle

The Kelvin Probe consists of a head unit, which contains a voice coil driving system and an integral amplifier, suspended above the sample. The Kelvin Probe operates like a parallel plate capacitor, where the tip of the reference probe and the sample surface represent the two plates.

Fig. 16 shows the Kelvin Probe arrangement with its two control systems: the PC controls the digital oscillator, setting the voice coil frequency, the amplitude and the signal trigger; the data acquisition system sets the backing potential and acquires the probe signal.

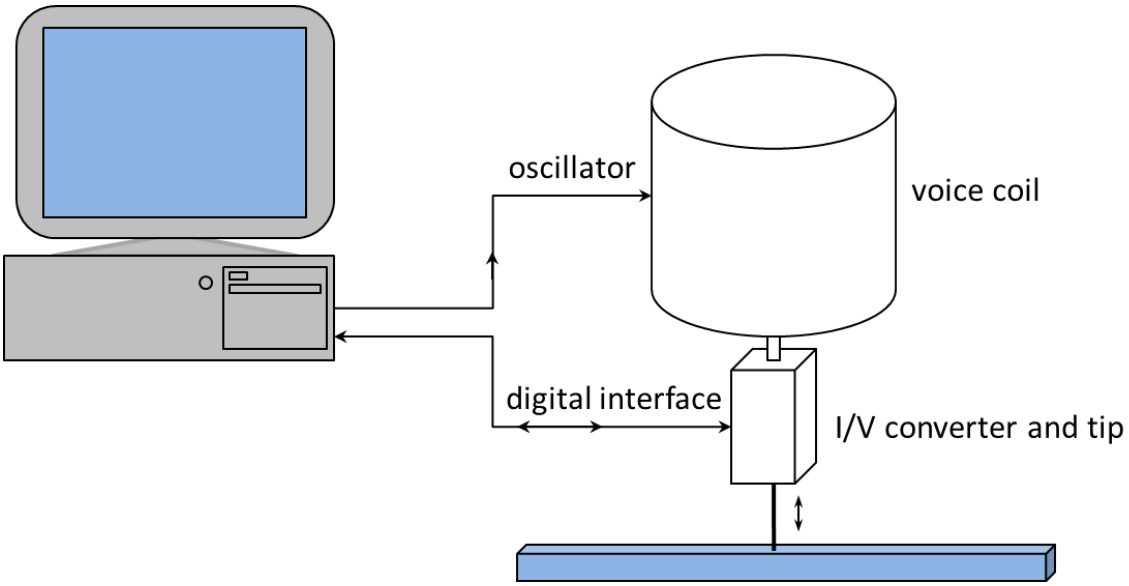

Fig. 16: KP system.

The signal that is measured is the contact potential difference between the reference tip and the sample. When contact is made between the two electrodes of the capacitor of different work function their Fermi levels equalise and the exchange of charge creates equal and opposite surface charges on the plates. The voltage forming over the capacitor is called the contact potential difference (CPD) and is measured by applying a backing potential V_b of direction and magnitude such that the surface charge disappears [117]. This mechanism is illustrated in Fig. 17.

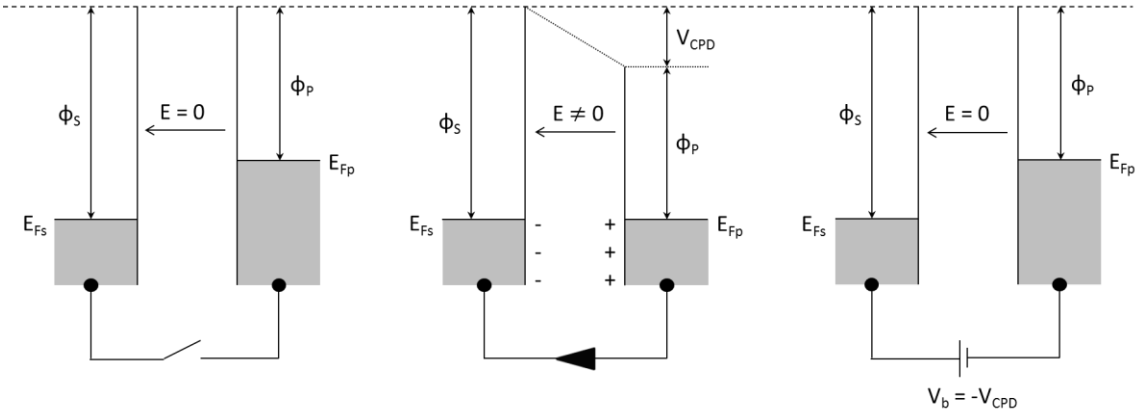

Fig. 17: Energy level diagrams of the sample and tip without contact, with external electrical contact and including the backing potential (left to right).

The capacitance results from the charge *Q* at the plates and the voltage V_C across the capacitor:

$$C = \frac{Q}{V_C}$$

By using a vibrating tip the distance between the capacitor plates is constantly varied so that with increasing distance the capacitance changes following the relationship:

$$C(t) = \frac{\varepsilon\ \varepsilon_r\ A}{d_0} = \frac{C_0}{1 + \beta\ \cos(\omega t)}$$

where *C(t)* is the time dependent capacitance, ε is the permittivity of air, *A* is the tip area and d_0 is the tip-sample separation. ε_r is assumed to be equal to 1 for measurements in air. β is the modulation index d_1/d_0, where d_1 is the amplitude of oscillation of the probe.

The current *I(t)* arising from the flow of charge between the plates with changing distance then results:

$$I(t) = \frac{dQ}{dt} = V_C \frac{dC}{dt}$$

Since the voltage V_C is the sum of the contact potential difference V_{CPD} and the backing potential V_b, the overall voltage equals zero when $V_b = - V_{CPD}$. At this point the output signal also equals zero and hence the work function difference between the tip and the sample is equal to the opposite potential required for a zero output signal [118].

In order to minimize error caused by noise and feedback depending on d_0 and d_1, the Off-Null method is used to calibrate the measurement. For this purpose the balance point is determined via linear extrapolation rather than nulling [119]. V_{ptp} versus V_b is hence plotted for a range of potentials and the linear graph is described with

$$V_{ptp} = m\, V_b + c$$

with *m* being the gradient and *c* the intersect with the y-axis. The contact potential difference V_{CPD} is hence equal to V_b when V_{ptp} is zero. For measurements, only two different values for the backing potential are used, +5 V and -5 V.

The gradient, *m*, obtained from this method depends on the mean spacing between the tip and the sample surface via a d_0^{-2} relationship and is hence used to set the distance and keep a constant spacing during measurements. A gradient of 400 was chosen for the measurements in this work as a higher gradient often resulted in contact between probe and sample and lower gradients for higher distances between tip and sample showed a larger measurement error.

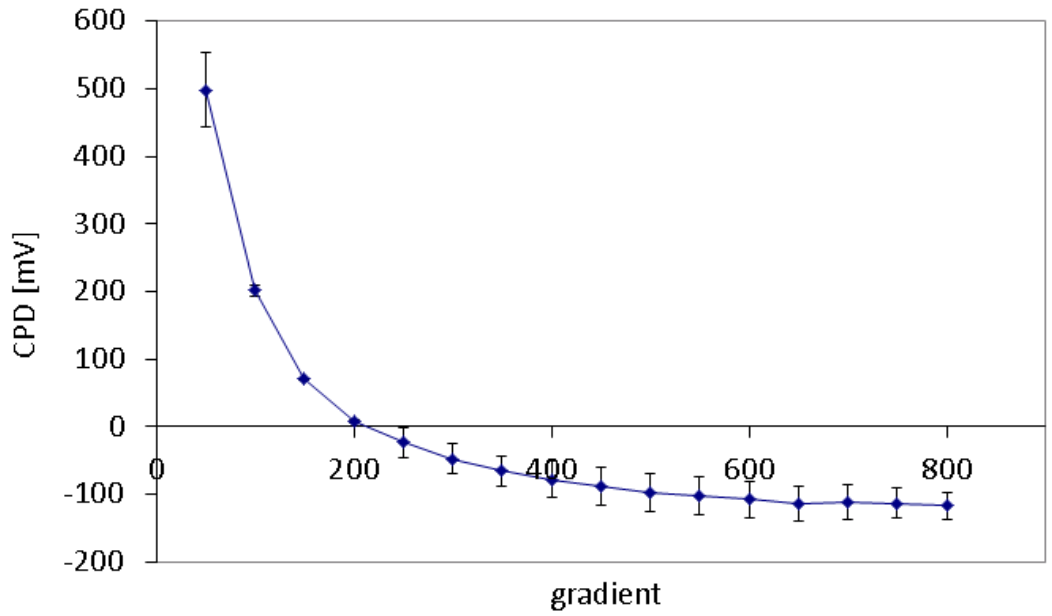

Fig. 18: CPD versus V_{ptp}-V_b gradient for the calibration of the probe-sample distance in Kelvin Probe measurements.

Conversion of the measured CPD values into work function (WF) values was achieved through the measurement of films of known work function and comparison with literature values. This method is taken as internally consistent and allows the comparison between different materials, however it should be noted that despite this, direct comparison with values obtained from different equipment and using different tips is still difficult. This is due to the fact that the measured contact potential difference depends vastly on the surface finish so that sample preparation plays a major role, and the work function of the metal tip depends on factors such as, for example, surface crystallographic orientation and lie in a range spanning about 0.3 eV for most materials [120]. Gold was chosen as probe material because of its stability in air. Its work function literature values vary between 4.8 and 5.1 eV [121].

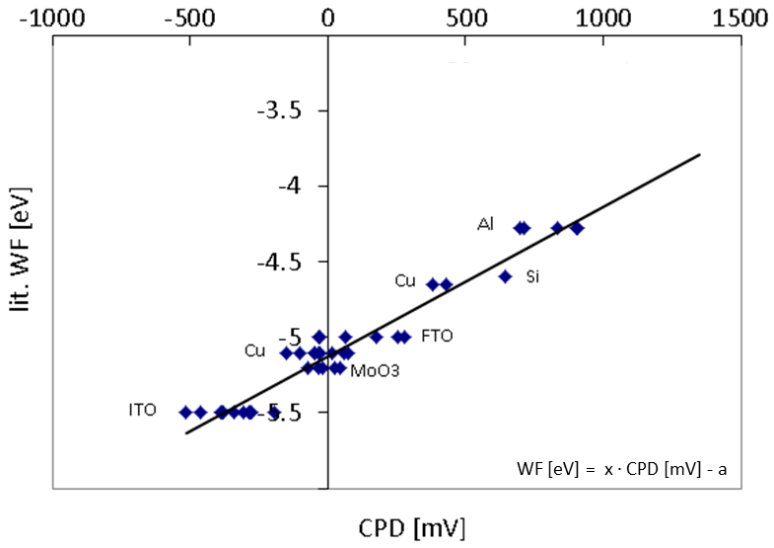

Fig. 19: Graph for the conversion of contact potential difference to work function.

2.4.2. Sample Preparation and Measurement

Kelvin Probe measurements on metal oxides are found in the literature [41, 45, 46], however when measuring low conductivity samples two requirements need to be fulfilled for accurate results:

- The sample needs to be able to dielectrically relax between changes of backing potential

- The sample capacity must be larger than the capacity of the counter electrode [122]

For this purpose, high resistivity films were measured on a conductive substrate, so that even if the above requirements are not met, i.e. charge movement within the film is not significant,

charge will still oscillate between the probe and the bottom interface between substrate and film, and the measurement is accurate independent of film conductivity [122].

Typically 30 measurements were taken in three different areas on each sample. As all films were either processed in air or at least exposed to air at some point during solar cell fabrication and are not sensitive to oxygen at room temperature Kelvin Probe measurements were performed in air both for practicality and to represent the applicability of the results to unencapsulated device structures.

2.5. UV-Vis Absorption Spectroscopy

UV-Vis spectra discussed in this work were measured on a Cary 5000 UV-visible-NIR spectrometer. The beam is produced by a tungsten halogen visible source with quartz window and a deuterium arc UV source, run through a monochromator and then split so that one beam can pass through the sample while the second beam is lead through a reference. The difference measured by the silicon photodiode detectors is the absorption of the investigated sample depending on wavelength.

2.5.1. Sample Preparation

For absorption measurements thin films were deposited on glass slides. A pristine glass slide was used as a reference.

2.5.2. Band Gap Determination

Optical band gaps were determined using a Tauc plot. In a Tauc plot $(\alpha h\upsilon)^r$ is plotted versus $h\upsilon$, with *r* being ½ for indirect and 2 for direct transitions [123]. Extrapolating the linear region of the curve to the abscissa gives the value of the optical band gap. An example is given in Fig. 20.

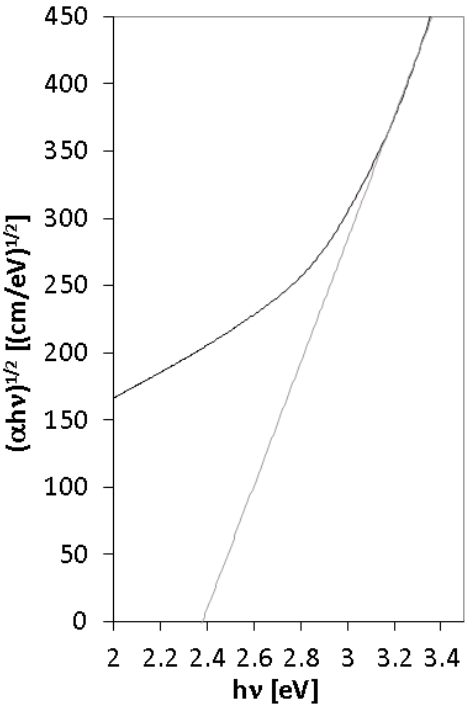

Fig. 20: Tauc plot of absorption data.

2.6. XRD

XRD patterns were recorded on a Philips PW1820 system with a PW1727 X-ray generator using Cu Kα radiation (λ=1.5418 Å). For phase matching the recorded data was compared to patterns on the crystallography.net database. In thin films it can be expected that the spread of crystal orientations is not random, but that some preferential grain orientations may easily form so

that there will be deviations in peak intensity and broadening compared to literature data of bulk measurements.

Thin films with thicknesses of at least 500 nm were deposited on glass slides and measured between 10 and 70° 2θ.

2.6.1. Grain Size Determination

The phenomenon of peak broadening with decreasing particle size below 1 μm was used to determine grain size following the Scherrer equation [124, 125]:

$$\tau = \frac{K\,\lambda}{\beta\,\cos\theta}$$

where τ is the mean grain size, K is a dimensionless shape factor, λ is the X-ray wavelength, β is the full width at half maximum (FWHM) and θ is the Bragg angle. K depends on the shape of the crystals and was taken to be 0.89 by Scherrer [126] and 1.11 by Patterson [127] for spherical particles of cubic structure. Birkes *et al.* [128] use an approximate value of 1 as a compromise for particles that are neither spherical nor cubic, but of cubic structure. In this work K was also assumed to have the value of 1.

Average grain size values were determined where several orientations of one phase were present.

2.7. SEM

Scanning electron microscopy (SEM) images were obtained on a JEOL JSM-840F at an accelerating voltage of 5 kV. Samples were prepared by attaching the substrates with the thin lead oxide films to metal stubs and coating it with 4 nm of platinum.

3. Evaporation and Thermal Oxidation of Lead Thin Films

3.1. Introduction

A simple way to make lead oxide films is to thermally evaporate lead and post anneal in air. Thermal oxidation of metallic lead has a very distinct colour change from metallic silver to yellow. Distinct visible oxidation at atmospheric pressure proceeds slowly at 270°C, while abrupt oxidation takes place at temperatures above 280°C. Oxidation is observed to start in one corner of the sample and then runs across the film within seconds. The oxidised films are yellow, indicating orthorhombic PbO. Below 270°C no significant oxidation is observed after 15 hours. Higher temperatures were not possible due to degradation in properties of the underlying ITO (see section 2.1.1.). This chapter reports a combination of crystallography, microscopy and optoelectronic characterisation techniques to understand the chemical and phase transformation dynamics of the oxidation process which influence the optoelectronic properties.

3.2. Microstructure

Microstructural investigations were carried out using XRD and SEM analysis to understand the formation and nature of different metal and oxide phases under different anneal conditions. A binary phase diagram is displayed in Fig. 7 showing the existence ranges of different phases with changing composition. However, the diagram shows the equilibrium phases for bulk material and does not take into account any thin film effects and the influence of the substrate, and hence does not provide much information for thin films oxidized for relatively short durations.

3.2.1. XRD

XRD patterns were recorded for thin films of lead after oxidation heat treatment in air at 270°C at different times. Fig. 21 shows the evolution of XRD patterns for 300nm thin films of metallic lead at various times over a 60 hour period.

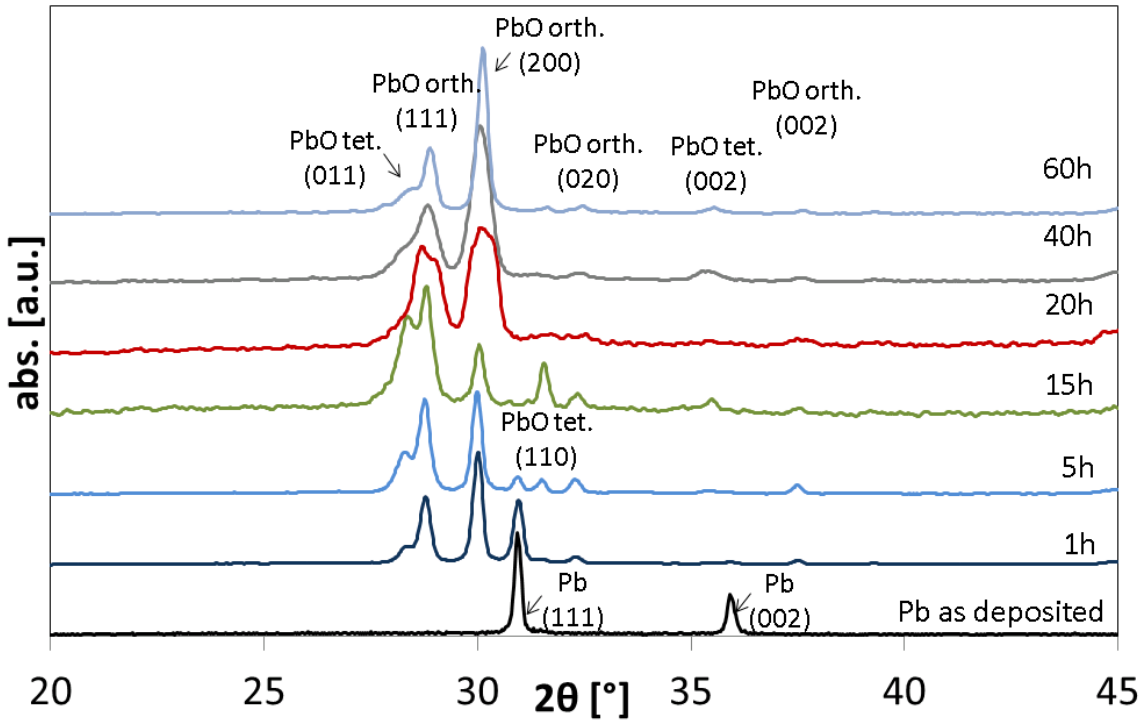

Fig. 21: XRD data for Pb films as deposited and after annealing at 270°C for 5h, 15h, 40h and 60h.

As-deposited, the lead film is crystalline with distinct peaks from the (111), (002) and (022) planes which indicate a grain size of approximately 49 nm in all orientations. After 1h at 270°C the (111) and (022) decrease in intensity while the (002) peak disappears completely, replaced by an orthorhombic lead oxide (PbO_{orth}) phase as indicated by strong (200) and (111) peaks and weak (002) and (020) peaks. Some tetragonal lead oxide (PbO_{tet}) is also present represented by a weak peak corresponding to the (011) plane.

There is very little work reported in the literature on thin film lead oxidation at these thicknesses. Most literature on the thermal oxidation of lead reports on film thicknesses greater than 10μm oxidised at higher temperatures [79, 129, 130]. There is some work on

monolayers of lead as well: Anderson *et al.* [131] reported the formation of purely orthorhombic lead oxide upon oxidising thermally evaporated thin films of lead at temperatures between 100°C and 275°C. After 5 h of heat treatment at 270°C oxidation has progressed further, showing an increasing content of tetragonal phase. The PbO_{orth} (111) peak gains intensity while the (200), (100) and (020) peaks stay roughly the same. The PbO_{tet} (011) peak increases in intensity and the (110) peak appears in the pattern, while the intensity of the only remaining Pb (111) peak decreases further.

After 15 h the sample is fully oxidised and no Pb peaks are observed. All the PbO_{orth} peaks lose intensity whereas the (200) peak shows the most significant loss, and the PbO_{tet} (011) and (110) peaks increase in strength. This shows an increase in PbO_{tet} content for intermediate oxidation times.

After 20 h the PbO_{tet} (011) decreases drastically and cannot be separated from the broad PbO_{orth} (111) peak. Following 40 h annealing the PbO_{tet} peaks do not show much change whereas the PbO_{orth} peaks become sharper. This trend continues and after 60 h the PbO_{tet} phase has almost disappeared with only a small residual (011) peak, and the sample predominantly consists of PbO_{orth}, showing (200), (111) and (100) peaks.

Anderson and Tare [131] describe the oxidation process as follows: Oxidation of Pb occurs through the adsorption of oxygen at free adsorption sites on the surface of the film, possibly located above a surface cation, with the oxygen taking up an electron. This is followed by the regeneration of the adsorption site through the combination of the adsorbed oxygen with an anion vacancy and an electron. The oxygen has now become an anion at the oxide-oxygen interface, and vacated the surface adsorption site that allows further oxidation. The

regeneration of anion vacancies occurs at the metal-oxide interface, through the combination of a lead atom and an oxygen anion, generating two free electrons and an anion vacancy.

For the case of thin films the oxidation process is complex, there are a number of competing processes occurring at the surface, bulk and substrate interface:

1. **Surface**

At the surface of the Pb film orthorhombic PbO is preferentially formed. Light *et al.* and Eldridge *et al.* [132, 133] report the formation of the high temperature orthorhombic oxide below its predicted transition temperature upon oxidation of thin films of lead and explain these findings through favourable misfit relationships between Pb and the orthorhombic oxide phase. Comparable to the findings in this work, they observe PbO_{orth} with a strongly preferred (001) orientation and explain that PbO_{orth} (001) grains are stabilized growing on a predominantly (111) Pb film, with the <001> PbO_{orth} direction parallel to the Pb <110> direction in the predominant (111) Pb planes. With these close packed directions of both phases parallel to each other the misfit between the Pb <110> direction and the PbO_{orth} <001> direction is estimated to be only about 3.6 %. The enthalpy of transformation between PbO_{tet} and PbO_{orth} of 57 cal/mol (238 J/mol) is very small, so that this misfit relationship is enough to stabilize the orthorhombic phase and allows for the formation of orthorhombic PbO below its bulk transition temperature.

Similarly, Baleva *et al.* [134] provide a theoretical analysis of this phenomenon and calculate the nucleation rate of PbO_{orth} and PbO_{tet} in films grown by pulsed laser deposition, finding a higher nucleation rate for polycrystalline PbO_{orth} than for PbO_{tet}. This is again explained with lower interfacial free energies as a result of a lower free energy of formation for nuclei of critical size for the PbO_{orth} (100) direction on (111) Pb. In accordance with [135] they conclude that pure PbO_{tet} films cannot be grown on Pb, but PbO_{tet} can only be obtained in a mixed PbO_{orth} - PbO_{tet} film.

2. **Bulk**

As oxidation progresses after the initial formation of an orthorhombic film on the surface, tetragonal PbO forms in the centre of the film as soon as oxygen diffuses into the material. This is explained by its smaller heat of formation and the lack of epitaxial forces in the bulk of the material. Wiechert *et al.* [135] also report more PbO_{tet} than PbO_{orth} in the bulk material of evaporated PbO films. However, for thinner films [134] the overall film composition remains predominantly PbO_{orth} for film thickness in the range of 500 nm, similar to the films in this work. In the topotaxic transformation of Pb to PbO_{tet}, (110) PbO_{tet} planes grow parallel to the (100) planes of Pb [136]. This could explain the disappearance of the (002) Pb peak with the emergence of the (011) PbO_{tet} peak at oxidation onset upon heating in air.

3. **Substrate interface**

Since the films in this work are oxidised post-deposition the influence of the substrate on phase formation will be less pronounced than in evaporated oxides. For thermal evaporation of PbO films however it was found by both Tompsett *et al.* [137] and Wiechert *et al.* [135] that an orthorhombic layer always forms on the glass substrate. The formation of tetragonal PbO is negligible at the initial stages of deposition. Similar to the formation of orthorhombic PbO on the surface of the Pb film, this phenomenon can be explained through orientation relationships between the film and the substrate.

Since the difference in enthalpy for the two phases is very small, thermodynamically the two oxide phases behave practically the same. The kinetic term of nucleation however correlates to the mismatch of the thermal expansion coefficients of the lattice constants between the substrate and the oxide phase as the energy for self-diffusion increases with increasing mismatch, thereby constraining epitaxy [134]. The linear thermal expansion coefficient for PbO_{orth} and PbO_{tet} are $15.9*10^{-6}$ K^{-1} and $25.9*10^{-6}$ K^{-1} respectively, whereas for glass it is roughly $1*10^{-6}$ K^{-1}, so that the mismatch between the oxide and the underlying glass substrate is smaller for orthorhombic PbO [134] explaining the higher nucleation rate for the orthorhombic phase than for the tetragonal phase. Orthorhombic seeding layers that reach thicknesses of up to 2 µm are reported for thermally evaporated PbO for overall films of 100 µm thickness [135] and 200 nm for 1 µm thick films [137]. The thickness of this seeding layer depends heavily on the processing method and conditions [134], for thermally evaporated films a higher deposition rate results in a thicker seeding layer [137]. Since the oxide films in the present work grow from surface to substrate this effect can only come into play at the final stages of Pb oxidation.

In summary, these three effects all contribute to the oxidation process at different time-scales. By 15 h the oxidation is complete and the stoichiometry is stable. However the crystal structure is continually changing due to the thermal energy supplied through the experiment. Since the difference in heat of formation between the tetragonal and orthorhombic phases is minimal, the percentage of PbO_{orth} in the film increases at the expense of PbO_{tet} [109].

To understand how this transition happens, the different crystal structures are examined.

The structure of the orthorhombic and tetragonal PbO phases are quite similar with clearly defined layer structures parallel to the (001) plane. Oxygen atoms are sandwiched between Pb atoms, each situated at the apex of an O_4 pyramid, and each Pb is four-coordinated surrounded by four O and *vice versa* [136, 138-140]. Upon oxidation of Pb, as oxygen is incorporated into the Pb lattice, the Pb tetrahedra become distorted and the Pb atoms are no longer in a close packed configuration. In PbO_{tet}, the atoms are aligned in zig-zag chains, which align in a stacked array at 90° rotation to form repeating layers of Pb-O-Pb as visualized in Fig. 22. In the PbO_{orth} phase chains repeating a distorted ABCD structure are formed and aligned in an antiparallel manner, resulting in two oxygen layers alternating with two lead layers [89, 140].

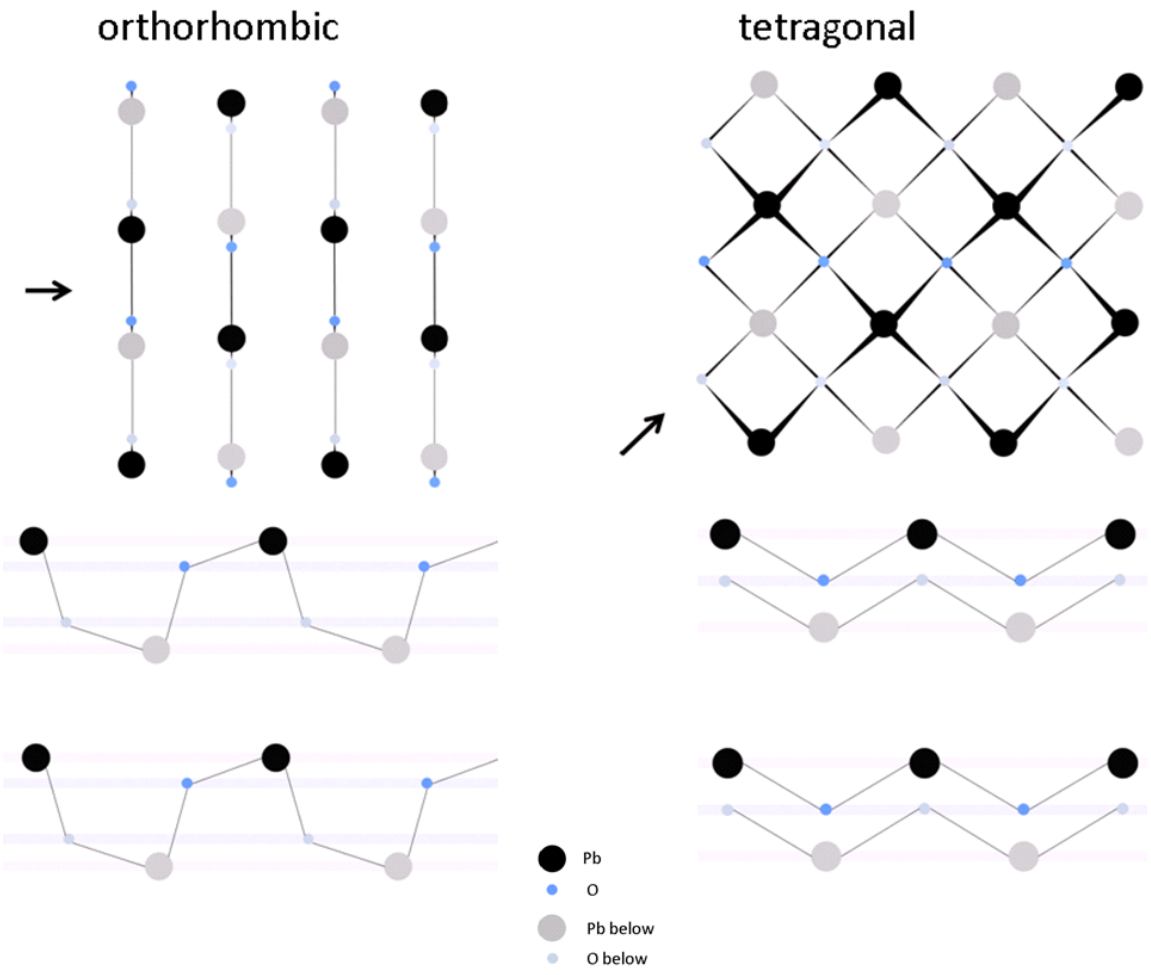

Fig. 22: Top view (top) and side view (bottom) of the structures of orthorhombic and tetragonal PbO. The arrows in the top view indicate the viewing direction for the side view sketches. Large black circles represent Pb, while small blue circles represent O. Grey and light blue circles stand for atoms one layer below the black and darker blue ones respectively in the top view image (in tetragonal PbO all oxygen atoms are situated in one plane, the light and dark blue colours were kept to better illustrate the transformation between the two phases. For better understanding, the same colours are also maintained in the side view sketches below). In the tetragonal side view image (bottom right), the lower of the two respective parallel zig-zag chains lies a unit cell "behind" the top chain within the image plane.

In PbO_{tet} all Pb-O bonds are of equal length, whereas in the distorted ABCD chains in PbO_{orth} two short and two long bonds exist between Pb and O [139]. In both phases the different layers are held together through interlayer bonds that are formed by lone pairs, connecting the layers through van der Waals forces. The lone pairs pack more tightly in tetragonal PbO, resulting in a shorter interlayer distance and hence higher density in the tetragonal structure [89, 140].

The side view sketches (bottom of Fig. 22) illustrate that orthorhombic PbO is built up in a sequence of layers of Pb-O-O-Pb Pb-O-O-Pb whereas in tetragonal PbO the oxygen atoms are situated in one plane resulting in the sequence Pb-O-Pb Pb-O-Pb [89].

Fig. 23 shows a simplified sketch of the tetragonal – orthorhombic transformation of PbO, showing the orientation relationship between the two phases and the movement of the oxygens during the transformation.

The transformation from orthorhombic to tetragonal PbO, opposite of what was observed in this work, was analysed and explained by Soderquist *et al.* [140]. The two lattices of the different phases align with the layers $(001)_{tet} \parallel (001)_{orth}$ and the directions $[110]_{tet} \parallel [100]_{orth}$, as visualized in Fig. 23. This way the lead packing can be conserved during the transformation. The, smaller, oxygen atoms are moved about 0.7 Å upwards and downwards along the $[001]_{orth}$, whereas the lead atoms are shifted about 0.47 Å [140]. Soderquist *et al.* don't observe any sharply defined transformation boundaries and suggest that the atoms diffuse to their new positions at random.

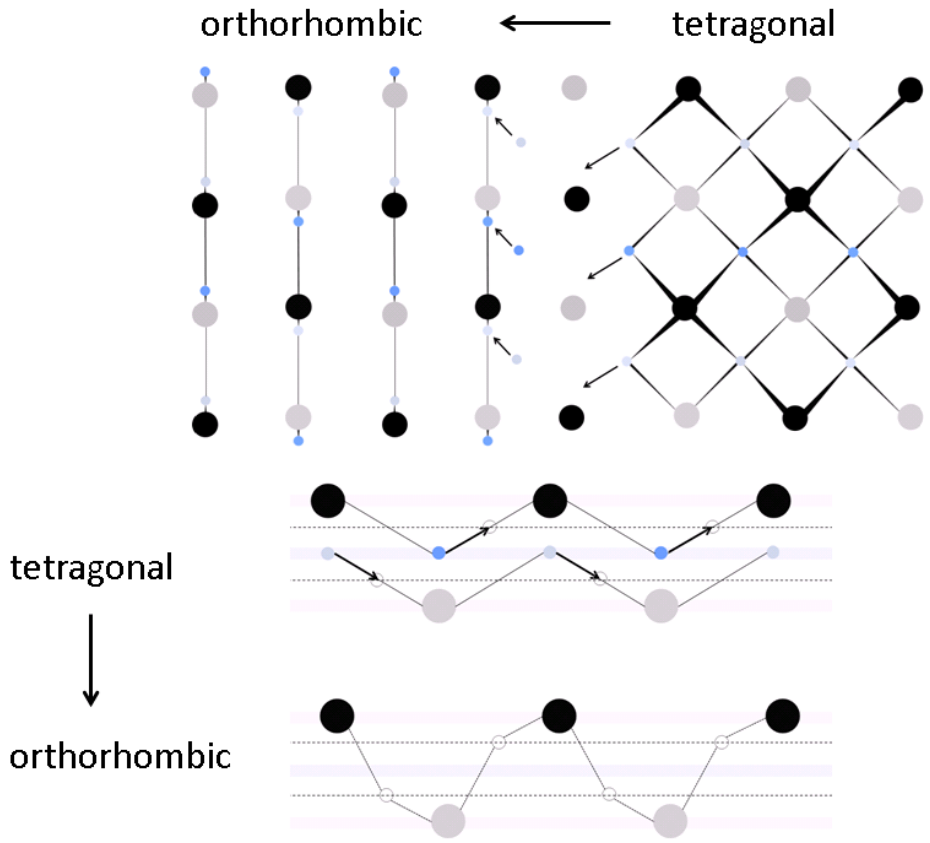

Fig. 23: Sketch of the transformation from tetragonal to orthorhombic PbO, showing the movement of the oxygens during the transformation.

In this suggested process of transformation the $(011)_{tet}$ planes are close to parallel to the $(111)_{orth}$ planes, so that $(011)_{tet}$ planes will result in $(111)_{orth}$ planes. A competition between these two orientations is observed in XRD (Fig. 21), where the PbO_{tet} (011) peak grows at the expense of the PbO_{orth} (111) peak at intermediate anneal times at 15 and 20 hours, with the reversed process occurring at long anneal times over 20 hours. This reversal is attributed to the fact that the heat of formation of the two phases is very similar and the continued heating

supplies enough energy for transformation to the orthorhombic phase in thin films, where PbO_{orth} is stabilised by orientation relationships with the substrate. A similar transformation has been observed by Venkataraj *et al.* [109].

3.2.2. Grain Size from XRD

Grain sizes can be ascertained from the peak widths of the XRD pattern (Fig. 21) and further confirm the findings about the preferential growth of the tetragonal and orthorhombic phases. The PbO_{orth} (020) peak broadens significantly with increasing heating time up to 20 hours, indicating a decrease in grain size. Between 40 and 60 h the measured peaks become significantly sharper, indicating general grain growth after long heat treatments.

A closer examination of grain sizes in Fig. 24 reveals a trend in accordance with the disappearance of the PbO_{tet} phase and the formation of new PbO_{orth} grains throughout the heat treatment.

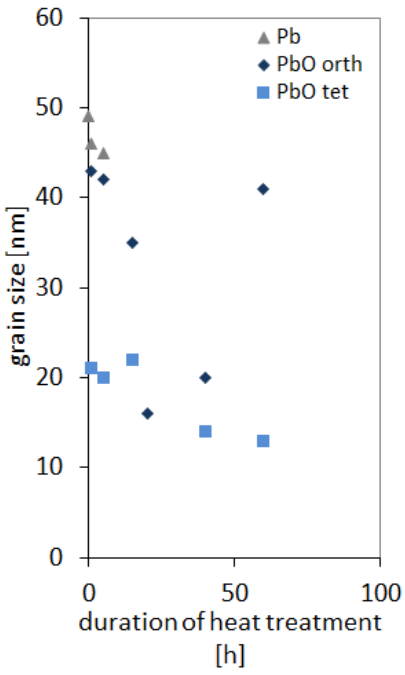

Fig. 24: Grain size of lead and lead oxides as a function of duration of oxidation heat treatment at 270°C.

With increasing duration of the heat treatment and as oxidation progresses, Pb grain sizes remain at a roughly constant size until they disappear after 5 h. This suggests that in the early stages of oxidation the grains that do not have an orientation relation with the underlying substrate oxidise first.

PbO_{orth} and PbO_{tet} grain sizes are 43 nm and 21 nm respectively after 1 h of oxidation, and both decrease after 5 h, indicating the nucleation of new oxide grains in both phases as the concentration of Pb in the sample decreases with the incorporation of oxygen into the lattice progresses. After 15 h the PbO_{tet} grains are slightly bigger while the size of the PbO_{orth} grains is

still decreasing, suggesting further nucleation of orthorhombic grains, while PbO_{tet} grains grow in the bulk of the film, consuming the remaining Pb.

After 20 h PbO_{tet} grain sizes cannot be measured as the small (011) peak cannot be separated from the PbO_{orth} (111) peak. The orthorhombic grains decrease to a minimum value of 16 nm as nucleation of new grains continues. After that, at 40 h and 60 h tetragonal grains decrease in size, with PbO_{tet} peaks almost disappearing from the pattern, and orthorhombic grains increase, indicating the growth of PbO_{orth} grains at the expense of PbO_{tet}.

The thickness of the films increases from 300 nm in the as-deposited sample to a total of roughly 500 nm after 60 h at 270°C, as measured via DEKTAK. The increase in thickness with increasing oxidation time can be attributed to the continuous incorporation of oxygen into the lattice as the oxidation progresses. The oxygen atoms locate at interstitial sites in the lead lattice, pushing the Pb atoms apart, thereby increasing the volume of the film. PbO_{orth} is less densely packed than PbO_{tet} with wider interlayer distances [140] and hence the film thickness keeps increasing slightly with the transformation of PbO_{tet} to PbO_{orth}, even after the film is fully oxidized, although after 15 h no substantial further increase in thickness can be observed.

3.2.3. SEM

SEM top view images show a rough microstructure with features in the order of roughly 50 to 500 nm that show no apparent change for heat treatments at magnifications up to 30 000x (Fig. 25).

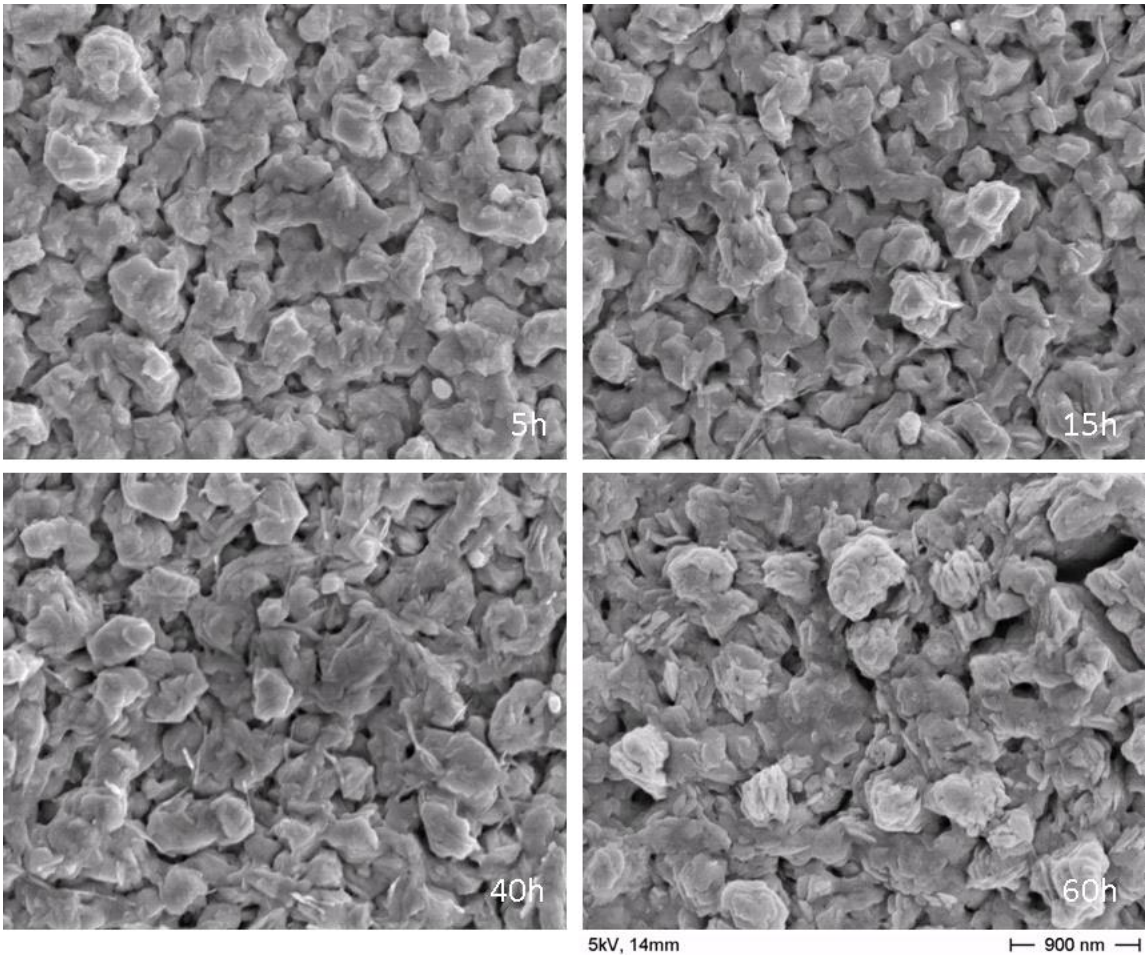

Fig. 25: Top view SEM micrographs for lead oxide films after different durations of heat treatments at 270°C.

3.3. Optical Properties

The changing compositions determined by XRD are also reflected in absorption data. Actual band gaps were found to be indirect from absorption spectroscopy using a Tauc plot and lie between 2.15 and 2.40 eV (Fig. 26). These values lie between the literature band gap values for PbO_{orth} and PbO_{tet} and could be expected for a multiphase material. The band gap of PbO_{tet} is reported between 1.9 and 2 eV throughout the literature, while values ranging from 2.5 eV to 2.8 eV can be found for pure PbO_{orth} [109, 130, 141]

The values found in this work correspond well with phase compositions found in XRD. After 5 h a considerable proportion of the film is oxidized which allows for band gap determination through absorption measurements. At this point the film consists of a mixture of orthorhombic and tetragonal PbO and the band gap is found to lie just below 2.3 eV, which is right in the middle between reported values for the two PbO phases. With increasing formation of tetragonal PbO at 15 and 20 h the band gap decreases, approaching 2.15 eV, close to the expected value for a tetragonal film. For longer heat treatments that see films undergo a transformation from tetragonal to orthorhombic PbO the band gap increases again and is found to be close to 2.35 eV, now closer to the literature band gap value for PbO_{orth}.

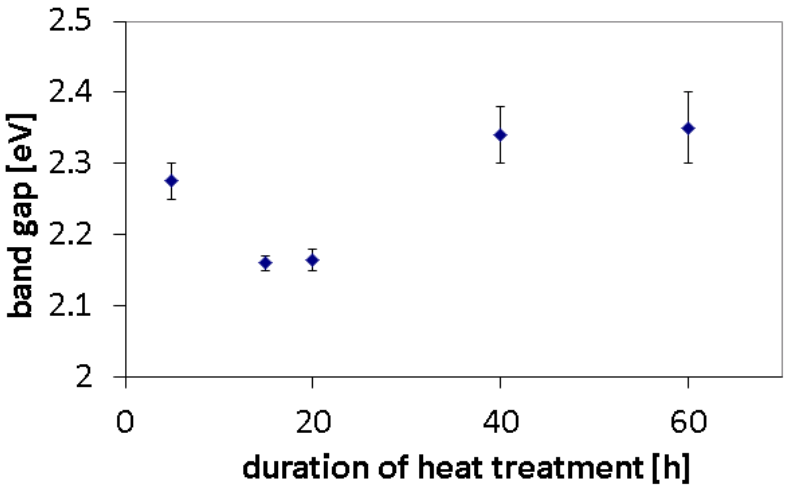

Fig. 26: Band gaps of lead oxide films depending on duration of the heat treatment.

3.4. Electronic Properties

Unfortunately lead oxide films produced via this method are highly resistive and thin films showed resistances across the surface in the order of GΩ so accurate measurements of resistivity, charge carrier density, mobility and carrier type could not be carried out through either four point probe, Hall measurements or Seebeck effect measurements. Schottmiller [130] reported difficulties making four point probe measurements on vapour deposited PbO films, PbO_{tet} was ~10^{11} Ω cm and PbO_{orth} ~10^{13} Ω cm which is beyond the measurement capabilities of our equipment. Most reliable methods for high resistivity materials in the

literature utilize a sandwich type electrode configuration, mostly using ITO and Ag as electrode material, to minimize length of the conductive pathway [130, 131].

From our observation and related literature, the following assumptions can be made about conductivity and charge carrier type of these films. Firstly, conductivity is highly dependent on oxygen pressure during production and processing of lead oxide films [129-131, 141-144]. Generally, films deposited at very low pressures or vacuum are n-type [130, 131, 141, 142, 144] and a transition to p-type conduction has been observed upon heat treatments at higher oxygen partial pressures [130, 131, 142, 144]. The literature broadly agrees that n-type PbO is oxygen deficient, and conductivity decreases for heat treatments with increasing oxygen partial pressure. This is attributed to the "filling up" and hence decreasing number of oxygen vacancies that are responsible for conductivity in n-type PbO [129, 130, 141-144]. Ma, Eldridge, Heyne and Schottmiller [130, 132, 142-144] all report a point of minimum conductivity, after which conductivity increases again with increasing oxygen partial pressure. This point of minimum conductivity and minimum number of charge carriers corresponds to the transition point from n-type to p-type conduction. Schottmiller also explains the change from n- to p-type with changing oxygen content, with oxygen vacancies or interstitial Pb in n-type material and Pb vacancies or excess oxygen incorporated in the lattice in p-type material. In agreement with this theory Eldridge defines a range of possible deviations from perfect stoichiometry with $Pb_{1.002}O$ for Pb rich n-type material and $PbO_{1.0012}$ for oxygen rich p-type material. One experimental method that does elucidate part of this transition is Kelvin Probe.

3.4.1. Work Function

From Kelvin Probe an increase in work function (Φ) can be observed with the duration of the heat treatment as shown in Fig. 27.

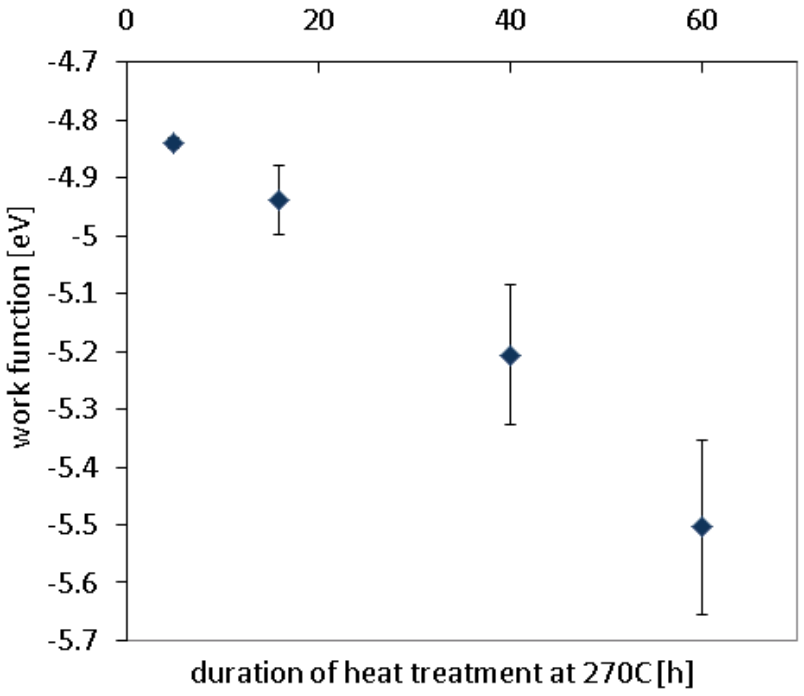

Fig. 27: Work function depending on the duration of the heat treatment of PbO films.

The analysed films are highly resistive and the maximum resistivity can be expected for the stoichiometric phase with the Fermi level in the middle of the band gap. Deviation from stoichiometric PbO introduces charge carriers into the material and hence changes its work function. Excess oxygen means that for every O two balancing positive charges must be present

in the material to achieve overall charge neutrality, increasing the number of holes in the material, hence lowering the Fermi level and making it p-type. For excess lead the opposite is true and the material will show a decreased work function, i.e. a higher level of the Fermi energy, and be n-type. This correlation between charge carrier density and work function has been observed in a number of simple and complex, doped and undoped oxide systems [145, 146].

3.4.2. Is it p-Type or n-Type?

If the annealed material were n-type, increasing the oxygen content would suggest a decrease in charge carriers, however if it were a p-type material, an increase in charge carriers would result. Similarly the annealing could also induce a transition from n- to p-type in this region. Schottmiller [130] observed this effect for evaporated PbO samples annealed at 300°C at various pressures, and attributed it to the incorporation of oxygen into the PbO lattice. Generally, the transition temperature from n- to p-type decreases with increasing oxygen pressure, as at higher pressures oxygen is more easily incorporated into the material and more oxygen uptake will happen at lower temperatures, hence filling up oxygen vacancies more efficiently. Schottmiller's results support the theory that the material discussed in this work is p-type, after long heat treatments at 270°C at ambient pressure. Yong *et al.* [147] determined the positions of the band edges of orthorhombic PbO at -4.02 eV and -6.82 eV. Assuming similar values for the material produced in this work, which is predominantly orthorhombic,

these values also suggest a transition from n-type to p-type during the oxidation heat treatment of the thin films. This assumption will be further discussed with regards to junctions formed between PbO and materials with known properties in chapter 5.

With increasing duration of the heat treatment the error bar for the measured work function value widens and the work function values become less reproducible. Generally semiconductors are very sensitive to foreign elements and charge carrier density and conductivity depend heavily on doping. Small local changes in oxygen content will hence have a considerable net impact on the carrier concentration and therefore work function of PbO [148]. In this work, the deviation in work function after long heat treatments can be attributed to small deviations in processing parameters such as material purity, temperature homogeneity of the hotplate, temperature of the surroundings, ambient humidity or even changes in air composition due to other on-going experiments that can all have an effect on the adsorption of oxygen and hence incorporation of oxygen anions or impurities into the PbO lattice.

3.5. Summary

This chapter has shown that by thermally evaporating a thin film of metallic lead and post-deposition annealing in air, mixed tetragonal and orthorhombic lead oxide thin films can be produced with composition dependant on anneal time. The mixed phase system inherently

leads to poor electronic properties arising from a smearing of the electronic structure. In a bid to improve the material properties the next chapter examines sputter coating as a route to producing homogeneous lead oxide thin films with a range of stoichiometries and hence band gaps.

4. Sputter Deposition of Thin Films of Lead Oxide

In a bid to produce thin films of lead oxide with more favourable electronic properties it was decided to use reactive magnetron sputtering at different oxygen flow rates. This method was used by Venkataraj *et al.* [109] with success to produce films with different stoichiometries and band gaps which suggested they would be suitable for photovoltaic devices.

In sputter coating, film deposition is dependent on cathode potential, atmosphere and substrate temperature. To keep variables to a manageable amount current and temperature were held constant. As in chapter 3, crystallography, microscopy and optoelectronic characterisation techniques are used to probe the chemical and phase transformation dynamics of the reactive deposition process and post deposition anneal.

4.1. Hysteresis and Deposition Rate

It is generally observed during reactive sputtering that, due to changes in the target surface chemistry, the cathode potential changes as a function of oxygen flow rate (Fig. 28). This was monitored for the reactive sputtering of lead by incrementally changing the proportion of oxygen and argon in the plasma (from pure argon, through steps of 2 sccm of oxygen to pure oxygen), and measuring the target potential. The overall gas flow of Ar and O_2 was held constant at 40 sccm, the current was set to 0.85 A and the potential was measured once the process had reached equilibrium and the voltage settled into a stable level after 5 minutes. Substrates were unheated and substrate temperatures were measured during deposition using a thermocouple and found to slightly vary between 100°C and 125°C.

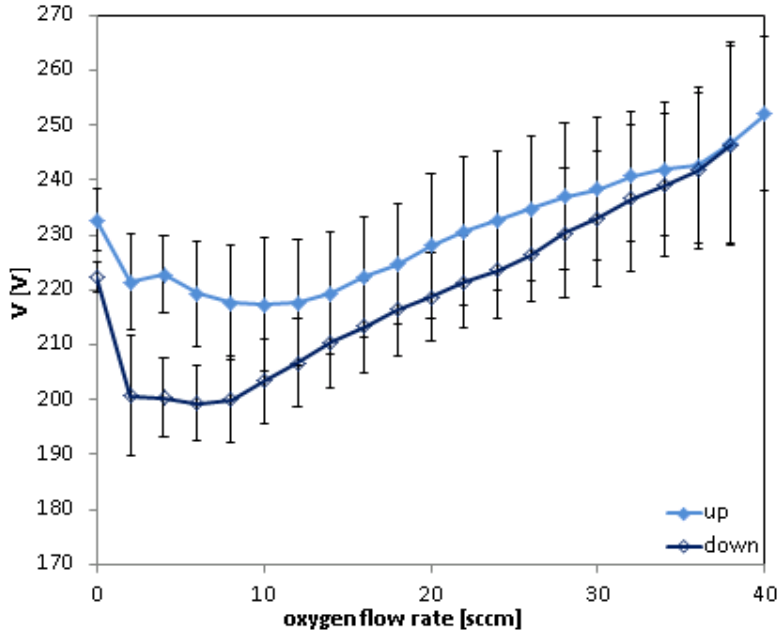

Fig. 28: Cathode potential as a function of oxygen flow rate at a constant absolute Ar+O_2 gas flow of 40 sccm. Typical of a hysteresis curve, the values for the potential as the flow rate was being increased at each step (pale blue line) are different than those as the flow rate was being decreased at each step (dark blue line). Error bars represent the spread of the values of 5 runs.

A sharp initial voltage drop is observed between 0 and 5 sccm while increasing the oxygen flow to the chamber. This initial decrease can be explained by the onset of target poisoning, the oxidation of the target surface with increasing oxygen content in the sputtering chamber, which increases the emission of secondary electrons [149], so that at constant sputtering current the voltage is decreased. The voltage then starts to increase again above 15 sccm O_2. As the target surface oxidation increases, so does the resistance of the target, hence the applied voltage required to hold a constant target current increases. By 15 sccm oxidation is sufficiently great that the effect of the resistance increase outweighs the drop in voltage due to the

additional secondary electrons. A similar relationship is observed by Venkataraj *et al.* [109]. Upon decreasing oxygen flow, the same trend can be observed, at a lower voltage level, reaching a maximum difference of ca. 20 V between 0 and 10 sccm O_2 flow. On the upward sweep of oxygen flow the target remains partially metallic, and the metal species that are sputtered are oxidised away from the target, consuming the oxygen in the plasma. In contrast, as the oxygen gas flow rate is being decreased, the target surface is changing from oxide to metal so initially, considerably less oxygen is consumed in the process, and the target surface is still exposed to a high oxygen concentration and the target remains oxidised, with a greater secondary emission, and hence keeping the voltage relatively low for a constant current. Venkataraj *et al.* [109] do not report the existence of a voltage hysteresis for a process with similar parameters, which could possibly be explained by a different size and geometry of the sputtering chamber. A larger chamber provides a larger gettering area and hence more oxygen is consumed in the chamber, rather than oxidizing the target surface, so a small change in oxygen flow will have relatively little influence on the target. Higher pumping speed as well as a smaller target to substrate distance and a small target sputter erosion zone also decrease the hysteresis width so that quantitative comparison between different chambers is not possible [149-152]. Comparison of the two cathode potential vs. oxygen flow rate curves indicates that the work by Venkataraj *et al.* was not carried out under poisoned target conditions despite higher oxygen flow rates unlike this experiment, but under conditions comparable to flow rates between 0 and 15 sccm in this work.

A similar target poisoning behaviour was observed by Pauleau *et al.* [153], who describe a steep increase of oxygen incorporation into the film with increasing oxygen flow at low oxygen content, or off a metal target and a slow increase for higher oxygen flow rates, off a poisoned target for RF sputtering.

With increasing oxygen flow rate the rate of deposition decreases as observed in Fig. 29. Thickness was determined through measurement of the final film thickness and the overall deposition time. The deposition rate decreases as the target becomes increasingly poisoned with oxide at higher oxygen flow rates. The absolute rate varies between 1 and 0.4 nm/s.

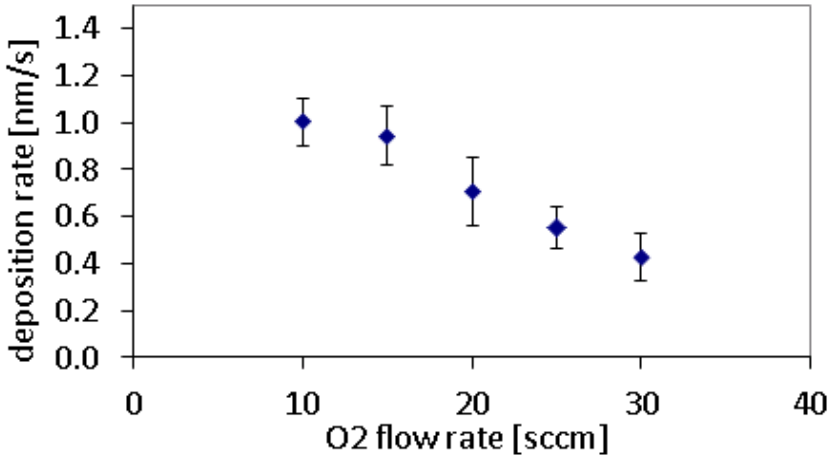

Fig. 29: Deposition rate vs. oxygen flow rate during reactive sputtering of lead oxide films.

The thickness distribution of a film deposited across a large sample showed that most material was deposited in the middle of the racetrack, with the film being thicker on the left side, where

the gas was fed into the chamber. A thickness profile is shown in Fig. 30. Subsequently, all characterized films were made in the middle of this region. XRD patterns generally show slightly narrower peaks in this middle region, indicating larger crystals, but no change in crystal structure. However, conductivity varied across the deposition zone and the most conductive, reproducible properties were found in the middle of the racetrack. This change in film thickness and grain size in magnetron sputtering has been extensively observed and modelled throughout the literature and is attributed to increased bombardment of the film with high energy ions in front of the erosion area of the target (race track) [154-158].

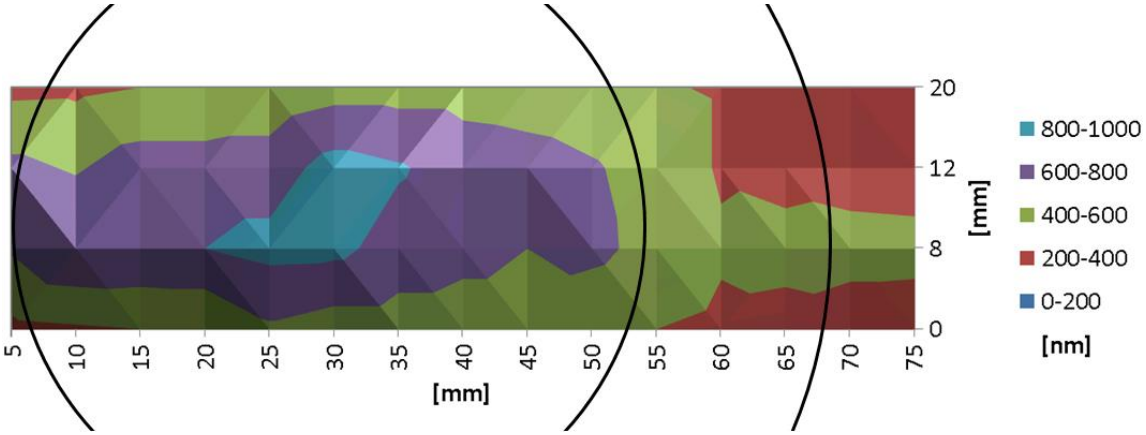

Fig. 30: Thickness distribution across a large sample with indication of the position of the racetrack.

4.2. Structural Properties

4.2.1. XRD

In order to determine the influence relative oxygen concentration has on the as-deposited lead oxide thin film, an XRD study was performed. The XRD confirms the formation of different phases and stoichiometries in films of about 700 nm thickness as shown in Fig. 31. At low oxygen flow rates up to 5 sccm PbO_{orth} is formed. Flow rates between 10 and 25 sccm yield mainly $PbO_{2\,orth}$ orientated predominantly in the (111) plane, with traces of $PbO_{2\,tet}$. The peak broadening with increasing oxygen flow rate indicates a general decrease in grain size. At 30 sccm oxygen flow the deposited material appears to be mainly amorphous with some residual $PbO_{2\,orth}$ peaks.

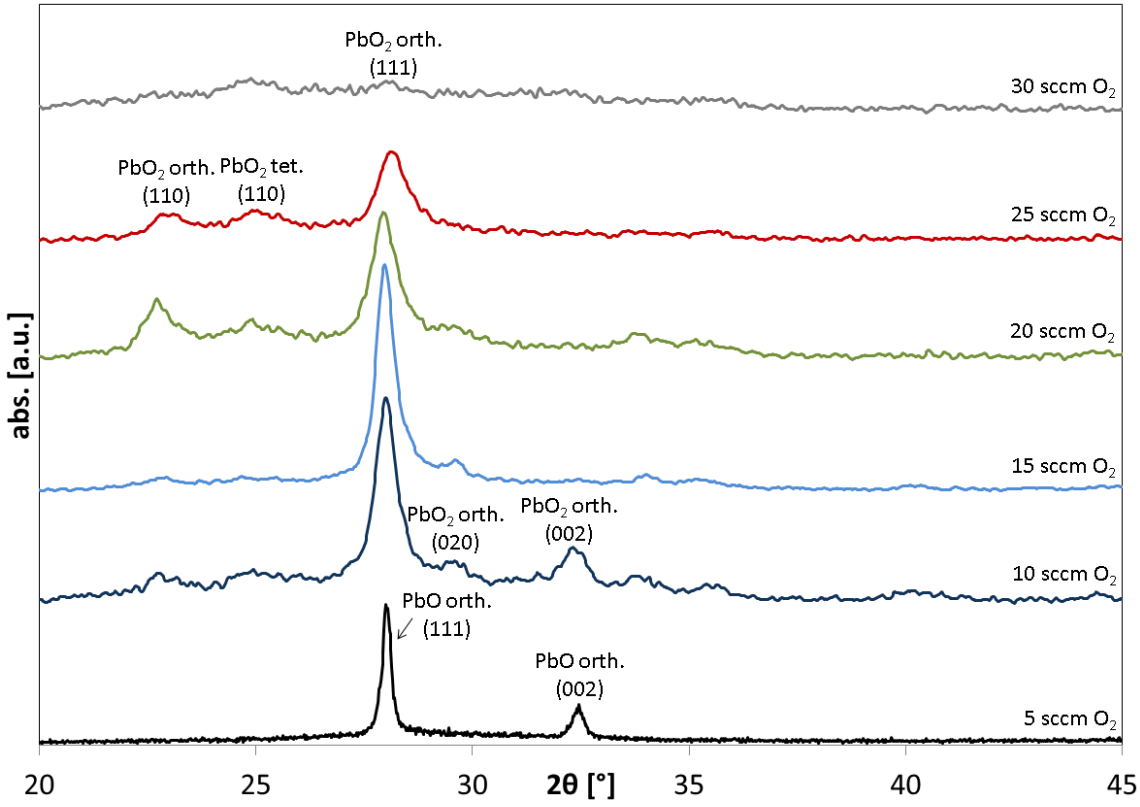

Fig. 31: XRD patterns for lead oxide films deposited at oxygen flow rates between 5 and 30 sccm show the formation of different phases of lead oxide.

Contrary to these results, Venkataraj *et al.* [109] report the formation of tetragonal, not orthorhombic, PbO at low oxygen flow rates. The heat of formation for tetragonal and orthorhombic PbO are very similar, at 217.6 kJ/mole and 220.9 kJ/mole respectively, and although the heat of formation of PbO_{tet} is slightly lower, the orthorhombic phase can be stabilized on a glass substrate (section 3.2.1) [135, 137] and small changes in the processing conditions can account for the formation of this phase at low oxygen flow rates. Pauleau *et al.* [153] find that in reactive radio frequency (RF) sputtering PbO_{orth} is preferably formed at low

gas pressures, high sputtering power and small substrate-to-cathode distances, whereas PbO_{tet} forms under the opposite condition. The PbO_{orth} films made in this study were deposited at similar pressures but slightly higher sputtering currents than the PbO_{tet} films made by Venkataraj *et al.*, thus the higher cathode discharge voltage used could provide the extra heat of formation necessary to form the more stable orthorhombic phase.

At higher oxygen flow rates PbO_2 is formed, with $PbO_{2\,orth}$ and some $PbO_{2\,tet}$ at flow rates between 10 and 25 sccm, and a relatively amorphous film with some residual $PbO_{2\,orth}$ peaks at 30 sccm oxygen, equivalent to 75% oxygen.

Venkataraj *et al.* did not report the formation of $PbO_{2\,tet}$, however Lappe [91] reports the formation of both orthorhombic and tetragonal PbO_2 for reactive sputtering of Pb, and both phases also form during electrodeposition of lead oxides [83, 159]. $PbO_{2\,tet}$ has been determined to be a stable phase at atmospheric pressures [77]. It is not possible to directly compare exact processing conditions, as the influence of gas flow rates will depend on a multitude of parameters such as chamber volume, pumping speed, overall gas flow and the location of gas inlet but many parallels exist between this study and similar ones reported in the literature.

4.2.2. Grain Size from XRD

The grain size of the different lead oxide phases was determined from the XRD peak width as plotted in Fig. 32.

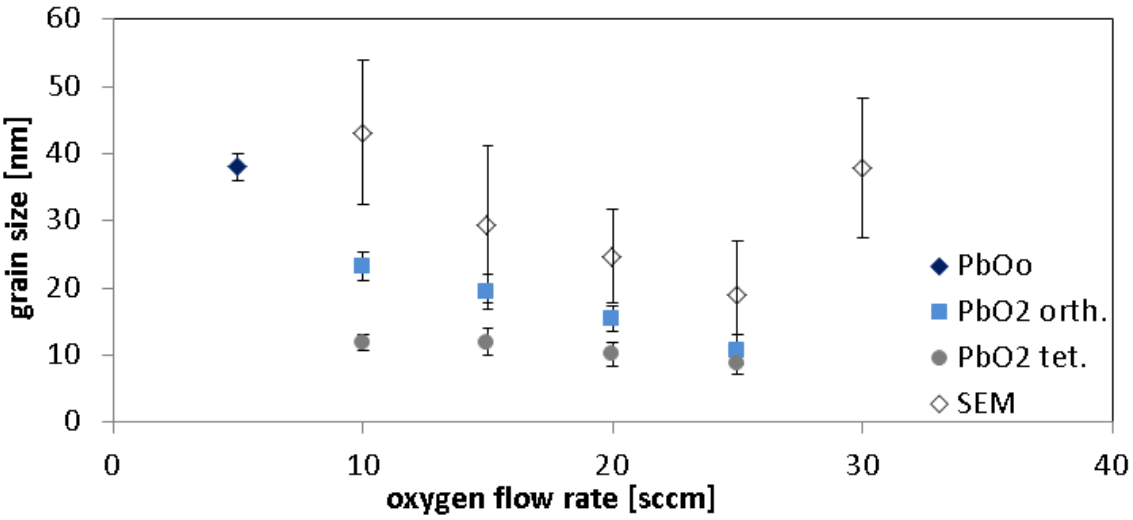

Fig. 32: Grain size of different phases of lead oxide as a function of oxygen flow rate during reactive sputtering (XRD error bars taken from the χ of the Gaussian of the fit while SEM error bars are the standard deviation of 30 domains measured in a single micrograph).

The PbO_{orth} formed at low flow rates has large grains around 40 nm, $PbO_{2\,orth}$ and $PbO_{2\,tet}$ formed at higher flow rates have smaller grain sizes between ca. 25 and 10 nm for $PbO_{2\,orth}$ and 10 to 8 nm for $PbO_{2\,tet}$. At 25 sccm grains of both phases are roughly the same size. XRD peaks at 30 sccm are not intense enough to allow for grain size determination. The grain and particle

sizes measured from SEM micrographs are also plotted on the figure, assuming there is no out of plane anisotropy they follow the same trend as the XRD derived grain size with a slight offset.

Although Venkataraj *et al.* [109] observe the formation of various phases of lead oxide, they also report a general decreasing trend in grain size with increasing oxygen flow. Reported grain sizes vary between 23 and 6 nm, roughly half of that observed in this work, for deposition rates roughly double of the ones achieved here. This indicates a correlation between grain size and deposition rate.

4.2.3. Microstructure

SEM gives information about the evolution of morphology and film homogeneity. Micrographs were recorded for films containing the two phases of PbO_2 (Fig. 33) and show reasonably smooth compact film surfaces. At low flow rates, isolated particles of around 50 nm were observed. As oxygen flow rate increases, between 15 and 25 sccm, the grains become needle shaped and more evenly distributed. Eventually, at 30 sccm, closely packed spherical particles are formed which are consistent with amorphous thin films. This confirms the grain size development determined from XRD data (Fig. 31).

As oxygen flow rate increases the dynamics of grain growth vary [160]. At low flow rates there is a higher probability that the Pb atoms can reach the substrate before interacting with an O, at the substrate the Pb and O have sufficient energy to migrate around the substrate and form

large cuboidal crystalline grains and minimize surface energy. As oxygen flow rate increases the probability of a Pb+O reaction increases which results in a reduction in the ability of the depositing species to move around on the film surface before reaction, hence the grain size decreases [161]. The formation of the anisotropic structures observed in the SEM between 15 and 25 sccm suggests that crystal growth is axially preferential which is not surprising given the unit cell of orthorhombic PbO_2. At very high oxygen flow rates (e.g. 30 sccm) the Pb either reacts in flight or very quickly upon arrival at the surface which results in large domains without crystallographic facets corresponding to a high entropy amorphous state.

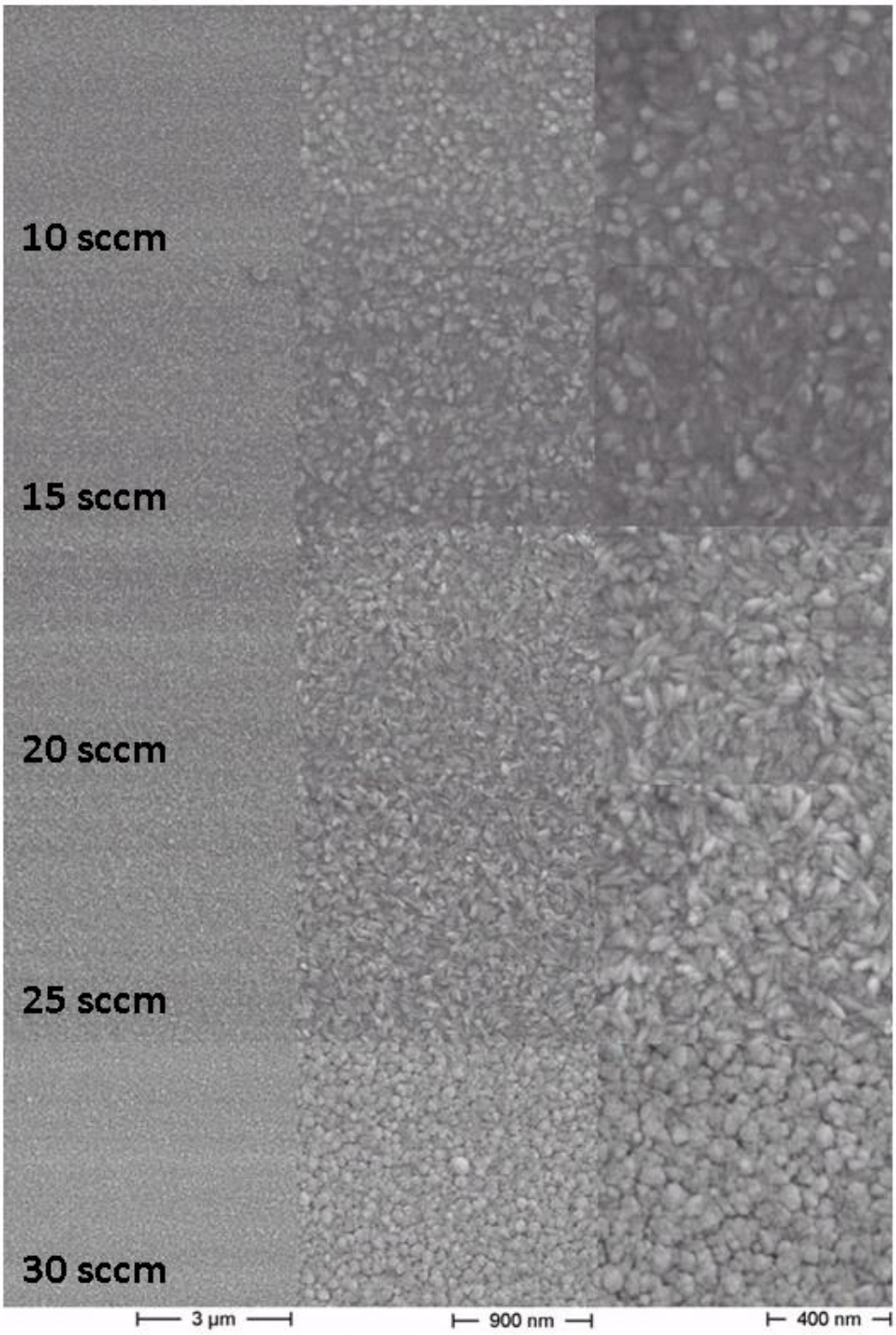

Fig. 33: SEM micrographs of PbO_2 films deposited between 10 and 30 sccm oxygen flow rate.

4.3. Electronic Properties

It is generally known that PbO_2 is highly conductive and the origin of its metal-like behaviour has been the subject of several studies since the 1960s [91, 162, 163]. A recent comprehensive study conducted by Payne *et al.* [164] on mixed tetragonal and orthorhombic PbO_2 material concludes that oxygen vacancy defects cause a large number of free charge carriers that occupy states above the conduction band, resulting in the observed high conductivity. The calculated band gap for PbO_2 is 0.2 eV though the optical band gap is strongly dependent on carrier concentration, which can be changed by gentle annealing treatments [112]. Oxygen loss is exothermic [165] and oxygen vacancies are the most stable defects in this material. A stable oxygen sub-stoichiometry of about 1.6 % accounts for charge carrier concentrations as high as 10^{21} cm^{-3}, as calculated by Scanlon *et al.* [165]. This high number of charge carriers exceeds the Mott criterion and renders the material a degenerate semiconductor, with the Fermi level being situated well inside the conduction band. Differences in the calculated fundamental band gap of about 0.2 eV and the measured optical band gap of about 1.5 eV are explained through symmetry-forbidden transitions [165] and the influence of the Moss/Burstein effect [165, 166], increasing the apparent band gap as a result of the states close to the conduction band edge being populated. Walsh *et al.* calculated the dependence of the effective optical band gap on charge carrier concentration using first-principle calculations and report a continuous range of 1.1 eV – 3.2 eV for carrier concentrations varying between 10^{18} and 10^{21} cm^{-3} [166].

PbO films sputtered at 5 sccm oxygen flow rate were too resistive to be characterized through Hall Effect measurements, hence data is only presented for films made between 10 and 30 sccm oxygen flow. All other films were conductive enough for electronic characterization and comprised of lead dioxide, containing mainly $PbO_{2\,orth}$, with some $PbO_{2\,tet}$ at intermediate oxygen flow rates between 20 and 25 sccm, as discussed with XRD data above. Results for charge carrier concentration, mobility and resistivity are presented in Fig. 34.

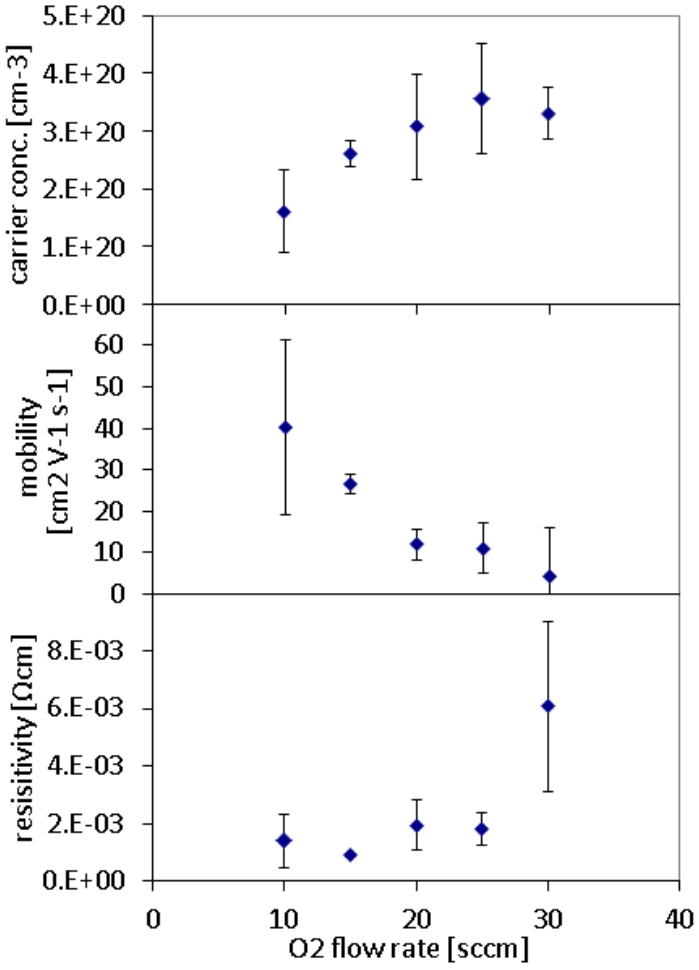

Fig. 34: Carrier concentration, mobility and resistivity of lead oxide films depending on oxygen flow rate during reactive sputtering.

PbO_2 films produced at all oxygen flow rates were highly conductive, with charge carrier concentrations increasing from $1*10^{20}$ to $4*10^{20}$ cm^{-3} and mobilities decreasing from 40 to 5 $cm^2/(Vs)$ with increasing oxygen flow rate. Both properties show considerable change between 10 and 20 sccm and plateau-out for higher flow rates.

An increasing charge carrier concentration seems to be in conflict with the increasing oxygen flow rate, as charge carriers in this n-type material arise from oxygen vacancies. Oxygen vacancies and hence charge carriers should therefore at first glance become fewer in number with increasing amount of oxygen in the chamber. Grain size, however, decreases with increasing oxygen flow rate, introducing more defects into the lattice, which also contribute to the number of charge carriers in the material. An increase in carrier concentration with increasing defect density in a less crystalline material, hence a larger proportion of grain boundaries, seems more plausible. A lower deposition rate might be expected to give rise to fewer defects, but nevertheless a smaller grain size is observed, and the carriers associated with defects at the grain boundaries appears to be the dominating factor.

It is generally recognized that in degenerate semiconductors mobility decreases with increasing charge carrier density [167-169]. Mobilities measured in the present materials indeed decrease with increasing oxygen flow rate and increasing charge carrier concentration, going along with the decreasing grain size, and in the case of the 30 sccm material due to the loss of crystallinity.

Resistivity increases slightly from 10 to 25 sccm oxygen and triples for 30 sccm, with a spread in values ranging over half an order of magnitude for the maximum oxygen flow rate. Mobility, rather than carrier concentration, is therefore the predominant factor in resistivity changes. A

correlation between mobility and resistivity in degenerate semiconductors is also observed by Slocombe *et al.* [169].

The large spread in measured values at 30 sccm can be explained by the fact that this material is highly amorphous and reproducible results were difficult to obtain under these conditions. It cannot be excluded that the drastic increase in resistivity at 30 sccm may be influenced by thickness effects. Mindt [83] observes a thickness dependent increase in resistivity below 200 nm film thickness in orthorhombic PbO_2. As the deposition rate decreases, runs at higher oxygen flow rates result in thinner final films, with the 30 sccm films lying in the range of 200 nm, so that surface scattering and inhomogeneities in the film may contribute significantly to resistivity changes.

4.4. Band-gap and Work Function

Fig. 35 shows the band gap and work function as a function of oxygen flow rate. Measured band gaps lie between 1.6 and 1.7 eV for all oxygen flow rates. This range of values corresponds well with predicted values for these carrier concentrations based on the Moss-Burstein effect and taking in to account inter- and intra-band transitions [166].

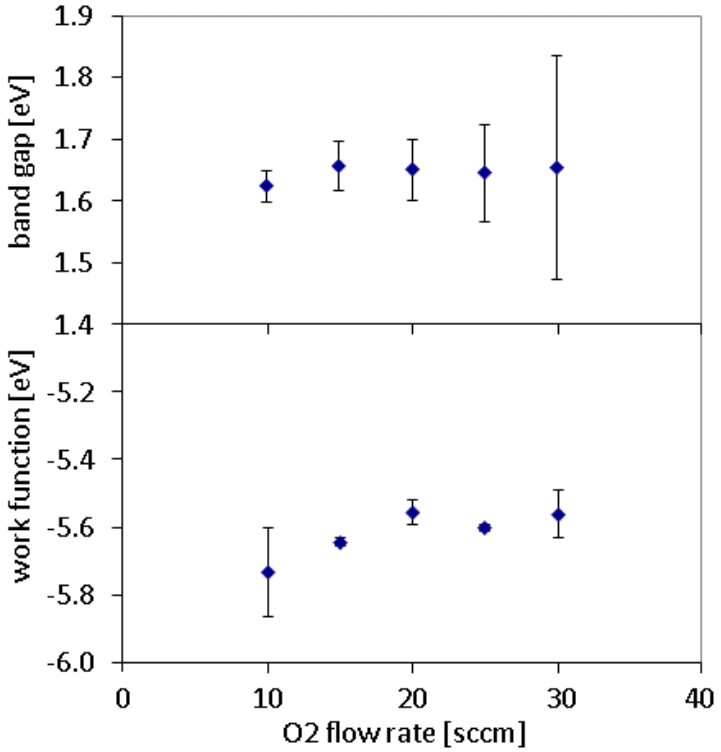

Fig. 35: Band gap and work function of lead oxide films depending on oxygen flow rate during reactive sputtering.

As was observed in Fig. 34, the 30 sccm deposition has a large spread in properties, particularly in this case the band gap. The composition of the films is similar for all flow rates in this range so that a similar band gap for all films is plausible. The possible small initial increase can be explained by the Moss-Burstein effect. At low oxygen flow rates there is a steep increase in charge carrier concentration (Fig. 34). This increased number of carriers means an increased number of occupied states above the band gap. As a result, electrons need to be elevated into a higher unoccupied state, thereby increasing the apparent optical band gap, explaining the band gap increase between 10 and 15 sccm oxygen flow.

The measured work function decreases with increasing oxygen flow rate up to 20 sccm and shows a plateau above that value, mirroring the charge carrier concentration. This correlation is also shown in Fig. 36 and demonstrates that with an increased number of charge carriers and the occupation of higher energy states, less energy is necessary to extract an electron from the material [146, 170].

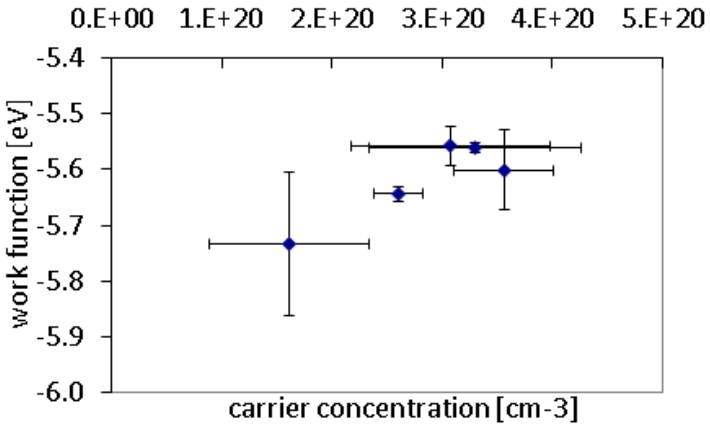

Fig. 36: Work function of $PbO_{2\ orth+tet}$ depending on carrier concentration.

4.5. Summary

The material produced so far in this chapter despite having optimal band gaps is not suitable for photovoltaic devices as it is very conductive and has a very high work function which makes it difficult to form a junction. Secondly the processing window for the production of stoichiometries between PbO and PbO_2 is very small and was not achieved in this setup. Therefore to further control the electronic properties of the films a series of post-deposition anneals was performed to take advantage of the properties of lead oxides of intermediate stoichiometries [159].

4.6. Post Deposition Heat Treatments

In order to vary the composition and properties of the sputtered films, post-deposition heat treatments were performed, in air, at 270°C. The results from structural, electronic and optical characterization follow.

4.7. Structural Properties

4.7.1. XRD

Heat treatments on thin films of lead oxide sputtered at 20 sccm oxygen flow rate as an average representative material were performed at 270°C for different durations up to 30 h. This temperature was chosen as it lies at the onset of thin film Pb oxidation and no significant ITO degradation is observed at 270°C, making it a suitable temperature for potential device processing. XRD patterns for the as-deposited film and films heat treated for 1, 5 and 30 h respectively are shown in Fig. 37.

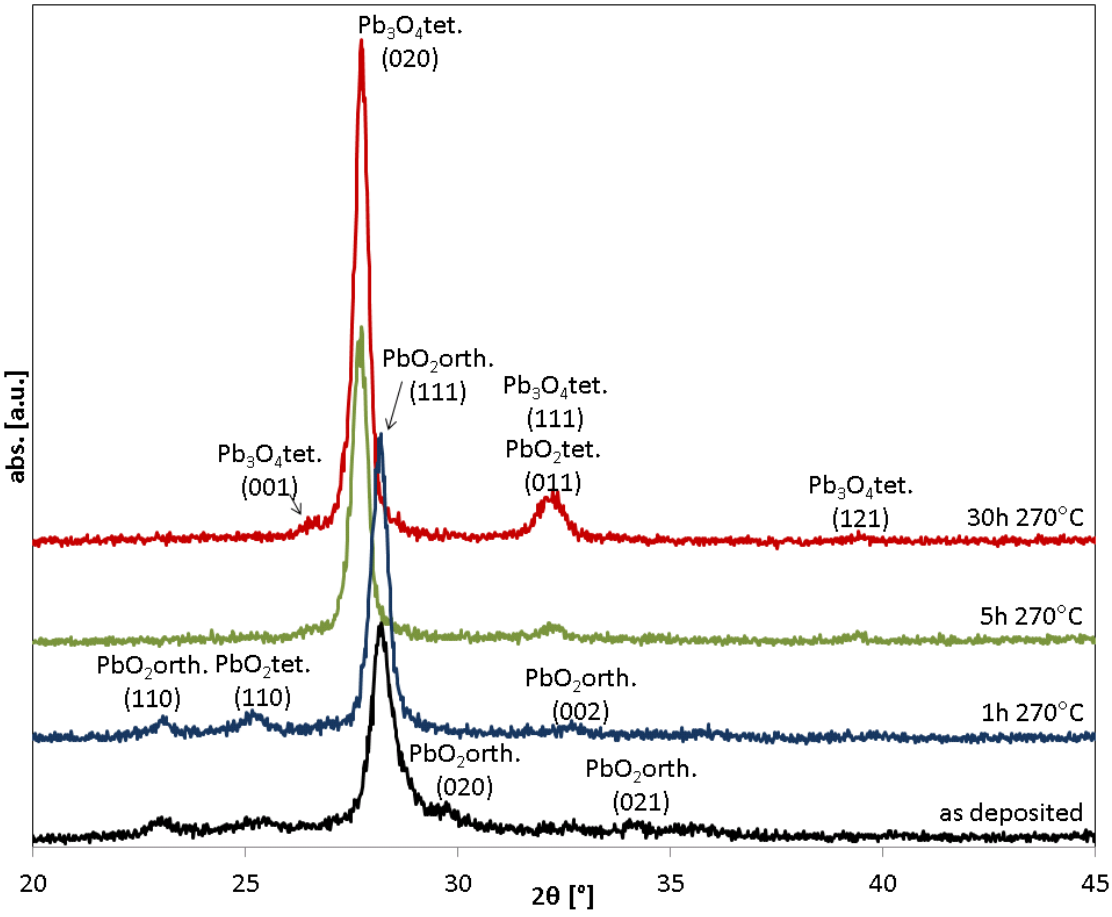

Fig. 37: XRD patterns of lead oxide films sputtered at 20 sccm oxygen flow and heat treated for different durations at 270°C.

As discussed in section 4.2.1., the as-deposited film consists of $PbO_{2\,orth}$ with traces of $PbO_{2\,tet}$. 1 h of heat treatment at 270°C provokes little to no change in phase composition, indicating that at this temperature the reaction kinetics are not fast enough to show substantial change after such a short time. The same strong $PbO_{2\,orth}$ (111) peak and weak $PbO_{2\,orth}$ (110) and (002) peaks and a weak $PbO_{2\,tet}$ (110) peak are observed in the XRD scan as in the as-deposited film.

The weak $PbO_{2\,orth}$ (020) peak observed in the as-deposited material cannot be found in the pattern measured after a 1 h heat treatment which could suggest preferentially oriented growth. The main orthorhombic peak appears slightly sharper, indicating grain growth. After 5 h the $PbO_{2\,orth}$ peaks disappear and peaks of the tetragonal Pb_3O_4 phase are observed, showing a strong (020) peak, a (111) peak and some indication of (001), (111) (121) peaks. There is some possible overlap with $PbO_{2\,orth}$ (111) and $PbO_{2\,tet}$ (011) so that the existence of both phases cannot be excluded in this material. After 30 h the pattern is very similar to the 5 h heat treatment one, but showing stronger and sharper Pb_3O_4 (020) and (111) peaks, again indicating grain growth for the longer heat treatment.

Literature data on the decomposition of PbO_2 looks somewhat contradictory at first sight, as the formation of new phases seems to be strongly dependent on temperature, heating rate and duration of the respective heat treatment. Aleksandrov *et al.* [171] found no formation of Pb_3O_4 at all for high heating rates of $2*10^2$-$2.5*10^3$ °C/s, but report the formation of Pb_3O_4 in a second reduction step from the metastable phase $Pb_{12}O_{19}$ at 470°C for lower heating rates between 0 and 0.2°C/s, and further decomposition into PbO_{tet} and subsequently PbO_{orth} at 600°C. Venkataraj *et al.* [74] report grain growth but do not observe any phase change of PbO_2 at 300°C. They report the formation of the tetragonal $PbO_{1.55}$ phase at 400°C, hence less oxygen loss than was observed here at 270°C. At 500°C they report the formation of PbO_{orth}. Venkataraj *et al.*, however, performed all their heat treatments for just one hour, so that the observed differences in phase changes reflect the strong influence of kinetics especially at low temperatures. In the present work heat treatments were conducted at the low temperatures necessary by the underlying ITO, and for longer times, leading to the formation of the

equilibrium phase Pb_3O_4. Burgio *et al.* [172] document the decomposition of PbO_2 under laser irradiation and observe the pathway $PbO_2 \rightarrow Pb_3O_4 \rightarrow PbO_{tet} \rightarrow PbO_{orth}$, pointing towards it being the same decomposition process as was observed in the present work. Peter [173] studied the reduction of $PbO_{2\ orth}$ in aqueous sodium tetraborate and also finds no evidence of the formation of non-stoichiometric phases.

4.7.2. Grain Size from XRD

Grain size determined from XRD data show a general trend of increasing grain size with longer heat treatments (Fig. 38). $PbO_{2\ orth}$ and $PbO_{2\ tet}$ grain sizes increase from around 20 to 25 nm and 9 to 16 nm after 1 h at 270°C. The newly formed Pb_3O_4 phase after 5 h shows an average grain size of about 24 nm, roughly the same as the largest PbO_2 grains after 1 h. A slight increase in grain size is observed for Pb_3O_4 grains between 5 and 30 h of heat treatment.

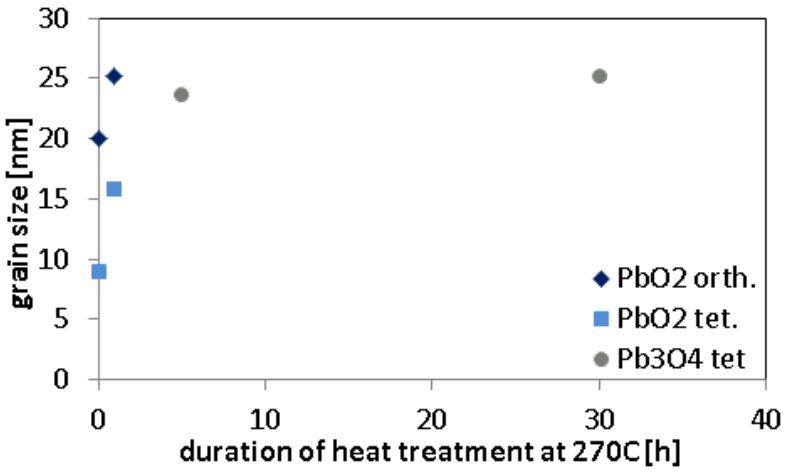

Fig. 38: Grain size for lead oxide films sputtered at 20 sccm oxygen flow and post deposition heat treated for different durations at 270°C.

4.8. Electronic Properties

Hall Effect measurements were made to observe the changes in electronic properties with heat treatment at 270°C. All films measured were n-type. The results for charge carrier concentration, mobility and resistivity are displayed in Fig. 39.

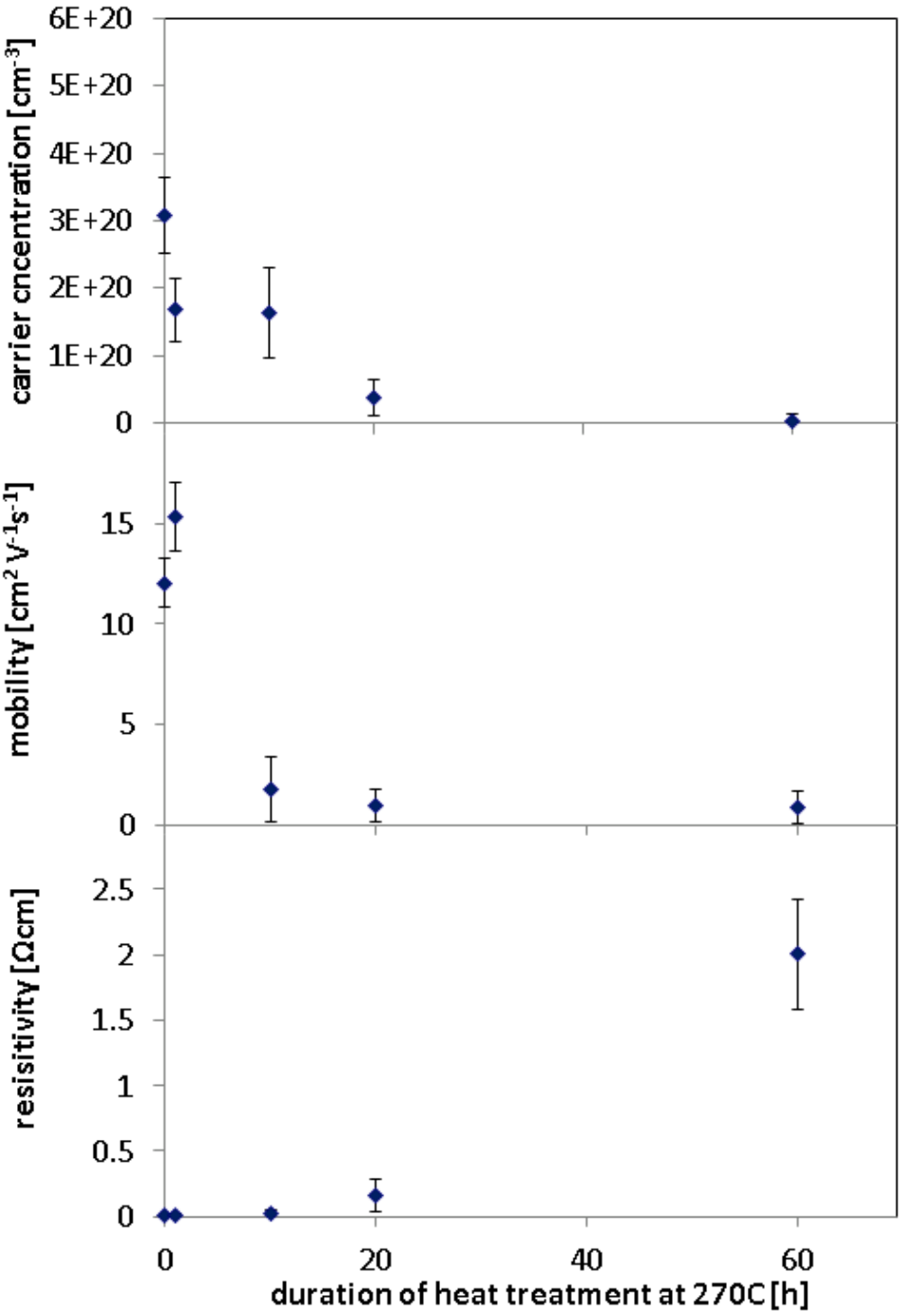

Fig. 39: Carrier concentration, mobility and resistivity of lead oxide films sputtered at 20 sccm oxygen flow depending on the duration of post deposition heat treatment at 270°.

After one hour of heat treatment a decrease in carrier concentration and increase in mobility is observed. Resistivity shows a negligible increase. As discussed in the previous section, during this heat treatment step no phase change is observed and the increased mobility can be explained by the increased grain size or the reduction in the number of oxygen vacancies leading to a reduction in the number of scattering centres. This result is reflected in the reduction in carrier concentration.

There is a drop in mobility after 10 h at 270°C, whereas carrier concentration stays approximately the same, and resistivity increases by an order of magnitude. The material investigated in this case is no longer PbO_2 but consists of mainly Pb_3O_4, which is not a degenerate semiconductor and is known to be much more resistive than PbO_2 [94, 174], although not much information can be found in the literature on the conductivity and the charge carrier behaviour of Pb_3O_4. Peter [173] cites a study stating that Pb_3O_4 appears to be a p-type semiconductor or insulator, however no further details are given on the processing or production of this material, so that a comparison to the films discussed here is not possible. Mobility does not show significant changes for longer heat treatments whereas charge carrier concentration shows a small decrease for heat treatments up to 60 h and resistivity seems to show an exponential increase towards 60 h. The decrease in carrier concentration points towards the possible filling up of oxygen vacancies, meaning that for Pb_3O_4 the present conditions are not reducing, and a temperature of 270°C is not high enough to reduce the oxide any further.

4.9. Optical Properties

Band gap and work function were measured depending on the duration of the post deposition heat treatment and are displayed in Fig. 40. Band gaps are determined to be around 1.5 eV for the as-deposited $PbO_{2\ orth}$ and increase with a logarithmic trend with increasing duration of heat treatment, approaching roughly 2.1 eV, the band gap of Pb_3O_4. The main band gap change is observed in the phase change region between 1 and 5 h, after which the measured band gap approaches the final value.

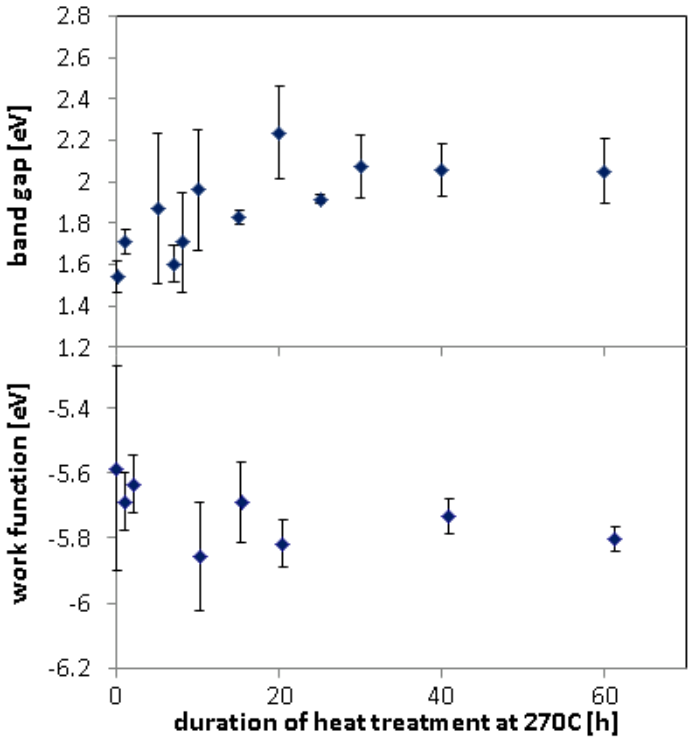

Fig. 40: Band gap and work function of lead oxide thin films sputtered at 20 sccm oxygen flow depending on the duration of post deposition heat treatments at 270°C.

The work function increases slightly from around -5.6 eV to -5.8 eV with the change from PbO_2 to Pb_3O_4.

4.10. Summary

Thin films of lead oxide were produced by reactive sputtering. Depending on oxygen flow rate either PbO or PbO_2 could be formed and with an *ex-situ* anneal Pb_3O_4 could be made. The as-produced films were n-type and demonstrated very high conductivities and carrier concentrations, the level of which could be controlled by the *ex-situ* anneal. The band gaps of the materials produced ranged from 1.6 to 2.1 eV which is in the ideal range for photovoltaic applications. The work function of the materials spanned from 5.6 to 5.8 eV, this presents a challenge to making photovoltaic devices as it is very hard to make a metal or semiconductor junction with such a high work function material.

5. Photovoltaic Devices Based on Lead Oxide Thin Films

To ascertain the potential of lead oxide materials for photovoltaics, a number of device configurations are prototyped. The materials produced in chapters 3 and 4 are incorporated in both Schottky and heterojunction type devices. A number of thin film treatments and device geometries are examined in this chapter in an attempt to improve junction performance. In parallel with device characterization, Kelvin probe (KP) measurements are used to understand the mechanism of junction formation and aid the next generation of device design.

5.1. Evaporated Films: Schottky Junctions

The starting point for all the work contained within this thesis was the result that an air-annealed thin film of lead deposited on a patterned ITO anode with a thermally deposited aluminium cathode produced a photovoltaic diode junction. Fig. 41 shows the dark and light current density versus voltage (*JV*) characteristics.

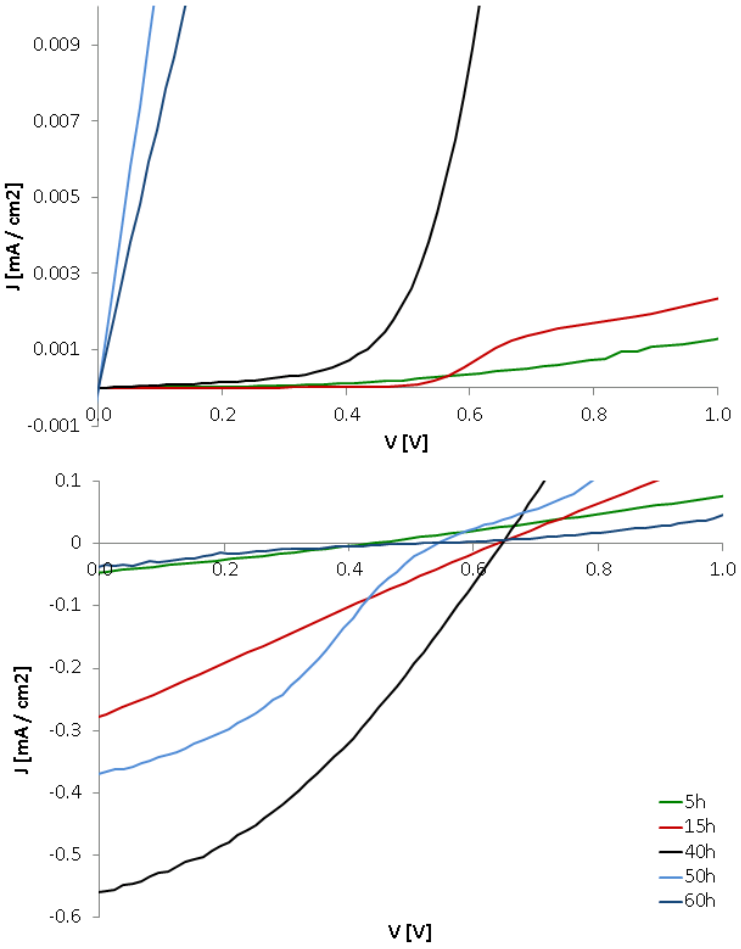

Fig. 41: JV curves for thermally evaporated and oxidized lead films sandwiched between an Al and an ITO electrode in the dark (top) and under illumination (bottom).

From the polarity of the device connection to the *JV* measurement set-up it was ascertained that electrons flow to the Al contact and holes to the ITO. Assuming PbO is p-type [130] a Schottky junction forms between PbO and the aluminium electrode, while an ohmic contact is formed at the ITO interface. This hypothesis will be further tested in the course of this chapter. Table 3 lists the key solar cell parameters derived from the *JV* curves for different annealing times:

Table 3: Photovoltaic device parameters for Schottky junctions oxidized for different times at 270°C.

HT [h]	J_{SC} [mA / cm^2]	V_{OC} [V]	**FF**	**PCE** [%]	R_s [Ω cm^2]
5	0.05	0.46	0.30	0.008	8300
15	0.28	0.68	0.26	0.063	2400
40	0.56	0.68	0.37	0.176	650
50	0.37	0.58	0.36	0.079	2000
60	0.04	0.51	0.19	0.004	10000

Under illumination the 40 h sample shows the lowest series resistance. Fig. 42 shows the correlation between J_{SC} and R_S for different anneal times. This is attributed to the changing phase composition of the material between tetragonal and orthorhombic. After 40 h the films show the highest percentage of tetragonal PbO (section 3.2.1.) which is reported to have resistivities two orders of magnitude lower than orthorhombic PbO and is more photosensitive because of its broader spectral response and a longer carrier range [130]. As a consequence, the short circuit current increases with increasing annealing time up to 40 h and decreases

thereafter as more orthrhombic material is formed. In addition, tetragonal grain size is seen to increase until 15 hours while the orthrhombic grain size increases between 15 and 60 hours, which could also contribute to improved conductivity observed due to the expected improvement in charge mobility [175, 176].

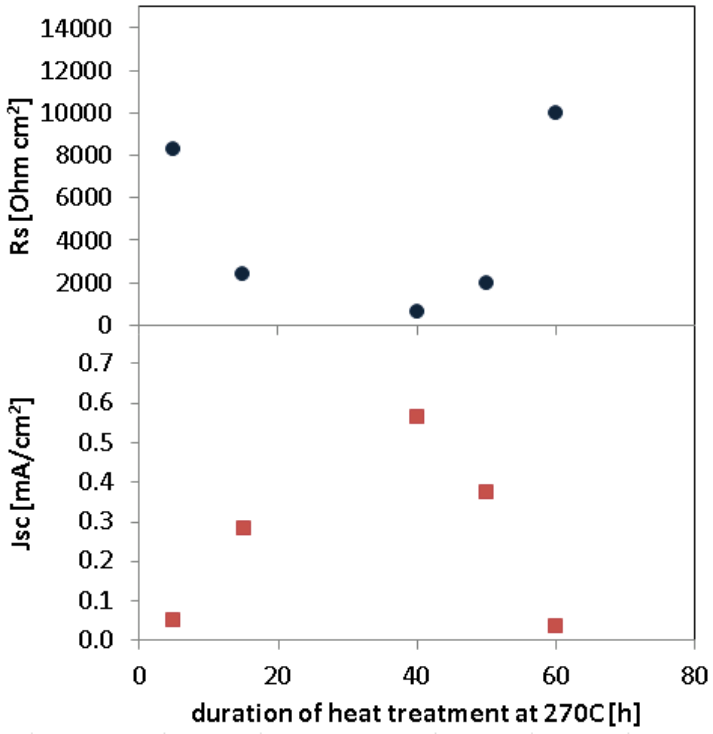

Fig. 42: Series resistance and short circuit current versus annealing time for lead oxide thin films.

The open circuit voltage increases up to 15 h where it plateaus, until it starts decreasing again after 40h. This trend can be explained by XRD combined with Kelvin probe measurements. The initial increase is attributed to the conversion of metallic lead to semiconducting lead oxide

which, as observed from XRD, is complete after 15 hours. Kelvin probe measurements also support this observation (Fig. 43) and show that the work function of the lead oxide film increases with increasing oxidation time.

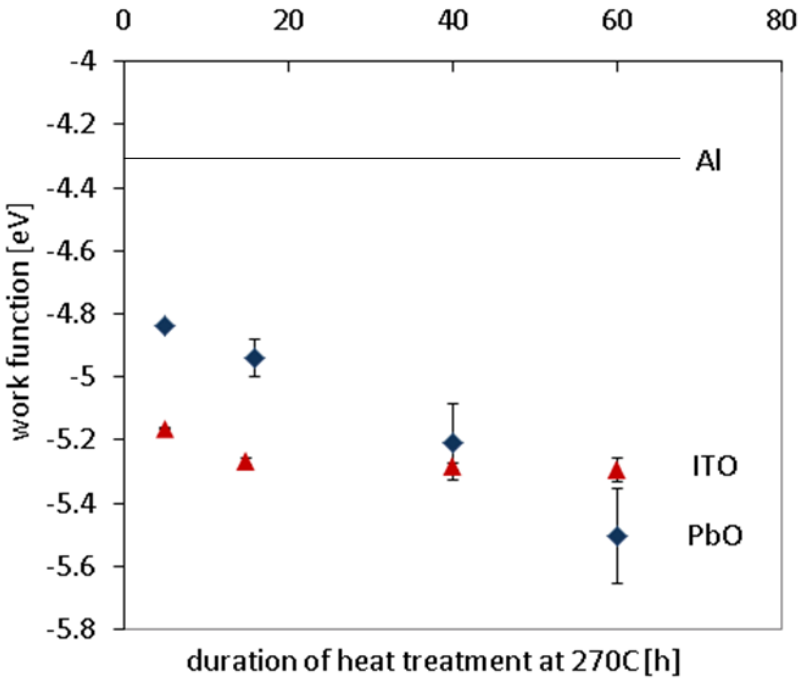

Fig. 43: Work function versus duration of heat treatment for PbO and ITO compared to the work function of Al (not heat treated).

Fig. 43 also compares PbO work function to those of the two electrodes, ITO and Al. It is clear from this that there is a crossover of workfunction of ITO and PbO at around 40 hours. This is the point of maximum V_{OC} determined from the current-voltage characteristics (Fig. 41). Fig. 44 compares work function with V_{OC}. After 40 h the lead oxide work function drops below that of

ITO, changing the nature of that interface from ohmic to a junction which is in the opposite direction to the Schottky diode formed between PbO and Al, thereby limiting the maximum possible potential difference for this materials combination. Secondly, above 40 h the work function difference between PbO and Al approaches 1, which is close to $E_G/2$, meaning that an inversion layer will form at larger barrier heights, thereby limiting V_{OC} [14]. V_{OC} of ~0.7 ± 0.09 V were achieved which is reasonably good for a Schottky junction made with a 2.2eV band gap material; theoretically the maximum attainable V_{OC} is 1.1eV before an inversion layer is formed.

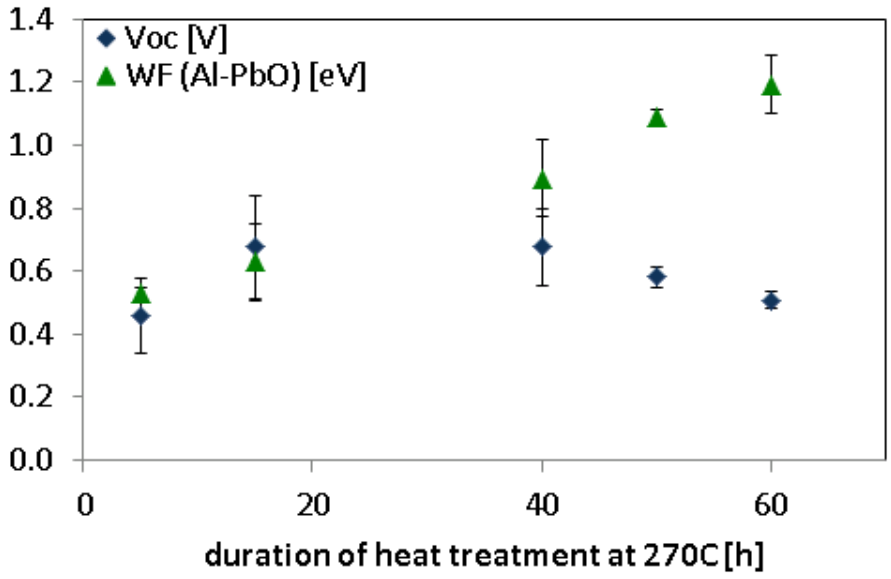

Fig. 44: V_{OC} compared to the work function difference between PbO and Al at the Schottky interface. At 40 h the Fermi level of PbO drops below that of the ITO electrode, thereby limiting V_{OC}.

Drawing the relative work functions of the three materials used in the Schottky device the following band structure emerges (Fig. 45):

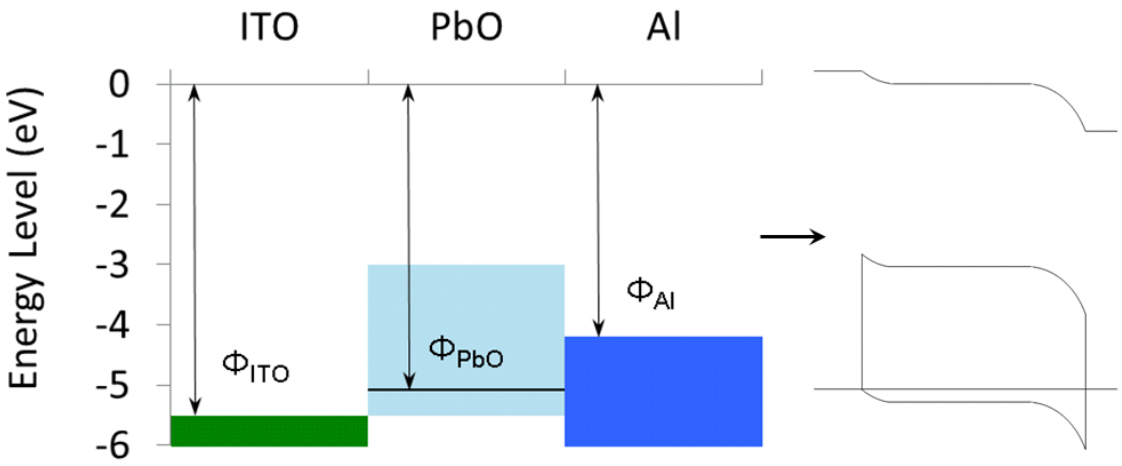

Fig. 45: Band alignment of ITO, PbO and Al in the discussed Schottky device (left) and proposed band structure of the materials in contact (right).

The cases below and above 40 hours of heat treatment are sketched in Fig. 46. Below 40 hours the maximum attainable work function difference between PbO and Al is not exploited which limits the V_{OC}. [14]. Open circuit voltages of diodes in series are additive. This means that with a second, opposing, junction forming at the front contact for heat treatments longer than 40 hours, the V_{OC} of this undesired ITO-PbO junction will be subtracted from the V_{OC} of the main Al-PbO Schottky junction. Since the Al-PbO V_{OC} is close to the maximum attainable due to the limit given by the inversion layer it cannot rise much further, so that the overall V_{OC} of the

device is reduced with the further increase of the PbO work function and the formation of this second barrier.

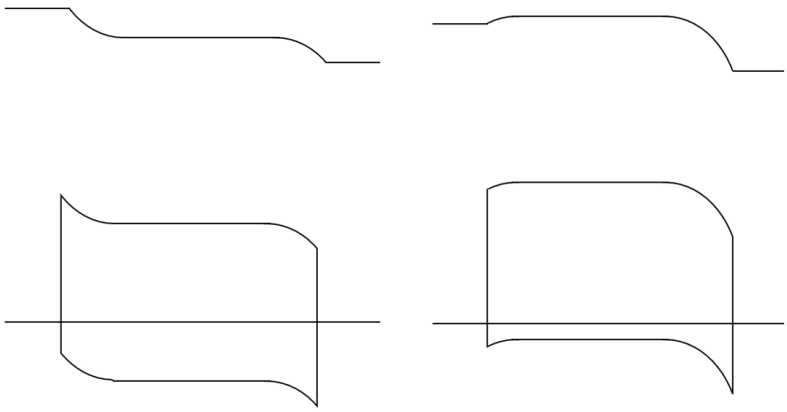

Fig. 46: Sketch of band structures for heat treatments shorter (left) and longer (right) than the optimum. In the left hand case the entire potential height of the barrier is not exploited resulting in a lower V_{OC}, whereas in the case illustrated on the right, the work function of the active layer is higher than that of the ITO front contact resulting in an opposed Schottky barrier, thereby also reducing device efficiency.

From the KP it is not possible to ascertain the position of the Fermi energy within the band gap but it is assumed that since the material is p-type the Fermi level is close to the valence band. This model of the band alignment confirms the hypothesis that an ohmic contact forms between PbO and ITO and a Schottky junction between PbO and Al. If the PbO were n-type the measured Fermi energy would result in an ohmic contact between PbO and Al and a very small

Schottky junction between PbO and ITO resulting in a V_{OC} much lower than observed in *JV* measurements.

Typically conversion efficiencies of around 0.1 % were achieved for devices fabricated via this route. The main limiting factor for these devices is J_{SC}, which could not be pushed above 0.5 mA/cm^2 although for single junction cells with a band gap around 2.3 eV the maximal theoretical current lies in the order of 10 mA/cm^2 [72]. Devices show an average of 35 % transmission in the visible region and, neglecting losses due to reflection and refraction, theoretical current densities lie in the range of 6.5 mA/cm^2. Due to the device architecture most light is absorbed at the ITO-PbO interface where it enters the device and charges generated at the PbO-Al junction have to travel far to reach the contact so that maximum current is not expected to be reached due to losses related to this structure. However, some improvement seems possible. In order to improve the material's carrier mobility it was decided to use hydrogen passivation treatments using forming gas on devices.

5.1.1. Hydrogen Passivation Treatment

Devices with lead oxide films annealed for the optimal time of 40 hours were subjected to a second annealing step in a tube furnace with 5% hydrogen in nitrogen gas flowed over them for 30 min at 100°C, 200°C and 300°C, prior to the deposition of Al top electrodes. *JV* characteristics are displayed in Fig. 47.

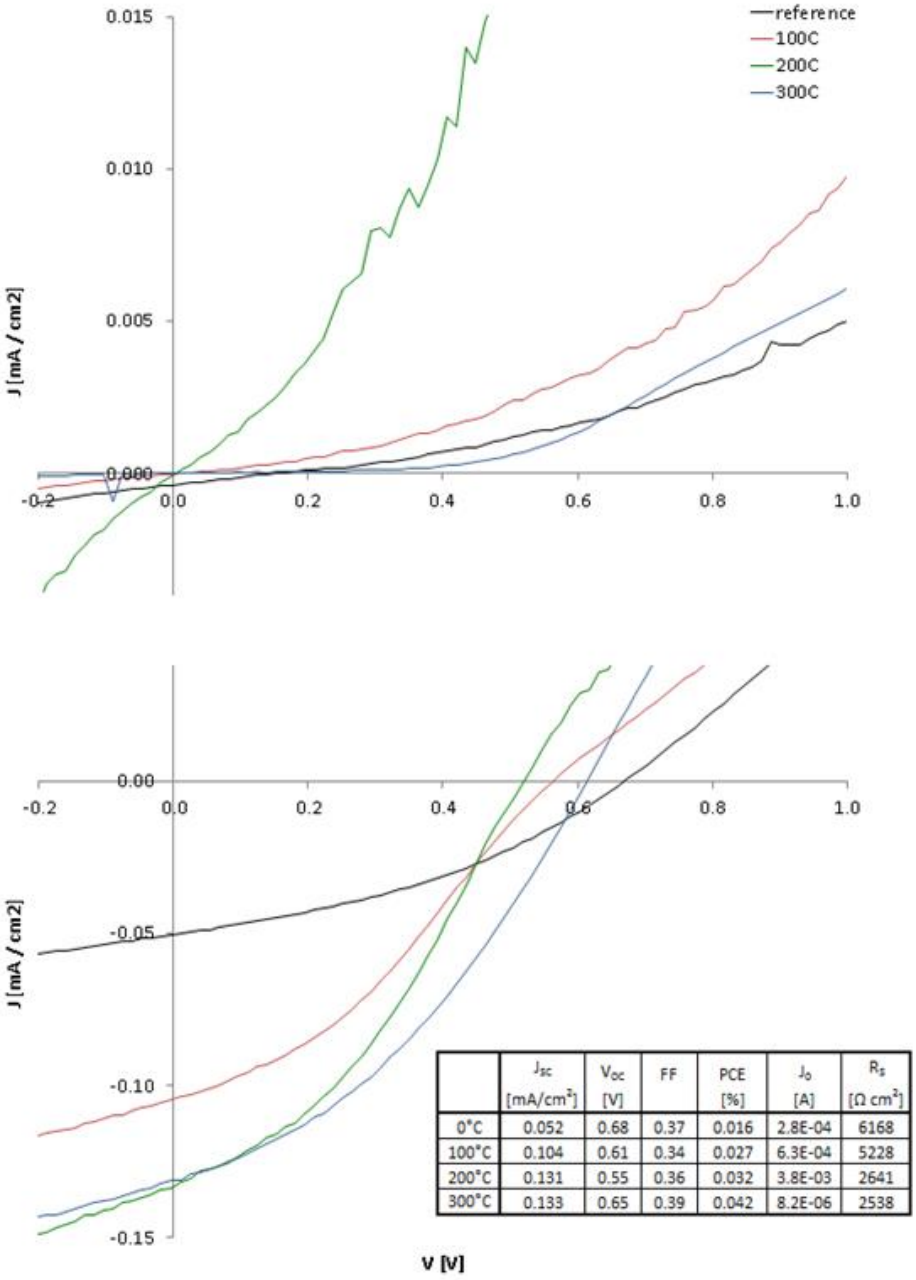

	J_{sc} [mA/cm^2]	V_{oc} [V]	FF	PCE [%]	J_0 [A]	R_s [Ω cm^2]
0°C	0.052	0.68	0.37	0.016	2.8E-04	6168
100°C	0.104	0.61	0.34	0.027	6.3E-04	5228
200°C	0.131	0.55	0.36	0.032	3.8E-03	2641
300°C	0.133	0.65	0.39	0.042	8.2E-06	2538

Fig. 47: JV characteristics of devices after a 30 min heat treatment in Ar-H_2 atmosphere at different temperatures. Dark curves are on top, illuminated at the bottom. The insert shows the most important device parameters.

An increase in PCE is observed that is mainly driven by an increased J_{SC}, together with slight variations in V_{OC}; the fill factor shows no significant change. The crystal structure of the photoactive films does not show significant changes after hydrogen annealing and grain size (as manifested in peak widths in the XRD) does not vary significantly between anneal times. As observed in section 3.2.1. the tetragonal and orthorhombic phases are in competition with each other and slight variations in relative composition are observed, for example at 100°C and 200°C the proportion of orthorhombic PbO is slightly increased. As noted in section 5.1. this affects device performance, so changes in V_{OC} and J_{SC} could be attributed to this until 200°C (Fig. 49).

Fig. 48 shows XRD patterns of the reference and hydrogen treated films.

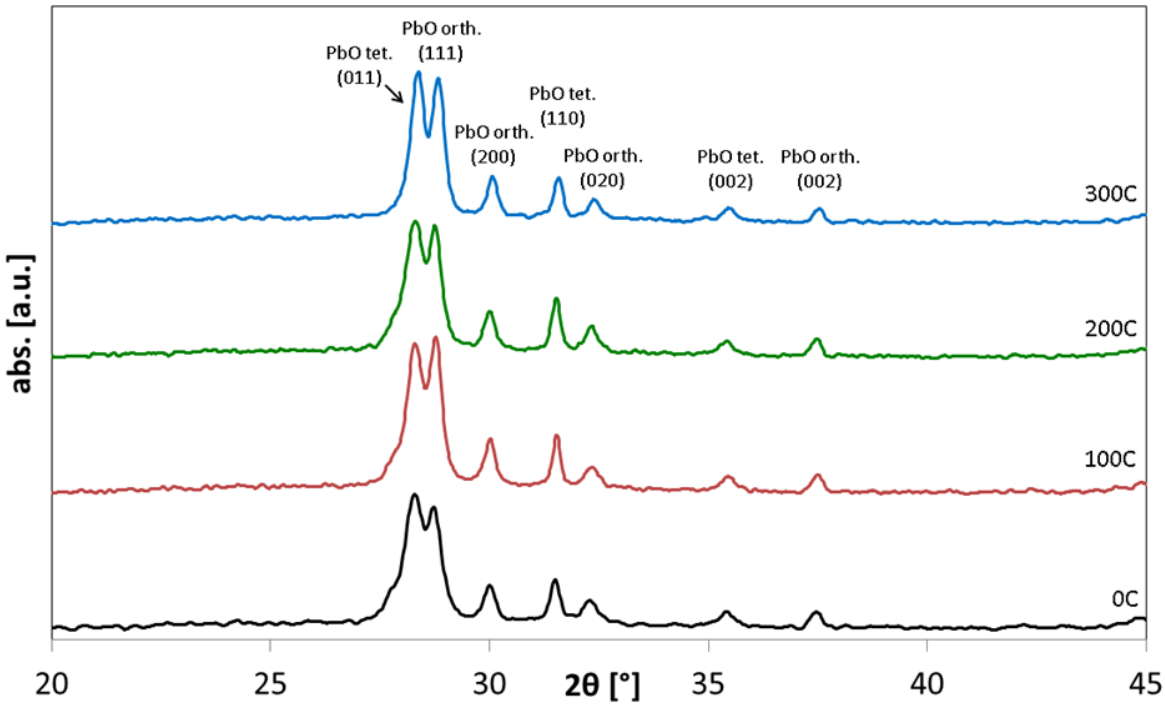

Fig. 48: XRD patterns of PbO films after a 30 min heat treatment in Ar-H_2 atmosphere at different temperatures.

Many authors have observed the improvement of electronic properties of amorphous and polycrystalline materials following a hydrogen atmosphere anneal and show that the hydrogen passivates grain boundaries leading to less recombination [38, 39, 44, 48, 72, 177], this is manifested in the dark current (J_0). J_0 remains roughly the same for anneal temperatures up to 200°C while there is dramatic reduction by two orders of magnitude at 300°C indicating that grain boundary passivation occurs and recombination is decreased.

The increase of J_{SC} with decreasing R_S is shown in Fig. 49. The values improve for 100°C and 200°C and plateau after that, suggesting that J_{SC} is more influenced by crystal stoichiometry and grain size than grain boundary passivation.

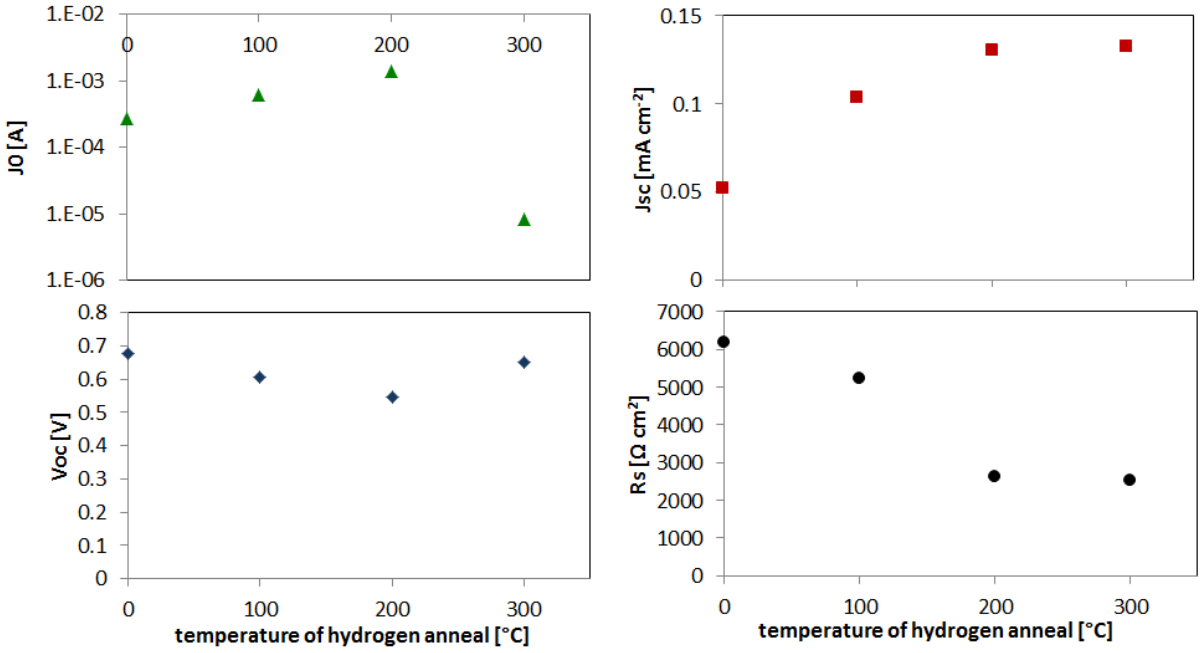

Fig. 49: Dark saturation current J_0, open circuit voltage V_{OC}, short circuit current J_{SC} and series resistance R_S depending on the temperature of hydrogen annealing.

Although passivation treatments lead to improvements in short circuit currents, overall efficiencies of the Schottky junctions are still low. Due to the very high resistivity of the PbO, film properties such as mobility and charge carrier concentration cannot be measured directly and further tuning of the properties proved to be very difficult. Higher oxides of lead are reported to show different properties including higher conductivity and lower band gaps that

make them promising materials for solar cell applications. As it is not possible to produce oxides of higher stoichiometry via the method of thermal evaporation and oxidation of thin films of lead without using high pressures, photovoltaic devices were fabricated using reactive sputtering of lead oxide films.

5.2. Junctions with sputtered lead oxide films

5.2.1. Semiconductor Metal Junctions

The first set of devices was fabricated using lead oxide, reactively sputtered at 20 sccm of oxygen sandwiched between ITO and Al. *JV* characteristics are shown in Fig. 50. This flow rate was chosen as it lies in the middle of the processing window to reproducibly make homogeneous, conductive PbO_2.

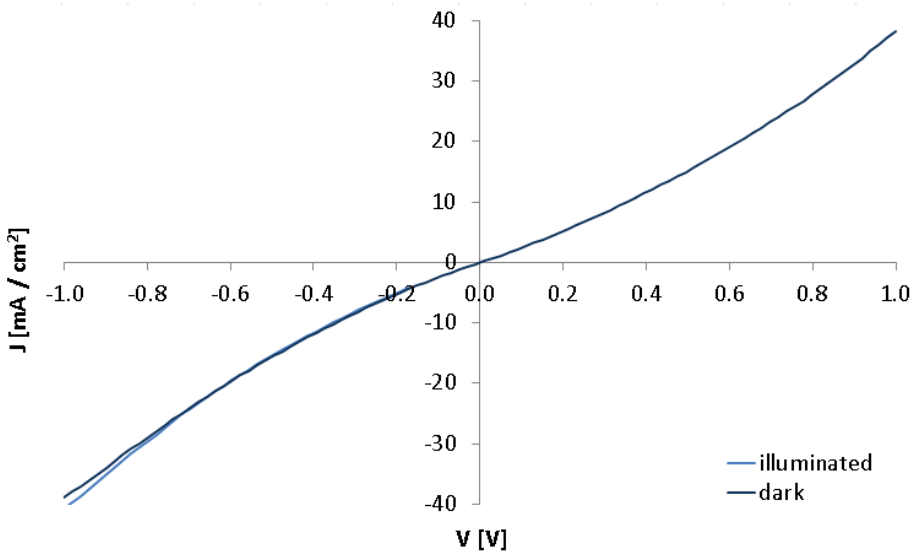

Fig. 50: JV characteristics for an ITO-PbO_2-Al device.

This configuration does not show rectifying behaviour and there is no change between dark and illuminated measurements. This is consistent with the electronic characterisation results from chapter 4, as the work function of PbO_2 lies below that of both aluminium and ITO, so that ohmic contacts are formed at both interfaces (Fig. 51).

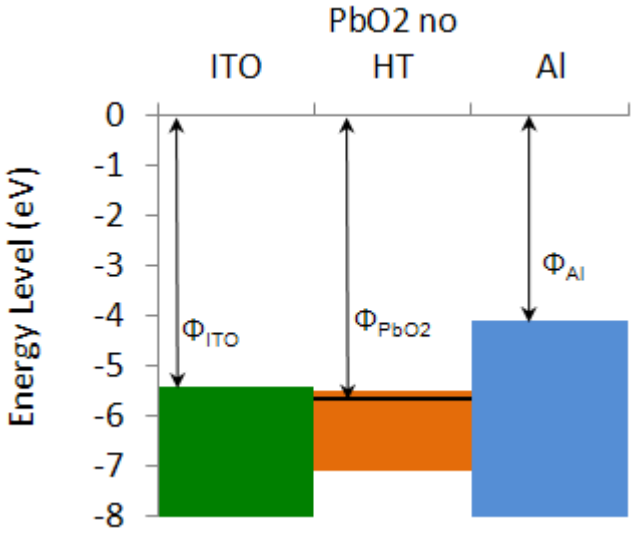

Fig. 51: Sketch of the band alignment of an ITO-PbO_2-Al device according to work functions measured by KP.

In addition, the PbO_2 films are highly conductive and open circuit conditions do not occur, hence no photovoltage can be sustained [159]. It was shown in chapter 4 that stoichiometry changes with heat treatment so that charge carrier concentration and hence mobility, conductivity and the level of the Fermi energy of the lead oxide film can be modified. The Fermi level of the heat treated films lies even lower below that of ITO and Al and the heat treated material is therefore unsuitable to form a Schottky junction with either of the electrodes. Platinum has a range of work functions [178-180], the lowest values of which would potentially make a Schottky junction however the sputtered platinum available to us had a work function of -5.2 eV and did not make a junction.

The next promising junction alternative is an n+:n junction, this was shown to be a viable device by Cao *et al.* [181], in this case between a sputtered and heat treated PbO_2 film and a PbO_2 film in the as-deposited state.

5.2.2. n+:n Junctions

A recent study by Cao *et al.* [181] shows the formation of a junction between two n-type metal oxides (copper oxide and doped lead oxide) of different work function, reaching power conversion efficiencies of up to almost 0.6 %. In this work, devices were made on ITO with heat treated sputtered PbO_2, reduced to Pb_3O_4 via a post-deposition heat treatment and as-deposited PbO_2 with aluminium as a top electrode.

The first PbO_2 film was annealed for 5 hours at 270°C, increasing its work function from about 5.6 eV to 5.8 eV while also cutting its charge carrier concentration in half from $3*10^{20}$ to $1.5*10^{20}$ cm^{-3} and increasing its resistivity. This was a promising sign that potentially a photovoltaic junction could be formed between the two differently processed films of reactively sputtered lead oxide. *JV* curves of such a device are shown in Fig. 52.

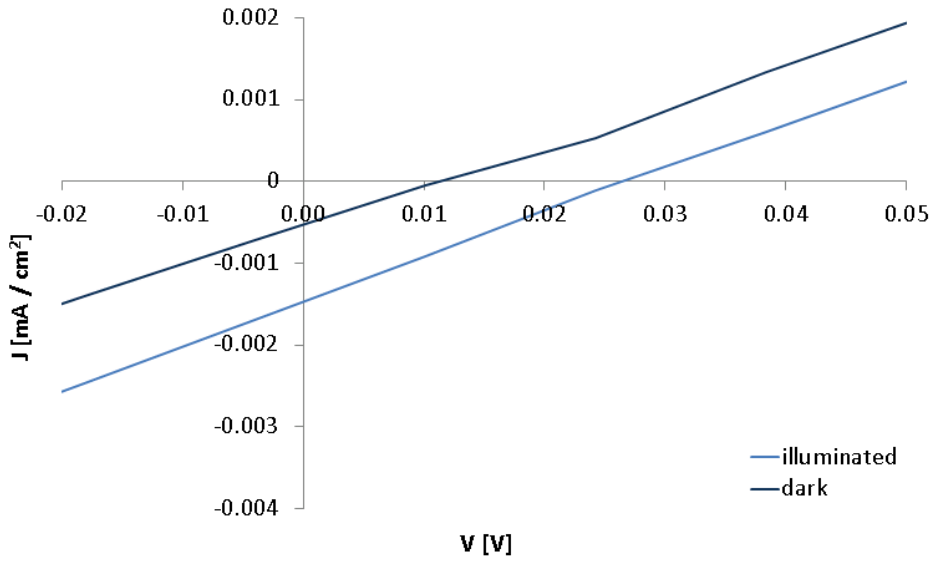

Fig. 52: Current-voltage characteristics of n+-n junctions between heat treated and as-deposited reactively sputtered PbO_2.

The devices do not show distinct rectifying behaviour and only a minimal change in current can be measured between the dark and illuminated condition. This shows that the change in carrier concentration and Fermi level induced by the heat treatment is not substantial enough to create a distinct junction between the two materials. A sketch of the band structure of this type of device is displayed in Fig. 53. It can be concluded that ohmic contacts are formed at both electrode interfaces, but the junction formed between the two lead oxide films is very small and cannot facilitate efficient charge carrier separation.

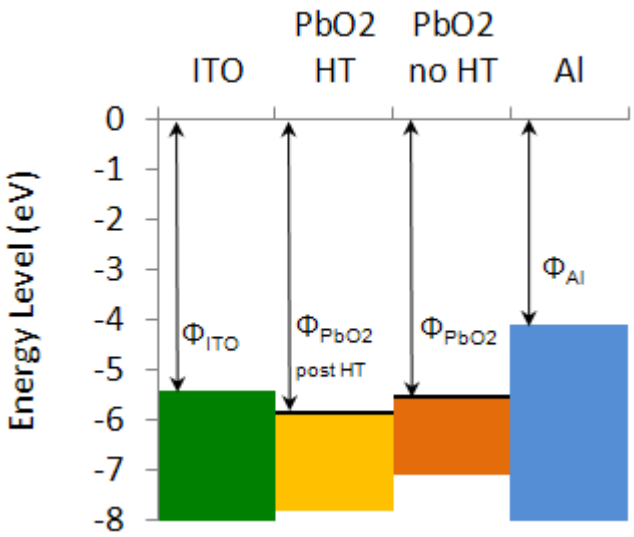

Fig. 53: Sketch of the band structure of an n+:n junction between differently processed sputtered PbO_2 films according to work functions measured by KP.

Since the as-deposited PbO_2 is not photoactive it does not contribute to the absorption of light at the junction but acts more like a metal, which gives this n+:n a Schottky character. As a consequence, an attempt was made at fabricating p-n junctions, using the evaporated and oxidised PbO p-type material paired up with the sputtered and heat treated n-type material.

5.2.3. p – n Junctions between evaporated and oxidized p-type PbO and sputtered n-type PbO_2

To take advantage of the different properties emerging with varying stoichiometry of the lead oxide films fabricated under different conditions, p-n junctions were made between evaporated Pb oxidized to PbO and heat treated sputtered PbO_2.

For the p-type layer Pb was oxidized for 60 h to create a high work function PbO film. For the n-type layer sputtered PbO_2 was annealed in a short 5 h heat treatment in order to reduce the material to Pb_3O_4 and decrease conductivity and change the materials properties from degenerate semiconductor to semiconductor, while keeping the increase in work function to a minimum. Current-voltage characteristics of such a junction between ITO and aluminium electrodes can be seen in Fig. 54.

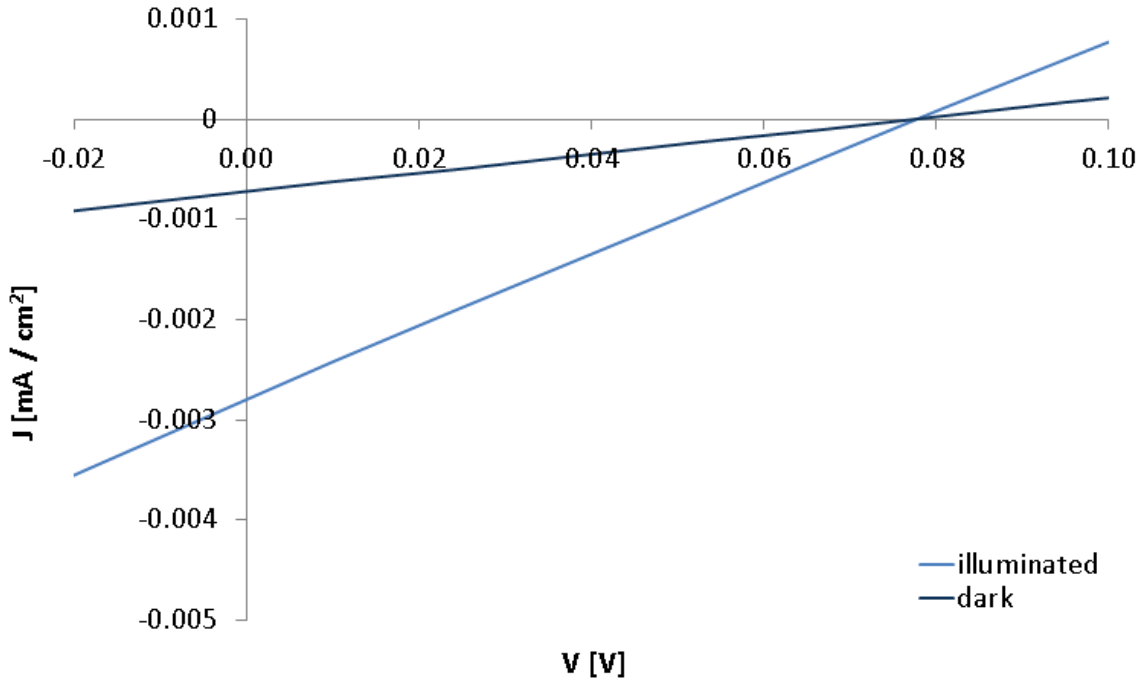

Fig. 54: Current voltage characteristics of a p-n junction between PbO and heat treated PbO_2.

This device configuration shows no rectifying behaviour and only a small photo response. No change in voltage between the dark and the illuminated condition and only very minimal photocurrent can be measured. The reasons for this can be explained through Kelvin probe measurements revealing the relative positions of the Fermi levels (Fig. 55).

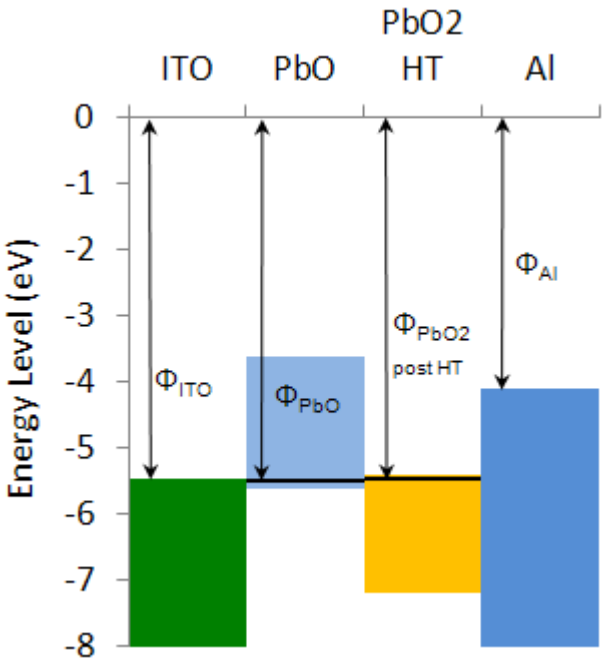

Fig. 55: Sketch of the band diagram of a PbO-PbO_2 p-n junction device according to work functions measured by KP.

Despite the careful processing of the p-type and n-type films, their work functions cannot be changed enough to create a junction between the two materials, but the maximum achievable for the p-type film lines up with the minimum of the n-type film, thereby creating neither a junction nor a barrier. Ohmic contacts are formed between the active layers and their respective neighbouring electrodes. In addition to that, the PbO is very resistive, suggesting a large imbalance of charge carriers between the two materials and therefore it can be expected that the depletion region does not extend very far into the n-type absorber material. The next step is to find a p-type material that works with PbO_2.

5.2.4. P3HT –annealed PbO_2 Junctions

Finding a suitable p-type material to work with sputter coated PbO_2 is something of a challenge because the Fermi level is very low. It was hence decided to use an excitonic system, where light absorbed in the conducting polymer creates bound excitons which migrate to a materials interface where there is a difference in potential sufficient to overcome the excitons intrinsic binding energy [14]. Due to the short diffusion length only excitons generated within ~10 nm of the interface on the polymer side will reach the interface to be dissociated [182]. Contacts with offset work functions are used so that electrons and holes can be selectively collected after the excitons dissociate [14]. Both of these effects were anticipated to result in a low current for simple bi-layer cells and act only as a proof of principle.

P3HT (poly(3-hexylthiophene) is one of the best-performing polymer solar cell materials and considered as a p-type standard for testing new polymer photovoltaic device designs [183-186]. Its HOMO is reported to lie between -4.8 and -5.3 eV, depending on processing conditions [187-190].

A device was made with annealed PbO_2 and P3HT between ITO and Au electrodes. Kelvin probe was used to determine the Fermi levels of the constituent materials as shown in Fig. 56.

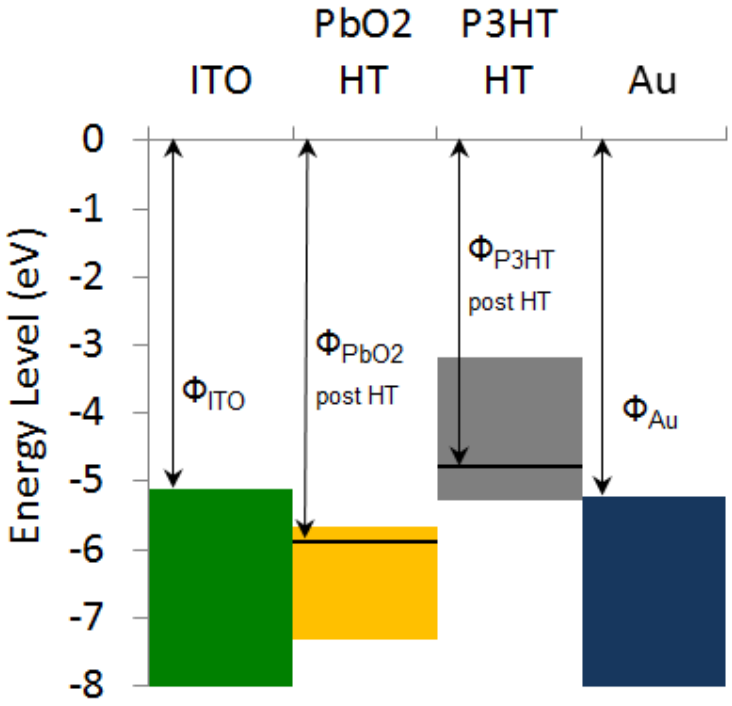

Fig. 56: Sketch of the band positions of ITO, P3HT, heat treated PbO_2 and Au according to work functions measured by KP.

Dietmueller *et al.* [191] have studied the band alignment in a semiconductor-P3HT interface extensively through temperature dependent *JV* characteristics, Kelvin probe and surface photovoltage measurements and report the formation of a depletion region in the semiconductor. Chan *et al.* [192] report the formation of a type II junction between ZnO and P3HT. Based on this it is believed that a type III-like, small barrier forms between the Pb_3O_4 and the P3HT. The large difference in P3HT lowest unoccupied molecular orbital (LUMO) and Pb_3O_4 conduction band (CB) indicates that efficient excitons dissociation could be possible at this interface [193].

In this device design electrons are collected by the ITO and holes by the Au. A sketch of the band diagram for such a device is illustrated in Fig. 57, indicating the direction of the charge carrier flow and the maximum attainable V_{OC}, which depends on the effective electronic band gap of the system [194], which is the difference between the highest occupied molecular orbital (HOMO) of the P3HT and the conduction band of the Pb_3O_4. Literature values were used to estimate the position of the HOMO and LUMO of P3HT [195-197].

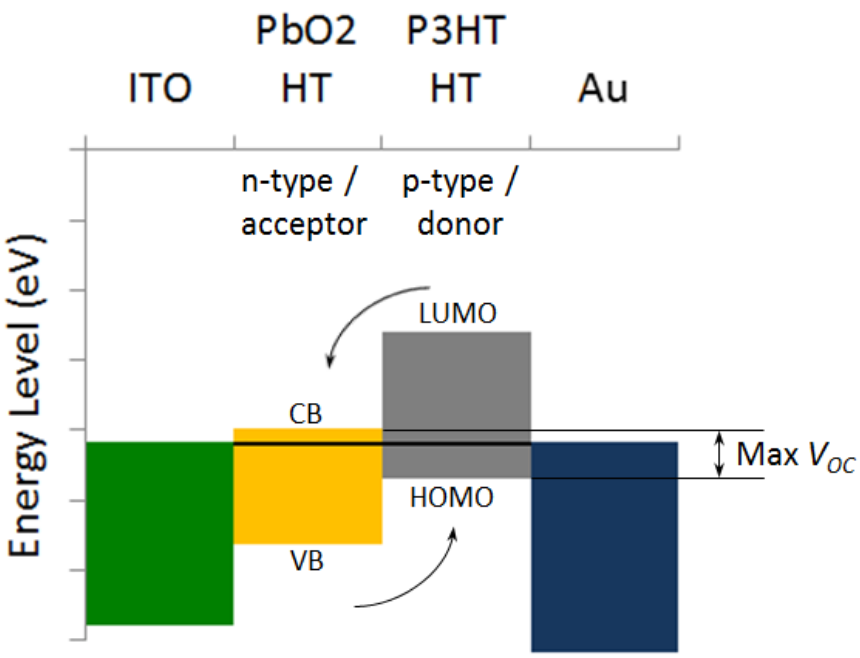

Fig. 57: Band diagram of the materials in contact, indicating the direction of charge flow and the maximum attainable V_{OC}.

JV curves for P3HT – annealed PbO_2 devices are shown in Fig. 58 for devices before and after a heat treatment performed on P3HT.

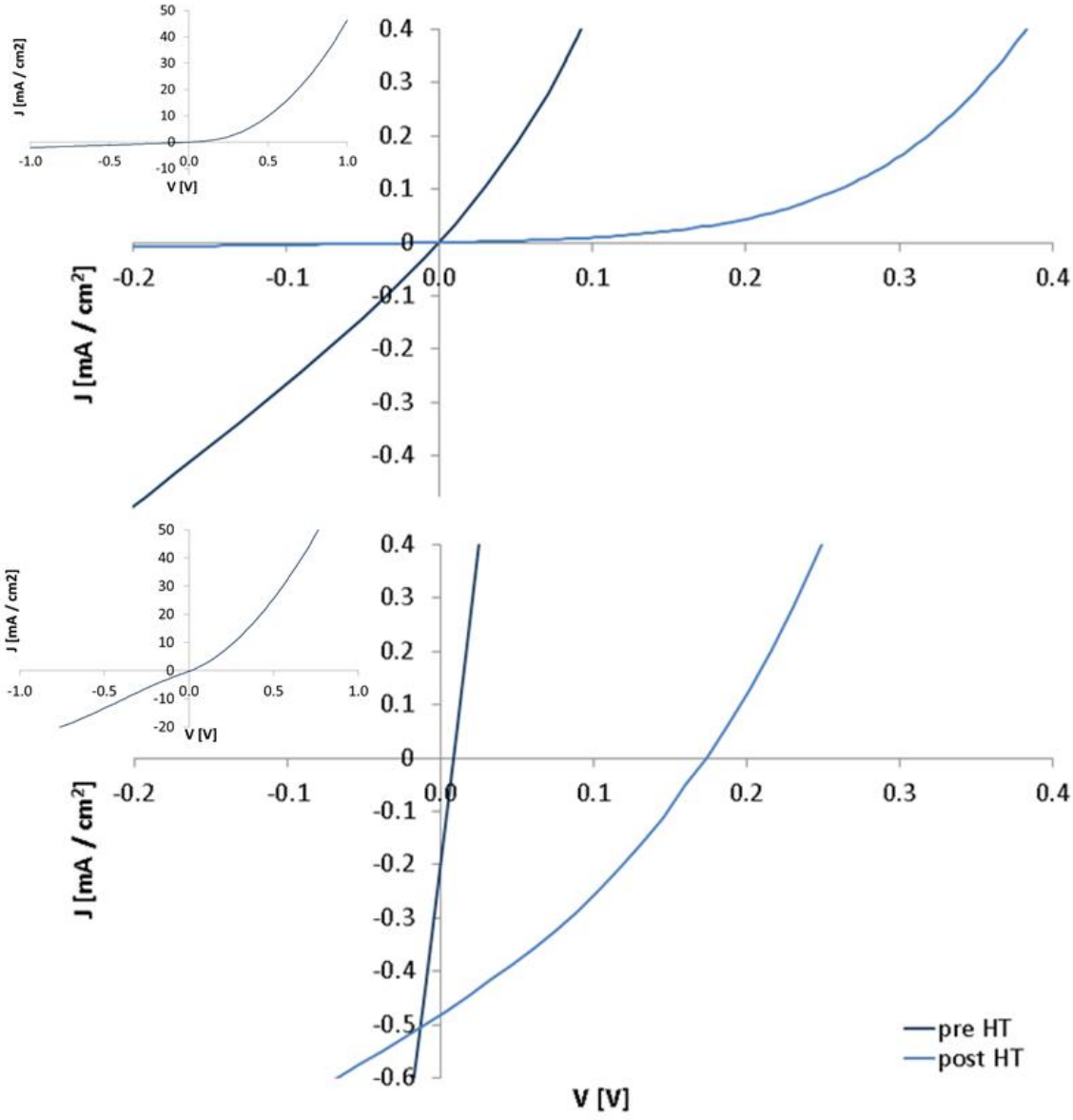

Fig. 58: JV characteristics of P3HT-heat treated PbO_2 junctions in the dark (top) and under illumination (bottom), pre and post P3HT annealing. The inserts show a zoom of the curves before P3HT heat treatment in the dark (top) and under illumination (bottom).

It is well-known that an anneal at 150°C on P3HT allows the material to crystallize into a lamellar structure, increasing mobility and conductivity of the material [198-200]. It is clear that without this anneal step there is next-to-no photovoltage observed even though a rectifying diode is made and a photocurrent produced upon illumination. Upon annealing, the device shows more pronounced rectification in the dark, giving evidence of improved parasitic resistances and a significant decrease in dark current J_0 from 0.097 mA/cm^2 to 0.0097 mA/cm^2. Under illumination a photovoltage is generated, V_{OC} is 0.18 V, and J_{SC} increases from 0.2 mA/cm^2 to almost 0.5 mA/cm^2 after annealing. The increase in J_{SC} is driven by the improved electronic properties of P3HT, the dark current J_0 decreases by an order of magnitude. To try and explain the change in V_{OC}, Kelvin probe measurements of the P3HT were performed which showed a change in work function of 0.1 ± 0.01 eV on annealing. This increases the built-in bias and the maximum attainable V_{OC}, and decreases the barrier; however this is unlikely to be the sole cause of the improved efficiency as it is too small a change. Reduced current leakage could be another reason as evidenced by the decrease in dark current.

Here Kelvin probe correctly predicted that an inverted structure would be made and delivers an explanation for the increase of V_{OC} after P3HT anneal.

5.3. Conclusions

Different stoichiometries of lead oxides were used as the absorber layer in photovoltaic devices. A mixture of orthorhombic and tetragonal PbO, oxidised from evaporated lead, in a Schottky junction shows the best performance. These devices were limited by their poor electronic properties and non-ideal band gap of 2.2-2.4 eV. In an attempt to improve properties a hydrogen anneal step to passivate grain boundaries was used with some success, device efficiency was improved by a factor of two. Sputter coating was then used to make a different stoichiometry (PbO_2). This was found to be a degenerate semiconductor with no photoactive behaviour. Thermal annealing was used to modify its stoichiometry and hence electronic properties in an attempt to make it a useful PV junction material. Unfortunately it showed a very high work function, making it difficult to find a p-type material with which to create a p-n junction. A device based upon a junction with a conducting polymer was produced with some success.

Kelvin probe is shown to be a useful tool for predicting the feasibility of new device designs, giving information about carrier flow direction in the device and attainable V_{OC} and can be used to determine work function changes induced by different processing.

6. Conclusions and Outlook

The primary objective of this thesis was to investigate lead oxides as photovoltaic materials. Vacuum deposition methods and *ex-situ* annealing were used to produce different stoichiometries of lead oxide. The relationship between structure and the optoelectronic properties was then investigated. Following this, a number of photovoltaic devices were prototyped and Kelvin probe used to determine and understand the band structure of devices.

Evaporated Films

Thin films of PbO were produced via air annealing of thermally evaporated films of lead. The two PbO phases, tetragonal and orthorhombic, were found to co-exist and compete with each other. It was found that the relative ratio of the two stoichiometries depends on the duration of the thin film heat treatment. The orthorhombic phase forms predominantly in the early stages of the anneal and the tetragonal oxide is formed as oxidation proceeds. If samples continue to be annealed the phase reverts back to orthorhombic as the anneal energy is used

in the phase transformation. It was concluded that this was due to the very similar structure of the two phases and the low activation energy for transformation.

The content of each oxide in the film determines the materials properties and the behaviour as a photoactive film in a solar device. A higher tetragonal content lead to better device performance because of its improved conductivity and more suitable band gap. Kelvin probe measurements revealed an increase in work function with increasing anneal duration. This goes along with a decrease in series resistance in devices after longer heat treatments and higher PbO_{tet} content. This trend continues up to 40 hours, where grain growth of the orthorhombic phase takes place at the expense of PbO_{tet} and the series resistance increases. At the same time a crossover of the PbO and ITO work functions occurs and a secondary junction is formed at the front contact which is opposed to the main PbO-Al Schottky junction. At this point a maximum V_{OC} and J_{SC} are achieved, resulting in a PCE of about 0.17 %. V_{OC} as well as J_{SC} decrease for longer heat treatments. The combination of KP measurements and *JV* curves reveals that the PbO is p-type, which, due to its high resistivity, is not measureable with Hall Effect.

The high V_{OC} is explained by the relative positions of the Fermi levels of the two materials forming the Schottky junction, revealed by Kelvin probe measurements. Limitations of this material are the poor conductivity and a non-ideal band gap of 2.2 – 2.4 eV. Grain boundary passivation via a hydrogen anneal showed some improvement in PCE that is related to an increased J_{SC} as a result of slight grain growth and a decrease in recombination measured as dark current J_0.

Sputtered Films

Reactive sputtering of lead resulted in the formation of PbO at very low oxygen flow rates and PbO_2 at higher flow rates. With increasing oxygen flow rate of the sputtering process the resistivity increases which could be related to decreasing mobility, arising from a decrease in grain size. This goes alongside increasing carrier concentration as the material gets less ordered, resulting in a decrease of the work function as energy bands get filled up. However work functions were unusually high between -5.6 and -5.8 eV for all sputtered films. Devices made with this material showed no rectification and no photo-response. Despite its nearly ideal band gap for single junction solar cells of 1.6 eV PbO_2 is a highly conductive degenerate n-type semiconductor and hence not photoactive. In addition to that its high work function between -5.6 and -5.8 eV means that it does not form a junction with a metal electrode. Pt is known for its high work function but only a value of -5.5 eV could be reached with sputtered Pt, which is still too low to form a junction with PbO_2.

In order to produce oxides of intermediate stoichiometry that show electronic properties more suitable for the application in solar cells, post-deposition annealing was performed on the sputtered films. This resulted in a transformation to Pb_3O_4, which is less conductive with lower carrier concentration and mobility and hence shows more promise for applications as a light absorber, although work function values were similarly high and the band gap is slightly increased from 1.6 eV to about 2 eV. Promising reports on metal oxide n+:n junctions motivated the fabrication of such structures with PbO_2 before and after a post-annealing step,

however the change in electronic properties was not pronounced enough to create a useful junction.

An attempt was made to make a PbO-PbO_2 p-n junction, as these devices could potentially be made in a one-step process. These structures however did not show rectification and only minimal current flow under illumination. Kelvin probe results explain this observation as even through skilled processing the Fermi levels of the two materials cannot be pushed far enough apart to create a potential big enough to drive a current through the device.

Heterojunctions between P3HT and Pb_3O_4 were made that verify the predictions made based on KP measurements. A heat treatment on P3HT improved its electronic properties and raised the Fermi level, resulting in a higher V_{OC} and J_{SC}, and a decrease in J_0.

Kelvin Probe as a Tool for Solar Cell Design

KP was demonstrated as a quick and useful tool for the development and understanding of photovoltaic junctions, explaining changes in V_{OC} under varying processing conditions and giving information about the viability of materials combinations without the need to fabricate devices. KP gives a good indication of how different materials energy levels will align and in combination with other techniques such as the Hall measurement to measure carrier concentration and type can be used to predict what will make a viable photovoltaic device.

In the case of the PbO-Al Schottly junctions KP helped to understand the changes in V_{OC} upon annealing and explained the inherent limitations of this materials combination for a solar device. The Fermi level of PbO drops with annealing and an opposed junction forms in the device at the cross-over of the Fermi levels of PbO and ITO, which limits V_{OC}.

In the devices made between different stoichiometries of lead oxides KP reveals that due to the Fermi levels of the materials lying too closely together, the built-in bias resulting from charge exchange at the junction is not strong enough to drive a current and the devices are not rectifying.

In an exitonic system it was shown that KP accurately predicts the direction of current flow and improvements in V_{OC} with changing position of the Fermi level of one of the junction materials.

Future Work

Low J_{SC} is the limiting factor for evaporated lead oxide Schottky junctions and a path to improving conductivity could be the fabrication of larger grain films, either via heat treatments or possibly reactive evaporation of PbO onto heated substrates. Additional doping of the films is another alternative to improve conductivity. Mittiga *et al.* [201] show that the introduction of a hole blocking layer in a Cu_2O cell doubles its efficiency as most charge carriers are generated near the TCO interface and a ZnO layer creates a barrier for holes, and hence prevents recombination at the contact [47]. This could be another path forward for increased PCE in PbO Schottky junctions.

In addition to the very high conductivity, PbO_2 shows visually observable colour changes upon heat treatments that go from brown to yellow to white, each time increasing the material's transparency. This makes it a candidate to be used as a transparent conductive oxide (TCO). Conductivities of PbO_2 approach those of ITO and first principles calculations carried out by Walsh *et al.* [166] show that a decrease in the number of charge carriers would prevent intra band transitions below 3 eV hence making the material optically transparent. Our experiments show a lot of promise for this to be attainable through simple annealing treatments.

References

[1] M. Asif, T. Muneer, Energy supply, its demand and security issues for developed and emerging economies, Renewable and Sustainable Energy Reviews, 11 (2007) 1388-1413.

[2] R. Gross, M. Leach, A. Bauen, Progress in renewable energy, Environment International, 29 (2003) 105-122.

[3] B.J.M. de Vries, D.P. van Vuuren, M.M. Hoogwijk, Renewable energy sources: Their global potential for the first-half of the 21st century at a global level: An integrated approach, Energy Policy, 35 (2007) 2590-2610.

[4] K. Branker, M.J.M. Pathak, J.M. Pearce, A review of solar photovoltaic levelized cost of electricity, Renewable and Sustainable Energy Reviews, 15 (2011) 4470-4482.

[5] A. Slaoui, R.T. Collins, Photovoltaics: advanced inorganic materials, Encyclopedia of Materials: Science and Technology, (2008) 1-11.

[6] D.M. Bagnall, M. Boreland, Photovoltaic technologies, Energy Policy, 36 (2008) 4390-4396.

[7] K.L. Chopra, P.D. Paulson, V. Dutta, Thin-film solar cells: An overview, Progress in Photovoltaics: Research and Applications, 12 (2004) 69-92.

[8] A. Jäger-Waldau, Thin film photovoltaics: Markets and industry, International Journal of Photoenergy, 2012 (2012).

[9] T. Surek, Crystal growth and materials research in photovoltaics: Progress and challenges, Journal of Crystal Growth, 275 (2005) 292-304.

[10] R.W. Birkmire, E. Eser, Polycrystalline thin film solar cells: Present status and future potential, Annual Review of Materials Science, 27 (1997) 625-653.

[11] H.W. Schock, R. Noufi, CIGS-based solar cells for the next millennium, Progress in Photovoltaics: Research and Applications, 8 (2000) 151-160.

[12] A.W. Czanderna, Stability of interfaces in solar energy materials, Solar Energy Materials, 5 (1981) 349-377.

[13] K. Kushiya, Y. Tanaka, H. Hakuma, Y. Goushi, S. Kijima, T. Aramoto, Y. Fujiwara, Interface control to enhance the fill factor over 0.70 in a large-area CIS-based thin-film PV technology, Thin Solid Films, 517 (2009) 2108-2110.

[14] J. Nelson, The physics of solar cells, Imperial College Press, (2003).

[15] C. Wadia, A.P. Alivisatos, D.M. Kammen, Materials availability expands the opportunity for large-scale photovoltaics deployment, Environmental Science and Technology, 43 (2009) 2072-2077.

[16] B.A. Andersson, Materials availability for large-scale thin-film photovoltaics, Progress in Photovoltaics: Research and Applications, 8 (2000) 61-76.

[17] B.A. Andersson, C. Azar, J. Holmberg, S. Karlsson, Material constraints for thin-film solar cells, Energy, 23 (1998) 407-411.

[18] J.D. Jorgenson, M.W. George, Mineral commodity profile indium, USGS Open-File Report, 1300 (2004).

[19] M.A. Green, K. Emery, Y. Hishikawa, W. Warta, Solar cell efficiency tables (version 34), Progress in Photovoltaics: Research and Applications, 17 (2009) 320-326.

[20] M.A. Contreras, B. Egaas, K. Ramanathan, J. Hiltner, A. Swartzlander, F. Hasoon, R. Noufi, Progress toward 20% efficiency in Cu(In,Ga)Se2 polycrystalline thin-film solar cells, Progress in Photovoltaics: Research and Applications, 7 (1999) 311-316.

[21] T. Aramoto, S. Kumazawa, H. Higuchi, T. Arita, S. Shibutani, T. Nishio, J. Nakajima, M. Tsuji, A. Hanafusa, T. Hibino, K. Omura, H. Ohyama, M. Murozono, 16.0% efficient thin-film CdS/CdTe solar cells, Japanese Journal of Applied Physics, Part 1: Regular Papers and Short Notes and Review Papers, 36 (1997) 6304-6305.

[22] T.L. Chu, S.S. Chu, C. Ferekides, C.Q. Wu, J. Britt, C. Wang, 13.4% efficient thin-film CdS/CdTe solar cells, Journal of Applied Physics, 70 (1991) 7608-7612.

[23] C.S. Ferekides, D. Marinskiy, V. Viswanathan, B. Tetali, V. Palekis, P. Selvaraj, D.L. Morel, High efficiency CSS CdTe solar cells, Thin Solid Films, 361 (2000) 520-526.

[24] T. Wada, Y. Matsuo, S. Nomura, Y. Nakamura, A. Miyamura, Y. Chiba, A. Yamada, M. Konagai, Fabrication of Cu(In,Ga)Se 2thin films by a combination of mechanochemical and screen-printing/sintering processes, Physica Status Solidi (A) Applications and Materials Science, 203 (2006) 2593-2597.

[25] F.J. Pern, J. Goral, R.J. Matson, T.A. Gessert, R. Noufi, Device quality thin films of CuInSe2 by a one-step electrodeposition process, Solar Cells, 24 (1988) 81-90.

[26] C.J. Hibberd, E. Chassaing, W. Liu, D.B. Mitzi, D. Lincot, A.N. Tiwari, Non-vacuum methods for formation of Cu(In, Ga)(Se, S)2 thin film photovoltaic absorbers, Progress in Photovoltaics: Research and Applications, 18 (2010) 434-452.

[27] D. Perednis, L.J. Gauckler, Thin film deposition using spray pyrolysis, Journal of Electroceramics, 14 (2005) 103-111.

[28] H. Neumann, R.D. Tomlinson, Relation between electrical properties and composition in CuInSe2 single crystals, Solar Cells, 28 (1990) 301-313.

[29] R.D. Tomlinson, Fabrication of CuInSe2 single crystals using melt-growth techniques, Solar Cells, 16 (1986) 17-26.

[30] B.M. Basol, V.K. Kapur, C.R. Leidholm, A. Minnick, A. Halani, Studies on substrates and contacts for CIS films and devices, in: Anon (Ed.) Conference Record of the IEEE Photovoltaic Specialists Conference, IEEE, Waikoloa, HI, USA, 1994, pp. 148-151.

[31] D. Braunger, D. Hariskos, G. Bilger, U. Rau, H.W. Schock, Influence of sodium on the growth of polycrystalline Cu(In,Ga)Se2 thin films, Thin Solid Films, 361-362 (2000) 161-166.

[32] M.A. Contreras, K. Ramanathan, J. Abushama, F. Hasoon, D.L. Young, B. Egaas, R. Noufi, Diode characteristics in state-of-the-art ZnO/CdS/ Cu(In 1-xGax)Se2 solar cells, Progress in Photovoltaics: Research and Applications, 13 (2005) 209-216.

[33] M. Bär, I. Repins, M.A. Contreras, L. Weinhardt, R. Noufi, C. Heske, Chemical and electronic surface structure of 20%-efficient Cu (In,Ga) Se2 thin film solar cell absorbers, Applied Physics Letters, 95 (2009).

[34] J. Britt, C. Ferekides, Thin-film CdS/CdTe solar cell with 15.8% efficiency, Applied Physics Letters, 62 (1993) 2851-2852.

[35] X. Wu, J.C. Keane, R.G. Dhere, C. DeHart, A. Duda, T.A. Gessert, S. Asher, D.H. Levi, P. Sheldon, 16.5%-efficient CdS/CdTe polycrystalline thin-film solar cell, Conference Proceedings, 17th European Photovoltaic Solar Energy Conference Munich, 22-26 (2001) 995-1000.

[36] I.M. Dharmadasa, Latest developments in CdTe, CuInGaSe2 and GaAs/AlGaAs thin film PV solar cells, Current Applied Physics, 9 (2009).

[37] D.B. Mitzi, O. Gunawan, T.K. Todorov, K. Wang, S. Guha, The path towards a high-performance solution-processed kesterite solar cell, Solar Energy Materials and Solar Cells, 95 (2011) 1421-1436.

[38] N.H. Nickel, N.M. Johnson, W.B. Jackson, Hydrogen passivation of grain boundary defects in polycrystalline silicon thin films, Applied Physics Letters, 62 (1993) 3285-3287.

[39] H.C. Cheng, F.S. Wang, C.Y. Huang, Effects of NHs plasma passivation on n-channel polycrystalline silicon thin-film transistors, IEEE Transactions on Electron Devices, 44 (1997) 64-68.

[40] H. Katagiri, K. Jimbo, S. Yamada, T. Kamimura, W.S. Maw, T. Fukano, T. Ito, T. Motohiro, Enhanced conversion efficiencies of Cu2ZnSnS4-based thin film solar cells by using preferential etching technique, Applied Physics Express, 1 (2008) 0412011-0412012.

[41] G. Halek, I.D. Baikie, H. Teterycz, P. Halek, P. Suchorska-Woźniak, K. Wiśniewski, Work function analysis of gas sensitive WO3 layers with Pt doping, Sensors and Actuators, B: Chemical, (2013).

[42] Y.D. Park, J.H. Cho, D.H. Kim, Y.L. Jang, H.S., K. Ihm, T.-H. Kang, K. Cho, Energy-Level Alignment at Interfaces Between Gold and Poly(3-hexylthiophene) Films with Two Different Molecular Structures, Electrochemical and Solid-State Letters, 9 (2006) G317-G319.

[43] W. Shockley, H.J. Queisser, Detailed Balance Limit of Efficiency of p-n Junction Solar Cells, Journal of Applied Physics, 32 (1960) 510-519.

[44] S. Ishizuka, S. Kato, Y. Okamoto, K. Akimoto, Hydrogen treatment for polycrystalline nitrogen-doped Cu2O thin film, Journal of Crystal Growth, 237–239, Part 1 (2002) 616-620.

[45] W. Zhang, Y. Chen, Experimental determination of conduction and valence bands of semiconductor nanoparticles using Kelvin probe force microscopy, Journal of Nanoparticle Research, 15 (2013).

[46] I. Hancox, L.A. Rochford, D. Clare, M. Walker, J.J. Mudd, P. Sullivan, S. Schumann, C.F. McConville, T.S. Jones, Optimization of a high work function solution processed vanadium oxide hole-extracting layer for small molecule and polymer organic photovoltaic cells, Journal of Physical Chemistry C, 117 (2013) 49-57.

[47] S. Rühle, A.Y. Anderson, H.N. Barad, B. Kupfer, Y. Bouhadana, E. Rosh-Hodesh, A. Zaban, All-oxide photovoltaics, Journal of Physical Chemistry Letters, 3 (2012) 3755-3764.

[48] M.J. Lee, J. Lim, J. Bang, W. Lee, J.M. Myoung, Effect of the thickness and hydrogen treatment on the properties of Ga-doped ZnO transparent conductive films, Applied Surface Science, 255 (2008) 3195-3200.

[49] N. Guijarro, T. Lutz, T. Lana-Villarreal, F. O'Mahony, R. Gómez, S.A. Haque, Toward antimony selenide sensitized solar cells: Efficient charge photogeneration at spiro - OMeTAD/Sb 2Se 3/metal oxide heterojunctions, Journal of Physical Chemistry Letters, 3 (2012) 1351-1356.

[50] R. Jose, V. Thavasi, S. Ramakrishna, Metal oxides for dye-sensitized solar cells, Journal of the American Ceramic Society, 92 (2009) 289-301.

[51] P.V. Kamat, TiO 2 nanostructures: Recent physical chemistry advances, Journal of Physical Chemistry C, 116 (2012) 11849-11851.

[52] J.A. Anta, E. Guillén, R. Tena-Zaera, ZnO-based dye-sensitized solar cells, Journal of Physical Chemistry C, 116 (2012) 11413-11425.

[53] S. Ferrere, A. Zaban, B.A. Gregg, Dye sensitization of nanocrystalline tin oxide by perylene derivatives, Journal of Physical Chemistry B, 101 (1997) 4490-4493.

[54] S. Burnside, J.E. Moser, K. Brooks, M. Grätzel, D. Cahen, Nanocrystalline mesoporous strontium titanate as photoelectrode material for photosensitized solar devices: Increasing photovoltage through flatband potential engineering, Journal of Physical Chemistry B, 103 (1999) 9328-9332.

[55] F. Lenzmann, J. Krueger, S. Burnside, K. Brooks, M. Grätzel, D. Gal, S. Rühle, D. Cahen, Surface photovoltage spectroscopy of dye-sensitized solar cells with TiO2, Nb2O5, and SrTiO3 nanocrystalline photoanodes: Indication for electron injection from higher excited dye states, Journal of Physical Chemistry B, 105 (2001) 6347-6352.

[56] S. Greenwald, S. Rühle, M. Shalom, S. Yahav, A. Zaban, Unpredicted electron injection in CdS/CdSe quantum dot sensitized ZrO 2 solar cells, Physical Chemistry Chemical Physics, 13 (2011) 19302-19306.

[57] B.D. Chernomordik, U. Cvelbar, V. Chakrapani, M. Mozetic, M.K. Sunkara, α-Fe2O3 nanowire array based electrodes for self-driven photoelectrochemical cells, in, Philadelphia, PA, 2008.

[58] R. Shinar, J.H. Kennedy, Photoactivity of doped αFe2O3 electrodes, Solar Energy Materials, 6 (1982) 323-335.

[59] S.S. Shinde, R.A. Bansode, C.H. Bhosale, K.Y. Rajpure, Physical properties of hematite α-Fe2O3 thin films: Application to photoelectrochemical solar cells, Journal of Semiconductors, 32 (2011).

[60] T. Choi, S. Lee, Y.J. Choi, V. Kiryukhin, S.W. Cheong, Switchable ferroelectric diode and photovoltaic effect in BiFeO3, Science, 324 (2009) 63-66.

[61] J. Seidel, D. Fu, S.Y. Yang, E. Alarcón-Lladó, J. Wu, R. Ramesh, J.W. Ager, Efficient photovoltaic current generation at ferroelectric domain walls, Physical Review Letters, 107 (2011).

[62] S.Y. Yang, L.W. Martin, S.J. Byrnes, T.E. Conry, S.R. Basu, D. Paran, L. Reichertz, J. Ihlefeld, C. Adamo, A. Melville, Y.H. Chu, C.H. Yang, J.L. Musfeldt, D.G. Schlom, J.W. Ager, R. Ramesh, Photovoltaic effects in BiFeO3, Applied Physics Letters, 95 (2009).

[63] S.Y. Yang, J. Seidel, S.J. Byrnes, P. Shafer, C.H. Yang, M.D. Rossell, P. Yu, Y.H. Chu, J.F. Scott, J.W. Ager, L.W. Martin, R. Ramesh, Above-bandgap voltages from ferroelectric photovoltaic devices, Nature Nanotechnology, 5 (2010) 143-147.

[64] L.C. Olsen, R.C. Bohara, M.W. Urie, Explanation for low-efficiency Cu2O Schottky-barrier solar cells, Applied Physics Letters, 34 (1979) 47-49.

[65] R.J. Iwanowski, D. Trivich, ENHANCEMENT OF THE PHOTOVOLTAIC CONVERSION EFFICIENCY IN Cu/Cu//2O SCHOTTKY BARRIER SOLAR CELLS BY H** plus ION IRRADIATION, Physica Status Solidi (A) Applied Research, 95 (1986) 735-741.

[66] L.C. Olsen, F.W. Addis, W. Miller, Experimental and theoretical studies of Cu2O solar cells, Solar Cells, 7 (1982) 247-279.

[67] J. Herion, E.A. Niekisch, G. Scharl, Investigation of metal oxide/cuprous oxide heterojunction solar cells, Solar Energy Materials, 4 (1980) 101-112.

[68] T. Minami, Y. Nishi, T. Miyata, J.I. Nomoto, High-efficiency oxide solar cells with ZnO/Cu2O heterojunction fabricated on thermally oxidized Cu2O sheets, Applied Physics Express, 4 (2011).

[69] Y. Nishi, T. Miyata, T. Minami, Effect of inserting a thin buffer layer on the efficiency in n-ZnO/p-Cu 2O heterojunction solar cells, Journal of Vacuum Science and Technology A: Vacuum, Surfaces and Films, 30 (2012).

[70] K.P. Musselman, A. Wisnet, D.C. Iza, H.C. Hesse, C. Scheu, J.L. MacManus-Driscoll, L. Schmidt-Mende, Strong efficiency improvements in ultra-low-cost inorganic nanowire solar cells, Advanced Materials, 22 (2010) E254-E258.

[71] K.P. Musselman, A. Marin, L. Schmidt-Mende, J.L. MacManus-Driscoll, Incompatible length scales in nanostructured Cu 2O solar cells, Advanced Functional Materials, 22 (2012) 2202-2208.

[72] B.Y. Oh, M.C. Jeong, D.S. Kim, W. Lee, J.M. Myoung, Post-annealing of Al-doped ZnO films in hydrogen atmosphere, Journal of Crystal Growth, 281 (2005) 475-480.

[73] S. Darbe, R. Beal, A. Stavrinadis, H. Cao, J. Smith, H.A. Assender, A.A.R. Watt, Visible light absorbing metal oxide solar cells, MIT-Oxford summer student report, (2009).

[74] S. Venkataraj, O. Kappertz, R. Drese, C. Liesch, R. Jayavel, M. Wuttig, Thermal stability of lead oxide films prepared by reactive DC magnetron sputtering, Physica Status Solidi (A) Applied Research, 194 (2002) 192-205.

[75] F.A. Cotton, G. Wilkinson, Advanced Inorganic Chemistry, Fifth Edition, John Wiley & Sons, Inc., (1988).

[76] A. Earnshaw, N. Greenwood, Chemistry of the Elements, Second Edition, Butterworth-Heinemann, (2002).

[77] H. Wriedt, A., The O-Pb (Oxygen-Lead) System, Bulletin of Alloy Phase Diagrams, 9 (1988) 106-124.

[78] W. Kwestroo, J. de Jonge, P.H.G.M. Vromans, Influence of impurities on the formation of red and yellow PbO, Journal of Inorganic and Nuclear Chemistry, 29 (1967) 39-44.

[79] W.B. White, F. Dachille, R. Roy, High-pressure - high-temperature polymorphism of the oxides of lead, Journal of the American Ceramic Society, 44 (1961) 170-174.

[80] W.B. White, R. Roy, Phase relations in the system lead-oxygen, Journal of the American Ceramic Society, 47 (1964) 242-249.

[81] H.J. Terpstra, R.A. De Groot, C. Haas, The electronic structure of the mixed valence compound Pb3O4, Journal of Physics and Chemistry of Solids, 58 (1997) 561-566.

[82] W.L. Bragg, J.A. Darbyshire, The structure of thin films of certain metallic oxides., Transactions of the Faraday Society, 28 (1932) 522-529.

[83] W. Mindt, Electrical properties of electrodeposited PbO2 films, Journal of the Electrochemical Society, 116 (1969) 1076-1080.

[84] J.T. McCloskey, M.C. Newman, S.B. Clark, Predicting the relative toxicity of metal ions using ion characteristics: microtox bioluminescence assay, Environ. Toxic. Chem., 15 (1996) 1730-1737.

[85] D. Pavlov, Semiconductor mechanism of the processes during electrochemical oxidation of PbO to PbO2, Journal of Electroanalytical Chemistry, 118 (1981) 167-185.

[86] I. Mukhopadhyay, M.S.S. Raghavan, M. Sharon, H. Minoura, P. Veluchamy, Photoelectrochemical studies of photoactive lead oxide prepared by the "Potential pulse coupled potentiodynamic anodization technique" in alkaline medium, Journal of Electroanalytical Chemistry, 379 (1994) 531-534.

[87] I. Mukhopadhyay, S. Ghosh, M. Sharon, Surface modification by potential delay to obtain a photoactive PbO film, Materials and Manufacturing Processes, 12 (1997) 925-933.

[88] S. Radhakrishnan, M.N. Kamalasanan, P.C. Mehendru, Sensitization of photoconductivity in tetragonal lead monoxide, Journal of Materials Science, 18 (1983) 1912-1916.

[89] G. Trinquier, R. Hoffmann, Lead monoxide. Electronic structure and bonding, Journal of Physical Chemistry, 88 (1984) 6696-6711.

[90] K.L. Keester, W.B. White, Electronic spectra of the oxides of lead and of some ternary lead oxide compounds, Materials Research Bulletin, 4 (1969) 757-764.

[91] F. Lappe, Some physical properties of sputtered PbO2 films, Journal of Physics and Chemistry of Solids, 23 (1962) 1563-1566.

[92] P. Ruetschi, B.D. Cahan, Electrochemical Properties of PbO2 and the Anodic Corrosion of Lead and Lead Alloys, Journal of the Electrochemical Society, 105 (1958) 369-377.

[93] H.J. Schuster, Messung des elektrischen Widerstandes von pulverformigen Bleioxyden, Chemie Ingenieur Technik, 28 (1956) 654-655.

[94] S. Kumar, M. Sharon, S.R. Jawalekar, Preparation of a thin film of Pb3O4 by thermal treatment of PbO2 film, Thin Solid Films, 195 (1991) 273-278.

[95] K.L. Chopra, Thin Film Phenomena, McGraw-Hill, New York, (1969).

[96] M. Bader, F. Witteborn, T.W. Snouse, Sputtering of metals by mass-analyzed N2+ and N+, NASA Technical Report R-105, (1961).

[97] M. Kaminsky, Sputtering experiments in the rutherford collision region, Physical Review, 126 (1962) 1267-1270.

[98] J. Comas, C.B. Cooper, Mass-spectrometric study of sputtering of single crystals of GaAs by low-energy a ions, Journal of Applied Physics, 38 (1967) 2956-2960.

[99] E.E. Smith, S.G. Ayling, Sputtered dielectric capacitors, Proceedings Electronic Components Confrence, Washington, USA (1962) 82.

[100] E. Krikorian, R.J. Sneed, Epitaxial deposition of germanium by both sputtering and evaporation, Journal of Applied Physics, 37 (1966) 3665-3673.

[101] J.W. Bradley, The plasma properties adjacent to the target in a magnetron sputtering source, Plasma Sources Science and Technology, 5 (1996) 622-631.

[102] P.J. Kelly, R.D. Arnell, Magnetron sputtering: A review of recent developments and applications, Vacuum, 56 (2000) 159-172.

[103] T. Minami, H. Sato, H. Nanto, S. Takata, Group III impurity doped zinc oxide thin films prepared by rf magnetron sputtering, Japanese Journal of Applied Physics, Part 2: Letters, 24 (1985) 781-784.

[104] H. Nanto, T. Minami, S. Shooji, S. Takata, Electrical and optical properties of zinc oxide thin films prepared by rf magnetron sputtering for transparent electrode applications, Journal of Applied Physics, 55 (1984) 1029-1034.

[105] K. Tominaga, T. Yuasa, M. Kume, O. Tada, Influence of energetic oxygen bombardment on conductive ZnO films, Japanese Journal of Applied Physics, Part 1: Regular Papers & Short Notes, 24 (1985) 944-949.

[106] J.B. Webb, Conductivity imaging of the erosion pattern for ZnO prepared by planar R.F. magnetron sputtering, Thin Solid Films, 136 (1986) 135-139.

[107] S.M. Rossnagel, J.J. Cuomo, W. Dickson Westwood, Handbook of plamsa processing technology: Fundamentals, etching, deposition, and surface interaction, Noyes Publications, William Andrew Publishing, LLC (1990).

[108] A. Anders, Physics of arcing, and implications to sputter deposition, Thin Solid Films, 502 (2006) 22-28.

[109] S. Venkataraj, J. Geurts, H. Weis, O. Kappertz, W.K. Njoroge, R. Jayavel, M. Wuttig, Structural and optical properties of thin lead oxide films produced by reactive direct current magnetron sputtering, Journal of Vacuum Science and Technology, Part A: Vacuum, Surfaces and Films, 19 (2001) 2870-2878.

[110] K.S. Kim, X-ray photoelectron spectra of lead oxides, Analytical Chemistry, 45 (1973) 2214-2218.

[111] L.D. Madsen, L. Weaver, Characterization of lead oxide thin films produced by chemical vapor deposition, Journal of the American Ceramic Society, 81 (1998) 988-996.

[112] D.J. Payne, R.G. Egdell, D.S.L. Law, P.A. Glans, T. Learmonth, K.E. Smith, J. Guo, A. Walsh, G.W. Watson, Experimental and theoretical study of the electronic structures of alpha-PbO and beta-PbO2, Journal of Materials Chemistry, 17 (2007) 267-277.

[113] C.H. Henry, Limiting Efficiencies of Ideal Single and Multiple Energy Gap Terrestrial Solar Cells, J. Appl. Phys., 51 (1980).

[114] S. Ngamsinlapasathian, A. Kitiyanan, T. Fujieda, S. Yoshikawa, Effect of substrates on dye-sensitized solar cell performance using nanocrystalline TiO2, in, Los Angeles, CA, 2006, pp. 7-15.

[115] R. Beal, Morphology and Efficiency of Polymer:Fullerene Solar Cells, PhD thesis, Department of Materials, University of Oxford, (2010).

[116] W. Thomson, l.L. Kelvin, Contact electricity of metals, Philosophical Magazine, 46 (1898) 82-120.

[117] W.A. Zisman, A new method of measuring contact potential differences in metals, Review of Scientific Instruments, 3 (1932) 367-370.

[118] D.K. Schroder, Semiconductor Material and Device Characterization, IEEE Press, Wiley-Interscience, (2006) 526.

[119] I.D. Baikie, S. Mackenzie, P.J.Z. Estrup, J.A. Meyer, Noise and the Kelvin method, Review of Scientific Instruments, 62 (1991) 1326-1332.

[120] M. Prutton, Introduction to Surface Physics, Clarendon Press Oxford, (1994) 118.

[121] H.B. Michaelson, The work function of the elements and its periodicity, Journal of Applied Physics, 48 (1977) 4729-4733.

[122] M. Pfeiffer, K. Leo, N. Karl, Fermi level determination in organic thin films by the Kelvin probe method, Journal of Applied Physics, 80 (1996) 6880-6883.

[123] J. Tauc, Optical properties and electronic structure of amorphous Ge and Si, Materials Research Bulletin, 3 (1968) 37-46.

[124] A.L. Patterson, The scherrer formula for X-ray particle size determination, Physical Review, 56 (1939) 978-982.

[125] F.W. Jones, Particle size measurement by the x-ray method, Journal of Scientific Instruments, 18 (1941) 157-158.

[126] P. Scherrer, Bestimmung der Grosse und der inneren Struktur von Kolloidteilchen mittels Rontgenstrahlen, Nachrichten von der Gesellschaft der Wissenschaften zu Gottingen, (1918).

[127] A.L. Patterson, The diffraction of X-rays by small crystalline particles, Physical Review, 56 (1939) 972-977.

[128] L.S. Birks, H. Friedman, Particle size determination from x-ray line broadening, Journal of Applied Physics, 17 (1946) 687-692.

[129] O. Hwang, S. Kim, J. Suh, S. Cho, K. Kim, J. Hong, S. Kim, Effect of thermal annealing of lead oxide film, Nuclear Instruments and Methods in Physics Research, Section A: Accelerators, Spectrometers, Detectors and Associated Equipment, 633 (2011) 569-571.

[130] J.C. Schottmiller, Photoconductivity in tetragonal and orthorhombic lead monoxide layers, Journal of Applied Physics, 37 (1966) 3505-3510.

[131] J.R. Anderson, V.B. Tare, Reaction of oxygen with evaporated films of lead, Journal of Physical Chemistry, 68 (1964) 1482-1489.

[132] J.M. Eldridge, D.W. Dong, The growth of thin PbO layers on lead films. I. Experiment, Surface Science, 40 (1973) 512-530.

[133] T.B. Light, J.M. Eldridge, J.W. Matthews, J.H. Greiner, Structure of thin lead oxide layers as determined by x-ray diffraction, Journal of Applied Physics, 46 (1975) 1489-1492.

[134] M.I. Baleva, L.N. Bozukov, V.D. Tuncheva, Crystal structure and growth mechanism of lead monoxide thin films produced by pulsed laser deposition, Journal of Physical Chemistry, 98 (1994) 13308-13313.

[135] D.U. Wiechert, S.P. Grabowski, M. Simon, Raman spectroscopic investigation of evaporated PbO layers, Thin Solid Films, 484 (2005) 73-82.

[136] S.B. Brody, M.P. Seitelman, X-ray study of tetragonal PbO electrolytically deposited on rolled Pb substrate, Journal of Applied Crystallography, 4 (1971) 376-379.

[137] M.F. Tompsett, J.S. Noble, In situ scanning high-energy electron diffraction studies of evaporated lead monoxide films, Thin Solid Films, 5 (1970) 81-96.

[138] M.I. Kay, A neutron diffraction study of orthorhombic PbO, Acta Crystallographica, 14 (1961) 80-81.

[139] J.M. Raulot, G. Baldinozzi, R. Seshadri, P. Cortona, An ab-initio study of the rôle of lone pairs in the structure and insulator-metal transition in SnO and PbO, Solid State Sciences, 4 (2002) 467-474.

[140] R. Söderquist, B. Dickens, Studies in solid state chemistry-I. On a solid-state mechanism for the polymorphic transformation of orthorhombic to tetragonal PbO, Journal of Physics and Chemistry of Solids, 28 (1967) 823-826,IN823-IN824,827.

[141] R.C. Keezer, D.L. Bowman, J.H. Becker, Electrical and optical properties of lead oxide single crystals, Journal of Applied Physics, 39 (1968) 2062-2066.

[142] J.M. Eldridge, The growth of thin PbO layers on lead films. II. Theory, Surface Science, 40 (1973) 531-544.

[143] L. Heyne, N.M. Beekmans, A. de Beer, Ionic conduction and oxygen diffusion in yellow lead oxide., Journal of the Electrochemical Society, 119 (1972) 77-84.

[144] Y.R. Ma, Study of the oxygen-sensitive behavior of yellow lead oxide by defect chemistry, Journal of Applied Physics, 76 (1994) 2860-2862.

[145] T. Minami, New n-type transparent conducting oxides, MRS Bulletin, 25 (2000) 38-44.

[146] Y. Sato, T. Ashida, N. Oka, Y. Shigesato, Carrier density dependence of optical band gap and work function in Sn-doped In2O3 films, Applied Physics Express, 3 (2010).

[147] X. Yong, M.A.A. Schoonen, The absolute energy positions of conduction and valence bands of selected semiconducting minerals, American Mineralogist, 85 (2000) 543-556.

[148] H.P. Myers, Introductory Solid State Physics, Taylor & Francis, Secon Edition (1997).

[149] W.D. Sproul, D.J. Christie, D.C. Carter, Control of reactive sputtering processes, Thin Solid Films, 491 (2005) 1-17.

[150] S. Berg, T. Larsson, C. Nender, H.O. Blom, Predicting thin-film stoichiometry in reactive sputtering, Journal of Applied Physics, 63 (1988) 887-891.

[151] S. Berg, T. Nyberg, Fundamental understanding and modeling of reactive sputtering processes, Thin Solid Films, 476 (2005) 215-230.

[152] T. Nyberg, S. Berg, U. Helmersson, K. Hartig, Eliminating the hysteresis effect for reactive sputtering processes, Applied Physics Letters, 86 (2005) 1-3.

[153] Y. Pauleau, E. Harry, Reactive sputter-deposition and characterization of lead oxide films, Journal of Vacuum Science and Technology A: Vacuum, Surfaces and Films, 14 (1996) 2207-2214.

[154] S. Calnan, J. Hüpkes, B. Rech, H. Siekmann, A.N. Tiwari, High deposition rate aluminium-doped zinc oxide films with highly efficient light trapping for silicon thin film solar cells, Thin Solid Films, 516 (2008) 1242-1248.

[155] D. Horwat, A. Billard, Effects of substrate position and oxygen gas flow rate on the properties of ZnO: Al films prepared by reactive co-sputtering, Thin Solid Films, 515 (2007) 5444-5448.

[156] T. Minami, T. Miyata, T. Yamamoto, H. Toda, Origin of electrical property distribution on the surface of ZnO:Al films prepared by magnetron sputtering, Journal of Vacuum Science and Technology A: Vacuum, Surfaces and Films, 18 (2000) 1584-1589.

[157] S. Swann, Film thickness distribution in magnetron sputtering, Vacuum, 38 (1988) 791-794.

[158] R.J. Hong, X. Jiang, B. Szyszka, V. Sittinger, S.H. Xu, W. Werner, G. Heide, Comparison of the ZnO:Al films deposited in static and dynamic modes by reactive mid-frequency magnetron sputtering, Journal of Crystal Growth, 253 (2003) 117-128.

[159] L.M. Peter, Photocurrent spectroscopy of lead dioxide, Surface Science, 101 (1980) 162-172.

[160] M. Vopsaroiu, K. O'Grady, M.T. Georgieva, P.J. Grundy, M.J. Thwaites, Growth rate effects in soft CoFe films, IEEE Transactions on Magnetics, 41 (2005) 3253-3255.

[161] R.H. Horng, D.S. Wuu, L.H. Wu, M.K. Lee, Formation process and material properties of reactive sputtered IrO2 thin films, Thin Solid Films, 373 (2000) 231-234.

[162] M. Heinemann, H.J. Terpstra, C. Haas, R.A. De Groot, Electronic structure of β-PbO2 and its relation with BaPbO3, Physical Review B, 52 (1995) 11740-11743.

[163] J.P. Pohl, G.L. Schlechtriemen, Concentration, mobility and thermodynamic behaviour of the quasi-free electrons in lead dioxide, Journal of Applied Electrochemistry, 14 (1984) 521-531.

[164] D.J. Payne, R.G. Egdell, W. Hao, J.S. Foord, A. Walsh, G.W. Watson, Why is lead dioxide metallic?, Chemical Physics Letters, 411 (2005) 181-185.

[165] D.O. Scanlon, A.B. Kehoe, G.W. Watson, M.O. Jones, W.I.F. David, D.J. Payne, R.G. Egdell, P.P. Edwards, A. Walsh, Nature of the band gap and origin of the conductivity of PbO 2 revealed by theory and experiment, Physical Review Letters, 107 (2011).

[166] A. Walsh, A.B. Kehoe, D.J. Temple, G.W. Watson, D.O. Scanlon, PbO2: From semi-metal to transparent conducting oxide by defect chemistry control, Chemical Communications, 49 (2013) 448-450.

[167] A.J. Leenheer, J.D. Perkins, M.F.A.M. Van Hest, J.J. Berry, R.P. O'Hayre, D.S. Ginley, General mobility and carrier concentration relationship in transparent amorphous indium zinc oxide films, Physical Review B - Condensed Matter and Materials Physics, 77 (2008).

[168] G. Masetti, M. Severi, S. Solmi, Modeling of carrier mobility against carrier concentration in arsenic-, phosphorus-, and boron-doped silicon, IEEE Transactions on Electron Devices, ED-30 (1983) 764-769.

[169] D. Slocombe, A. Porch, M. Pepper, P.P. Edwards, The Mott transition and optimal performance of transparent conducting oxides in thin-film solar cells, Energy and Environmental Science, 5 (2012) 5387-5391.

[170] J. Huang, P.F. Miller, J.S. Wilson, A.J. De Mello, J.C. De Mello, D.D.C. Bradley, Investigation of the effects of doping and post-deposition treatments on the conductivity, morphology, and work function of poly(3,4-ethylenedioxythiophene)/poly(styrene sulfonate) films, Advanced Functional Materials, 15 (2005) 290-296.

[171] V.V. Aleksandrov, V.V. Boldyrev, V.V. Marusin, V.G. Morozov, V.S. Solovjev, T.M. Rozhentseva, Effect of heating rate on the thermal decomposition of lead dioxide, Journal of Thermal Analysis, 13 (1978) 205-212.

[172] L. Burgio, R.J.H. Clark, S. Firth, Raman spectroscopy as a means for the identification of plattnerite (PbO2), of lead pigments and of their degradation products, Analyst, 126 (2001) 222-227.

[173] L.M. Peter, A photoelectrochemical study of the reduction of alpha lead dioxide in aqueous sodium tetraborate, Journal of Electroanalytical Chemistry, 144 (1983) 315-330.

[174] V.T. Avanesyan, V.A. Bordovskii, E.P. Baranova, G.I. Grabko, Kinetics of polarization current in a Pb3O4 wide-gap photoconductor, Semiconductors, 41 (2007) 1405-1407.

[175] D. Chaverri, A. Saenz, V. Castano, Grain size and electrical resistivity measurements on aluminum polycrystalline thin films, Materials Letters, 12 (1991) 344-348.

[176] A.K. Kulkarni, K.H. Schulz, T.S. Lim, M. Khan, Dependence of the sheet resistance of indium-tin-oxide thin films on grain size and grain orientation determined from X-ray diffraction techniques, Thin Solid Films, 345 (1999) 273-277.

[177] C.J. Tavares, M.V. Castro, E.S. Marins, A.P. Samantilleke, S. Ferdov, L. Rebouta, M. Benelmekki, M.F. Cerqueira, P. Alpuim, E. Xuriguera, J.P. Rivière, D. Eyidi, M.F. Beaufort, A. Mendes, Effect of hot-filament annealing in a hydrogen atmosphere on the electrical and structural properties of Nb-doped TiO 2 sputtered thin films, Thin Solid Films, 520 (2012) 2514-2519.

[178] S. Mugo, J. Yuan, Influence of surface adsorption on work function measurements on gold-platinum interface using scanning Kelvin probe microscopy, Journal of Physics: Conference Series, 371 (2012).

[179] A. Ohta, H. Murakami, S. Higashi, S. Miyazaki, Determination of energy band alignment in ultrathin Hf-based oxide/Pt system, Journal of Physics: Conference Series, 417 (2013).

[180] D. Gu, S.K. Dey, P. Majhi, Effective work function of Pt, Pd, and Re on atomic layer deposited HfO_2, Applied Physics Letters, 89 (2006) 82907-82901 - 82907-82903.

[181] D. Cao, C. Wang, F. Zheng, W. Dong, L. Fang, M. Shen, High-efficiency ferroelectric-film solar cells with an n-type Cu_2O cathode buffer layer, Nano Letters, 12 (2012) 2803-2809.

[182] D.E. Markov, E. Amsterdam, P.W.M. Blom, A.B. Sieval, J.C. Hummelen, Accurate measurement of the exciton diffusion length in a conjugated polymer using a heterostructure with a side-chain cross-linked fullerene layer, Journal of Physical Chemistry A, 109 (2005) 5266-5274.

[183] Z. Bao, A. Dodabalapur, A.J. Lovinger, Soluble and processable regioregular poly(3-hexylthiophene) for thin film field-effect transistor applications with high mobility, Applied Physics Letters, 69 (1996) 4108-4110.

[184] J.F. Chang, B. Sun, D.W. Breiby, M.M. Nielsen, T.I. Sölling, M. Giles, I. McCulloch, H. Sirringhaus, Enhanced Mobility of poly(3-hexylthiophene) transistors by spin-coating from high-boiling-point solvents, Chemistry of Materials, 16 (2004) 4772-4776.

[185] A. Salleo, R.J. Kline, D.M. DeLongchamp, M.L. Chabinyc, Microstructural characterization and charge transport in thin films of conjugated polymers, Advanced Materials, 22 (2010) 3812-3838.

[186] G. Wang, J. Swensen, D. Moses, A.J. Heeger, Increased mobility from regioregular poly(3-hexylthiophene) field-effect transistors, Journal of Applied Physics, 93 (2003) 6137-6141.

[187] Y.-I. Lee, J.-H. Youn, M.-S. Ryu, J. Kim, J. Jang, CdSe quantum dot cathode buffer for inverted organic bulk hetero-junction solar cells, Organic Electronics, 13 (2012) 1302-1307.

[188] G.D. Sharma, S.P. Singh, M.S. Roy, J.A. Mikroyannidis, Solution processed bulk heterojunction polymer solar cells with low band gap DPP-CN small molecule sensitizer, Organic Electronics, 13 (2012) 1756-1762.

[189] J. Wu, G. Yue, Y. Xiao, J. Lin, M. Huang, Z. Lan, Q. Tang, Y. Huang, L. Fan, S. Yin, T. Sato, An ultraviolet responsive hybrid solar cell based on titania/poly(3-hexylthiophene), nature scientific reports, 3 (2013) 1-6.

[190] W. Zhang, Z. Tan, D. Qian, L. Li, Q. Xu, S. Li, H. Zheng, Y. Li, ITO electrode/photoactive layer interface engineering for efficient inverted polymer solar cells based on P3HT and PCBM using a solution-processed titanium chelate, J. Phys. D: Appl. Phys., 45 (2012) 1-7.

[191] R. Dietmueller, H. Nesswetter, S.J. Schoell, I.D. Sharp, M. Stutzmann, Band alignment at organic-inorganic heterojunctions between P3HT and n-type 6H-SiC, ACS Applied Materials and Interfaces, 3 (2011) 4286-4291.

[192] M.H. Chan, J.Y. Chen, T.Y. Lin, Y.F. Chen, Direct evidence of type II band alignment in ZnO nanorods/poly(3- hexylthiophene) heterostructures, Applied Physics Letters, 100 (2012).

[193] V. Gowrishankar, S.R. Scully, M.D. McGehee, Q. Wang, H.M. Branz, Exciton splitting and carrier transport across the amorphous-silicon/ polymer solar cell interface, Applied Physics Letters, 89 (2006).

[194] D.C. Olson, S.E. Shaheen, M.S. White, W.J. Mitchell, M.F.A.M. Van Hest, R.T. Collins, D.S. Ginley, Band-offset engineering for enhanced open-circuit voltage in polymer-oxide hybrid solar cells, Advanced Functional Materials, 17 (2007) 264-269.

[195] D. Chirvase, Z. Chiguvare, M. Knipper, J. Parisi, V. Dyakonov, J.C. Hummelen, Electrical and optical design and characterisation of regioregular poly(3-

hexylthiophene-2,5diyl)/fullerene-based heterojunction polymer solar cells, Synthetic Metals, 138 (2003) 299-304.

[196] T. Oku, S. Nagaoka, A. Suzuki, K. Kikuchi, Y. Hayashi, H. Inukai, H. Sakuragi, T. Soga, Formation and characterization of polymer/fullerene bulk heterojunction solar cells, Journal of Physics and Chemistry of Solids, 69 (2008) 1276-1279.

[197] A.K. Thakur, A.K. Mukherjee, D.M.G. Preethichandra, W. Takashima, K. Kaneto, Charge injection mechanism across the Au-poly(3-hexylthiophene-2,5-diyl) interface, Journal of Applied Physics, 101 (2007).

[198] J. Huang, G. Li, Y. Yang, Influence of composition and heat-treatment on the charge transport properties of poly(3-hexylthiophene) and [6,6]-phenyl C61 -butyric acid methyl ester blends, Applied Physics Letters, 87 (2005).

[199] H.C. Liao, N. Chantarat, S.Y. Chen, C.H. Peng, Annealing effect on photovoltaic performance of hybrid P3HT/In-situ grown CdS nanocrystal solar cells, Journal of the Electrochemical Society, 158 (2011) E67-E72.

[200] S. Lilliu, T. Agostinelli, E. Pires, M. Hampton, J. Nelson, J.E. Macdonald, Dynamics of crystallization and disorder during annealing of P3HT/PCBM bulk heterojunctions, Macromolecules, 44 (2011) 2725-2734.

[201] A. Mittiga, E. Salza, F. Sarto, M. Tucci, R. Vasanthi, Heterojunction solar cell with 2% efficiency based on a Cu2O substrate, Applied Physics Letters, 88 (2006).